



**Shear turbulence controllable synthesis of micro particles in
a turbulent Rankine vortex flow reactor – Mechanism and
Applications**

by

Jiaying Lu

Submitted in partial satisfaction of the requirements for the degree of
Master of Mechanical Engineering

Under the supervision of

Prof. Xiaogang Yang

Dr. Hao Chen

September 2021

DEDICATION

To my family.

ACKNOWLEDGEMENTS

It is impossible to complete my master's dissertation without many people's help in this year. Foremost, I would like to give my sincere thanks to my supervisor Prof. Xiaogang Yang, who gave me valuable guidance and inspiration throughout my research work and has always been approachable and patient. His meeting discussions and insights helped build up a scientific thinking style on the computational fluid dynamics, especially the dimensionless number that I was previously unfamiliar of it. In addition, I would like to thank Dr. Faith Chan and Dr. Hao Chen who gave me support and valuable inputs to my academic study.

Besides, I am greatly to Dr. Yanqing Guo in the FAST group, who instructed me on my first project and taught me synthesis skills when I firstly joined the group and through my whole master's study. I would also like to thank Dr. Chenyang Xue and Mr. Bin Li for their support during the lab working. Next, I would like to thank my friends and colleagues Mr. Tuo Hou and Mr. Zhiyu Zhang for their assistance in scientific research and accompany in daily life. I will cherish this great friendship with them. My special thanks to Mr. Yicheng Qian, Ms. Jiahui Shen and Ms. Ke Wang for their daily care and support, even though miles apart

Most importantly, I must thank my parents and grandparents for allowing me to pursue my interest under their unconditional love, that mere words are insufficient and unnecessary for.

SYNOPSIS

A large amount of attention has been paid to the approaches of synthesis micro/nano particles. In comparison with other methods such as hydrothermal treatment or self-assembly method, shear controllable methods have been attractive in recent study. Shear controllable synthesis has the advantages of precise control, high mass transfer rate and variable properties of synthesized production. In order to promote research in this area, we have developed a reactor, a counter swirling flow reactor, which can improve the mixing performance and mass transfer rate several times than conventional mixing tank.

This dissertation involves numerical simulations and micro/nano particle synthesis. First, we focus on the computational fluid dynamics inside the reactor. By using the ANSYS Fluent, hydrodynamic characteristics are captured giving a general concept of the underlying mechanisms. We highly concentrate on the shear turbulence at high Reynolds number, because the shear rate is the key factor in determining the size, particle size distribution and morphology of the production. Meanwhile, empirical formulas are given for better describing the relationship between hydrodynamics and synthesised particles.

Second, the effects of shear rate induced by both hydrodynamics and ultrasound irradiation under different experimental conditions have been illustrated. Because of the simplicity of the hydrolysis and condensation reaction of Tetraethyl orthosilicate (TEOS), amorphous nature and simple kinetics analysis, synthesis of SiO_2 is chosen as the experiment object. The spherical mesoporous SiO_2 nanoparticles are widely applied in Adsorption, catalysis, photoluminescence and biomedicine. However, particle size and morphology controllable technologies do not meet the industrial requirements. Based on the above discussion, it can be postulated that the characteristics of mesoporous SiO_2 nanoparticles can be affected by local shear turbulence. To reveal the exact influence of the local shear turbulence on production, several analysis methods have been adopted, such as Scanning Electron

Microscopy image, N₂ adsorption–desorption isotherm measurement, Fourier transform infrared spectroscopy and particle size analysis.

Overall, the results of the work give an insight into the shear controllable synthesis process, which can provide a platform for further industrial synthesis. Future works of study on the mechanism and application of shear controllable synthesis of silica will be studied in much greater detail.

TABLE OF CONTENTS

ACKNOWLEDGEMENTS.....	i
SYNOPSIS.....	ii
TABLE OF CONTENTS.....	iii

Chapter 1. Current status of shear turbulence controllable

synthesis of mesoporous silica nanoparticles

1.1 Introduction.....	1-1
1.2 Fundamentals of controllable synthesis of mesoporous micro/nano particles	1-2
1.2.1 Conventional synthesis approaches.....	1-2
<i>Hydrothermal treatment</i>	1-2
<i>Self-assembly method</i>	1-5
<i>Combustion and calcination</i>	1-8
<i>Sol-gel method</i>	1-12
1.2.2 Shear controllable synthesis of micro/nano particles	1-15
<i>Hydrodynamic shear generation by turbulent shear flows</i>	1-15
<i>Turbulent shear enhancement by ultrasound irradiations</i>	1-17
1.2.3 Possible morphology and structure of mesoporous micro/nano SiO ₂ particles.....	1-20
1.3 Reactor systems used for turbulent shear controllable synthesis of mesoporous micro/nano particles	1-23
1.3.1 Types and characteristics of reactors for turbulent shear generation	1-23
<i>Continuous stirring tank reactor (CSTR)</i>	1-23

<i>Taylor - Couette reactor (TCR)</i>	1-26
<i>Impinging jet reactor (IJR)</i>	1-32
<i>Swirling vortex flow reactor (SVFR)</i>	1-36
1.3.2 Effects of hydrodynamics in various reactors on synthesis process of mesoporous micro/nano particles	1-39
<i>Flow heterogeneity</i>	1-39
<i>Flow homogeneity</i>	1-42
<i>Shear turbulence generation</i>	1-44
1.4 Modelling of hydrodynamics in the process of mesoporous micro/nano particles synthesis	1-45
1.4.1 Interfacial momentum transfer	1-46
1.4.2 Interfacial mass transfer	1-47
1.4.3 Modelling of chemical reaction taking place in the SiO₂ mesoporous particle synthesis	1-51
<i>Descriptions of synthesis reaction</i>	1-51
1.4.4 Numerical simulation of mesoporous micro particle transport in turbulence shear generation reactors	1-52
<i>Eulerian- Eulerian approach</i>	1-53
<i>Eulerian- Lagrange approach</i>	1-53
1.4.5 Turbulence modelling	1-54
<i>k-ε model</i>	1-54
<i>Reynolds stress model</i>	1-56
<i>Large eddy simulation</i>	1-57
1.5 Recapitulation and concluding remarks	1-58
References	1-60

Chapter 2. Modelling of silica micro/nano particle synthesis process

2.1	Introduction.....	2-1
2.2	Mathematical modelling.....	2-2
2.2.1	Governing equations for descriptions of particle synthesis process ..	2-2
2.2.2	Turbulence closure model of RSM.....	2-3
2.2.3	Numerical modelling.....	2-5
	<i>Description of the problem</i>	<i>2-5</i>
	<i>Mesh generation.....</i>	<i>2-7</i>
	<i>Boundary conditions</i>	<i>2-9</i>
2.3	Results and discussion on silica micro/nano particle synthesis	11
2.3.1	Shear turbulence in counter swirling impinging flow reactor.....	2-11
2.3.2	Turbulence shear effect on particle aggregation.....	2-14
	<i>The formulation of particle aggregation</i>	<i>2-14</i>
	<i>Particle size prediction</i>	<i>2-15</i>
2.4	Effects of the interaction between the turbulence shear rate and reaction on synthesis process.....	2-19
2.5	Conclusion	2-21
	References.....	2-23

Chapter 3. Experimental investigation on turbulence shear controllable synthesis of micro/nano porous silica oxide particle

3.1	Introduction.....	3-1
3.2	Experimental setup	3-2
3.3	Materials and experimental description	3-3

3.4 Synthesis and kinetics	3-6
3.4.1 Reaction kinetics of silica nanoparticles by sol-gel process	3-7
3.4.2 Formation process of silica oxide	3-9
3.5 Characterization methods	3-12
3.6 Results and discussion	3-14
3.6.1 Characteristics of synthesised silica oxide particles	3-14
3.6.2 Effect of hydrodynamics in counter swirling impinging flow reactor on silica oxide synthesis	3-19
3.6.3 Effect of ultrasound irradiation intensification on in hydrodynamic synthesis	3-21
3.7 Conclusion	3-23
References	3-25

Chapter 4. Conclusions and outlook for the future work

4.1 Conclusions for the present study	4-1
4.2 Recommendations for future work	4-2

Chapter 1. Current status of shear turbulence controllable synthesis of mesoporous silica nanoparticles

1.1 Introduction

Mesoporous silica materials (MSNs) have achieved significant advancements in drug delivery technologies. The ordered and uniform pores make it possible to carry variety of cargo ranging from RNA (Zhang and Kleinstreuer, 2011, Vanaki et al., 2014), proteins (Gao et al., 2021, Xu et al., 2019) and DNA (Sun et al., 2019, Hai et al., 2018), which may have problems in crossing the cell membranes, lack of specificity, poor performance on solubility and stability. The Stober's method is always the way to synthesis spherical monodisperse silica micro particles (Narayan et al., 2018). The widely used approaches to achieve chemical reaction are sol-gel process, self-assembly, hydrothermal treatment with post treatment like combustion and calcination. However, the above approaches have shortcomings in industry applications such as low effectiveness, poor performance on production quality and high consumption. In this study we introduce a shear controllable synthesis method. High shear stress can induce the aggregation between particles, affect the crystal growth direction and characteristic uniformity, through which the characteristics of mesoporous silica materials can be tuneable. Considering the need to enlarge the industrial application of MSNs, it is necessary to figure out an effective way in synthesis MSNs and its underlying mechanism. Then, this dissertation will particularly focus on shear controllable synthesis of mesoporous silica nanoparticles.

1.2 Fundamentals of controllable synthesis of mesoporous micro/nano particles

1.2.1 Conventional synthesis approaches

Hydrothermal treatment

The hydrothermal treatment is of particular interest since it is a low cost, environmentally friendly method (Tam et al., 2006). It was seen as an effective way for rational synthesis and crystal engineering in the area of ionic conductors, compound oxides and fluorides, inorganic-organic hybrid microporous materials, and especially condensed materials. With advantages such as high reactivity of reactants, easy to control interface reactions, generation of metastable and unique condensed phases, it arouses the interest in hydrothermal treatment (Feng and Xu, 2001). Compared with other routes, like templating, anodic oxidation methods. Hydrothermal synthesis has some obvious drawbacks, including the long reaction duration, addition of highly concentrated base, hard to achieve uniform size and thermal stable (Liu et al., 2014).

Homogeneous nucleation processes, small grain sizes and high purity powders are important assessment in hydrothermal treatment. Lee and Choi (2004) synthesised CeO₂ particles under temperature of 200 °C for 6h with the various concentrations of H₂O₂ (0.5, 0.8, 1mol). Figure 1-1 is the all X-ray diffraction patterns of the prepared CeO₂ powders which shows the presence cubic fluorite structure and the production is pure with no other phase due to the impurities elimination during the calcination step.

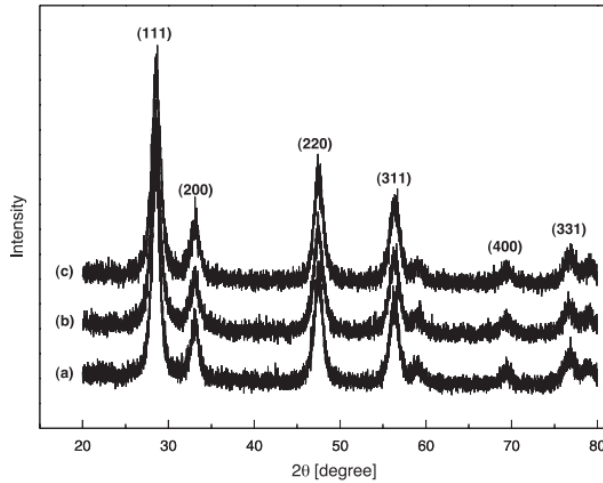


Figure 1-1 Xray diffraction of CeO₂ powders at different H₂O₂ concentrations: (a) 0.5, (b) 0.8 and (c) 1 mol.

Sonali et al. (2020) synthesised ZnO nanoparticles separately by two different ways: modified auto-combustion and hydrothermal. The particle size was almost uniform and spherical in shape in both the cases. However, an obvious difference was noticed from Figure 1-2. The fraction of particles obtained from hydrothermal synthesis was small and uniformly distributed than those obtained from combustion.

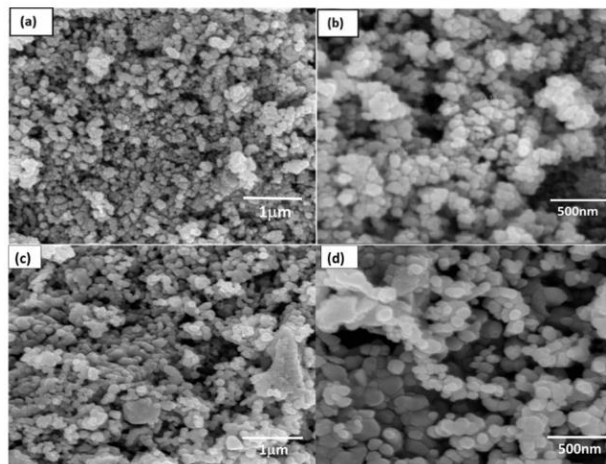


Figure 1-2 FE-SEM images of ZnO nanoparticles. Hydrothermal synthesis route: (a) and (b); combustion synthesis: (c) and (d).

Neto et al. (2020) synthesised $ZnWO_4$ nanoparticles by microwave-assisted hydrothermal treatment with different reaction time (0, 5, 10, 30, 60, 120 min). The hydrothermal treatment time had no significant changes in $ZnWO_4$ structure as shown in Figure 1-3. The average diameters for 0 min and 120 min are 28.81 and 26.74 nm, respectively. The crystallinity of the nanoparticles increased with the time increase, as seen through the diffractograms (Figure 1-4). Furthermore, Figure 1-5 illustrates that the photocatalytic activity improved with the increased hydrothermal treatment time.

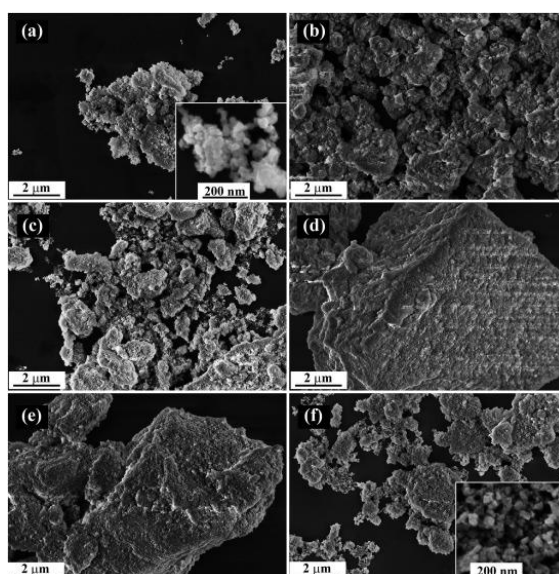


Figure 1-3 Prepared SEM images (a) ZW0, (b) ZW5, (c) ZW10, (d) ZW30, (e) ZW60 and (f) ZW120.

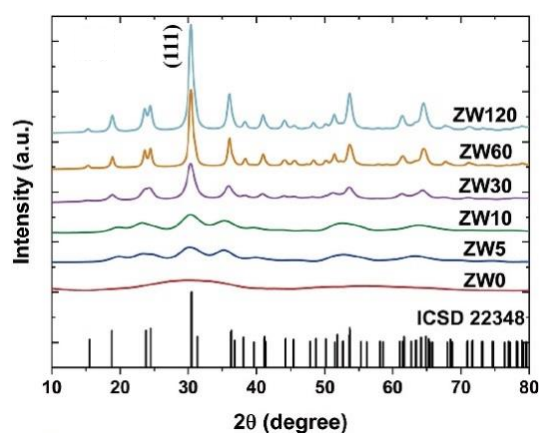


Figure 1-4 Diffractograms for $ZnWO_4$ samples.

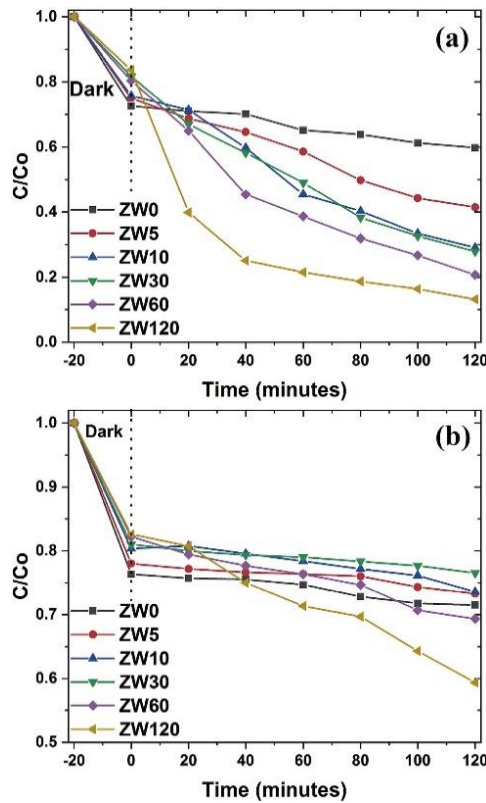


Figure 1-5 Concentration variation curves as a function of test time of the (a) MB and (b) MO dyes for the ZnWO₄ samples.

Self-assembly method

Self-assembly (SA) is a process by which nanoparticles or other discrete components spontaneously organize due to specific interactions through their environment (Grzelczak et al., 2010). It is commonly used in producing nanoparticles and forming nanostructures. This free energy driven process spontaneously organizes molecules into ordered structures at multiple length scales. The biggest advantage of this method is by controlling the experimental conditions, the structure of the final production can be easily and finely tuned (Cui et al., 2010).

Pacholski et al. (2002) synthesised zinc oxide nanoparticles which were synthesised from C₄H₁₀O₆Zn in alcoholic solution under basic conditions via self-assembly

method. They found that the overall concentration of precursors is a key factor in determining the shape of the ZnO particles. The TEM image in Figure 1-6 depicts two different morphologies of ZnO. Under low concentration of zinc acetate dihydrate (starting sol) the synthesised particles were nearly spherical, whereas at 10 times higher concentrations mainly nanorods were formed.

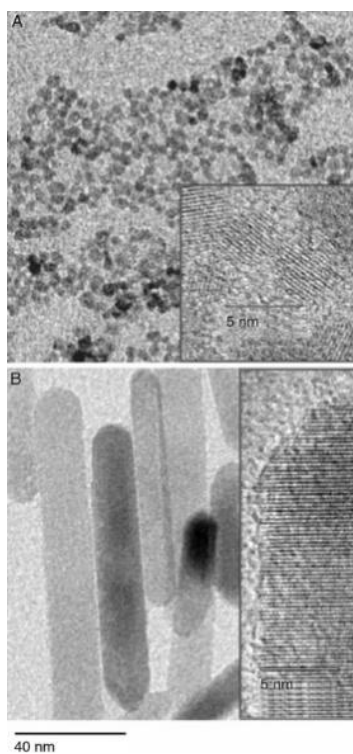


Figure 1-6 TEM images of ZnO. A) starting sol; B) after one day of reflux of the concentrated sol.

Cui et al. (2010) synthesised PA functional material by using molecular self-assembly to produce. They illustrated the driving forces for this process which mainly consisted of hydrophobic interactions, hydrogen bonding, and electrostatic repulsions. The hydrophobic interactions and hydrogen bonding are attractive forces that tend to promote the aggregation of PA molecules, whereas electrostatic repulsions from the charged components disassociate the molecules. The size, shape and interfacial

curvature of the final production reflect a delicate balance between these energy contributions.

Boal et al. (2000) demonstrated that the self-assembly process provides control over the resulting aggregates. A polymer-mediated strategy has been introduced for the self-assembly of nanoparticles into ordered one. As shown in Figure 1-7, the highly ordered and multi-scale discrete nanoparticles were formed. Self-assembly is also very temperature dependent due to the balance between entropic and enthalpic effects. Figure 1-8 displayed the morphologies of aggregates at different temperature. The results showed that larger aggregate structures were yielded at lower temperatures.

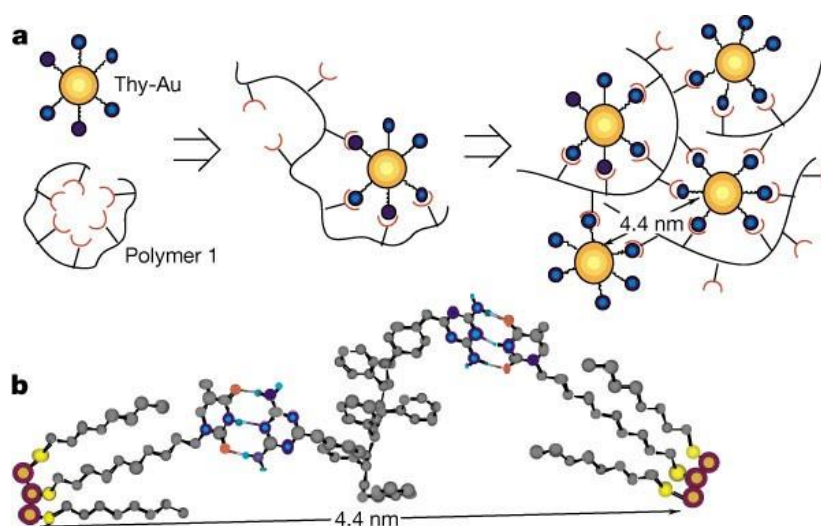


Figure 1-7 Proposed mechanism for the aggregation of polymer 1-Thy-Au. a, Polymer mediated self-assembly of Thy-Au, showing the experimentally determined interparticle distance. b, Proposed polymer 1-Thy-Au self-assembled structure, showing the computationally predicted interparticle distance.

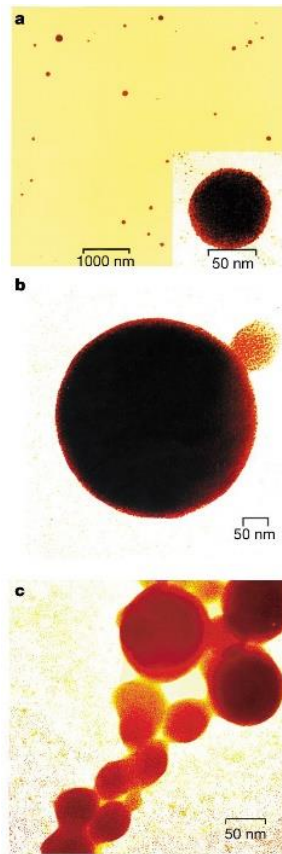


Figure 1-8 TEM image of polymer 1-Thy-Au aggregates formed at different temperatures: (a) 23°C. (b) -20°C. (c) 10°C.

Combustion and calcination

Combustion is often used to synthesis metal particles in various areas, such as space, explosions, underwater propulsion and hydrogen formation (Sundaram et al., 2015).

Physicochemical processes play an important role in combustion process, such as heat and mass transfer between the particle and the gas phase, transformations in the oxide layer, and exothermic chemical reactions. Lynch et al. (2010) demonstrated the mechanism of combustion that occurs heterogeneously on the nano aluminium particle surface as shown in Figure 1-9. The overall concept of this mechanism can be concluded as mass diffusions and chemical reactions.

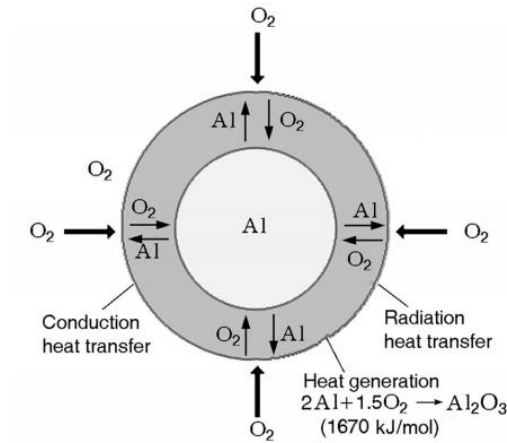


Figure 1-9 Three important processes in combustion of nano aluminum particles in oxygen.

Nagaveni et al. (2004) have synthesised nano TiO₂ particles by solution combustion method. The synthesised particles were used for the solar photocatalytic degradation of various organic dyes as a property indicator. Degradation figures illustrated the rate of degradation with combustion synthesised. As shown in Figure 1-10 the performance of combustion synthesised TiO₂ was much better than commercial TiO₂, this can be attributed to the small size, crystal structure, high crystallinity, large number of surface hydroxyl groups and decreased band-gap energy of the catalyst which enhanced the solar energy absorption.

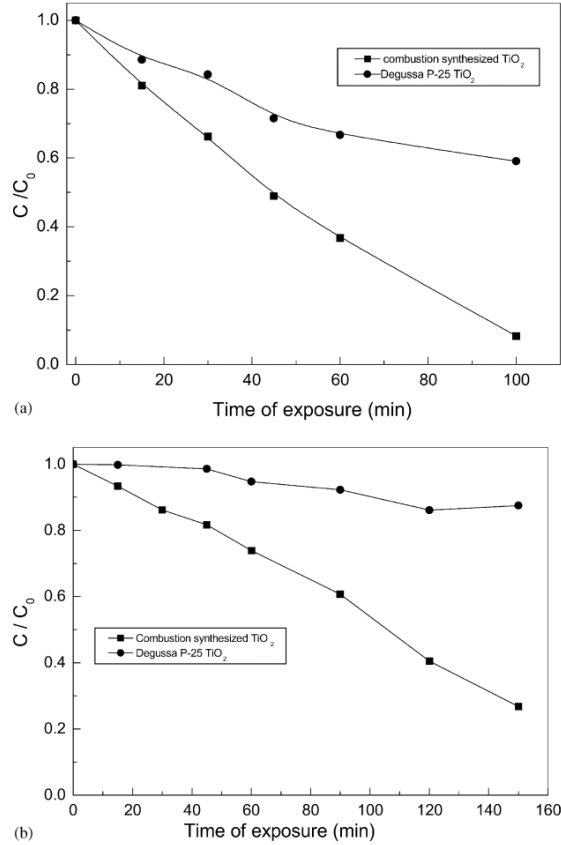


Figure 1-10 Degradation profiles of (a) OG with 25 ppm and (b) RBBR with 100 ppm initial concentration with catalyst loading of 1 kg m^{-3} .

Calcination can remove volatile matter by heating the inorganic materials. During the calcination, the release of volatile components minimizes internal shrinkage in later processing steps that can lead to the development of internal stresses and, eventually, cracking or warping (Rand, 1991).

Al-Hada et al. (2014) synthesised ZnO nanosheets by thermal-treatment method. The calcination here allowed the removal of organic matter and nitrate ions leaving a residue of pure powders. The influence of calcination temperature was displayed in Figure 1-11, the average particle size decreased from 38 to 23 nm with the increase of calcination temperature. The band gap energy of ZnO nanoparticles also changed from 3.260 eV to 3.23 eV as shown in Figure 1-12.

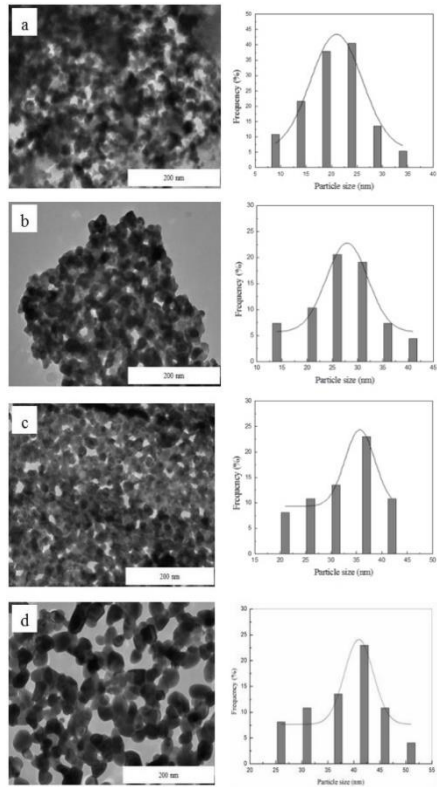


Figure 1-11 TEM images and particle size distribution of ZnO nanosheets at calcination temperature of (a) 500°C, (b) 550°C, (c) 600°C and (d) 650°C.

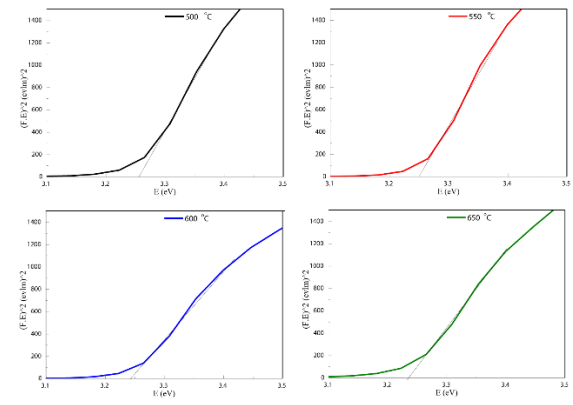


Figure 1-12 The band gap energy of ZnO nanosheets calcined at different temperatures.

Among the elements which may have effect upon the grain size and microstructure of nano-TiO₂ powders, Li et al. (2003) found the calcination temperature was more effective compared with the calcination time and concentration. The nanoparticle size

tended to increase with the increasing temperature which was plotted in Figure 1-13. It grows slowly at low calcination temperatures and then becomes very fast at high calcination temperatures.

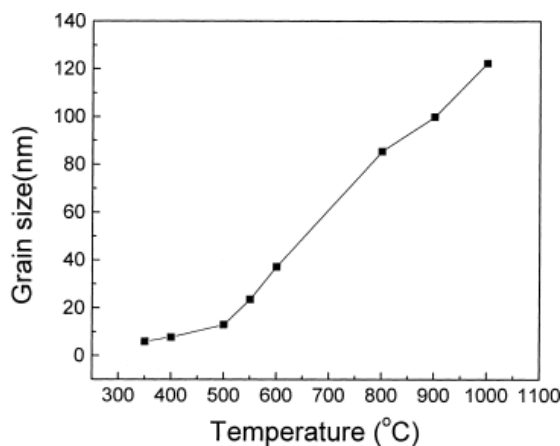


Figure 1-13 The grain size as a function of different calcination temperatures.

Sol-gel method

The advantage of sol–gel is that the obtained production is nano sized crystallized particles with high purity at relatively low temperature. This method normally needs subsequent post treatments for crystallization such as annealing. However, the annealing may cause hard aggregation and even inter-particle sintering (Macwan et al., 2011). As a liquid phase method, it can be influenced by several parameters, such as pH, precursors, temperature, reactants molar ratios, solvent composition and conditions of aging and drying.

Sol-gel method has wide applications in coating including thin films, optical coating and corrosion resistant coatings (Dehghanhadikolaei et al., 2018). Sharma et al. (2020) synthesised nano powder of TiO₂ by sol-gel method. After annealing, TiO₂ nanocrystals were generated with good structural, optical and electrochemical properties. The synthesised TiO₂ nanoparticles showed absorbance in the UV range,

by using the solar radiation the UV-Vis can be extended to near-infrared region which makes them adopted in photochromic applications. From the image of absorption spectra (Figure 1-14), TiO₂ samples presented a peak value at 342 nm.

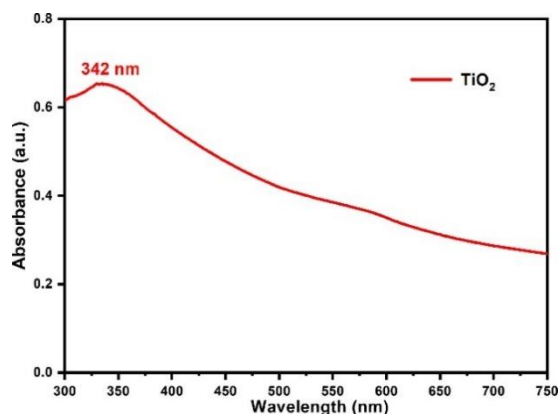


Figure 1-14 UV-Vis absorption spectrum of TiO₂ nanoparticles.

Martins et al. (2017) also synthesised TiO₂/activated carbon as a photocatalyst employed to decomposition of tetracycline via sol-gel method. By comparing with bare TiO₂ and P25, the properties and catalytic activity can be roughly evaluated. According to Figure 1-15, TiO₂/AC had better structural and electronic features for photocatalysis.

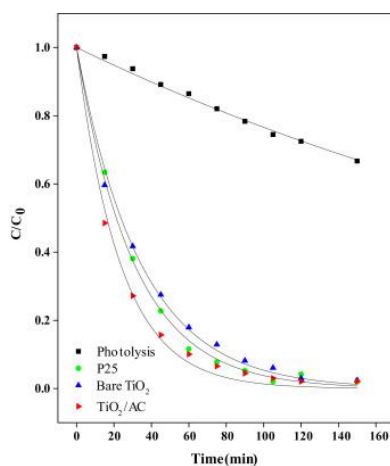


Figure 1-15 Kinetic curves from pseudo-first order kinetic model fitted to the experimental data of TC photodegradation reaction under photolysis (■) and catalysed by P25 (●), bare TiO₂ (▲) and TiO₂/AC (►) composite.

Vazquez et al., (2017) illustrated the effect of different molar ratio of surfactant and H₂O on morphology and particle size. Figure 1-16 was the SEM images of mesoporous silica particles prepared by sol–gel as a function of the surfactant and water amount. It was clearly that the CTAB concentration has significant influence on the growth of particles, as shown in Figure 1-16 under low concentration of CTAB more homogeneous spherical particles are formed.

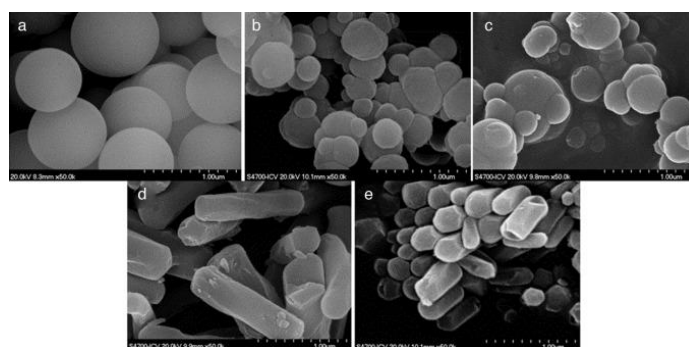


Figure 1-16 SEM images of mesoporous silica particles at different molar ratios (a) 0 CTAB:45 H₂O, (b) 0.1 CTAB:45 H₂O, (c) 0.3 CTAB:45 H₂O, (d) 0.3 CTAB:600 H₂O and (e) 0.3 CTAB:1200 H₂O.

Although aqueous sol–gel approaches are highly attractive, they bring some major limitations forward when need to synthesis nanoscale production. During the process, hydrolysis, condensation and aggregation always occur simultaneously and are difficult to control individually. Therefore, subtle changes in experimental conditions can lead to changes in particle morphology, which poses great difficulties for experimental repeatability (Niederberger, 2007).

1.2.2 Shear controllable synthesis of micro/nano particles

As discussed, the synthesis of inorganic particles is divided into three stages: nucleation, growth and agglomeration. These three stages are inevitably occurring at the same time when synthesis in a batch environment. This can be attributed to the inability to mix and separate the agglomerated particles well during their growth, which leads to great difficulties for experimental repeatability in both size and size distribution of nanoparticles. In addition, insufficient mixing and mass transfer problems will be exacerbated after scaling up the batch synthesis, resulting in various physical and chemical characteristics of poly-dispersed population of nanoparticles.

Microfluidic synthesis approach has been widely studied since 1990s, a great deal of research has been devoted to this area. Especially the continuous-flow microfluidic systems, are attractive due to their accurate control, high heat and mass transfer efficacy, intensive mixing, large reaction interfaces compared with conventional synthesis methods. In microfluidic systems, the nucleation and growth stages of nanoparticle formation can be separated with reference to the distance from the solution mixing region, giving excellent control of size, particle size distribution and morphology, thus increasing reproducibility (Ma et al., 2017).

Hydrodynamic shear generation by turbulent shear flows

High shear mixer (HSM) system is a method with high mass and heat efficacy, it has been commonly used in fine dispersions and homogeneous reaction mixing process (Koopmans et al., 2013). Liu et al. (2015a) synthesised LiFePO_4 nanoparticles in a HSM via hydrothermal method, the effect on the particle size distribution and morphology of final production was demonstrated. It was clearly that in contrast to those formed with the conventional impeller, the HSM-assisted synthesised LiFePO_4

nanoparticles presented remarkable discharge capacity. Table 1-1 showed that from the structural characteristics to carbon content, LiFePO₄/C composites with HSM had a better performance.

Table 1-1 Different characteristics with samples synthesised under various conditions.

Sample	a (nm)	b (nm)	c (nm)	V (nm ³)	D _[020] ^a (nm)	S _{BET} (m ² ·g ⁻¹)	Carbon content (wt%)
LFP/C- H1.9	1.0330	0.6007	0.4693	0.2912	60.2	14.8	1.04
LFP/C- H1.6	1.0328	0.6006	0.4692	0.2911	59.3	15.0	1.08
LFP/C- H1.3	1.0328	0.6005	0.4690	0.2909	58.9	15.6	1.18
LFP/C- H1.0	1.0330	0.6008	0.4693	0.2912	61.1	14.3	0.99
LFP/C-CI	1.0333	0.6009	0.4695	0.2915	63.0	12.5	0.84

Jeon et al. (2020) illustrated the effect of different design factors, such as nozzle position, reactor and heater temperature, residence time and swirling intensity, in synthesis TiO₂ nanoparticles. Among these design factors, the reactor and heater temperatures, residence time and swirl intensity of the flow field had a significant impact on nanoparticles.

AlAmer et al. (2018) utilised a Taylor-Couette reactor to synthesise GO under different hydrodynamic flow regimes. As shown in Figure 1-17, GtO-3 (synthesised under Taylor vortex flow) was showed highest oxidation level with the G peak position around ~1600 cm⁻¹ and high full-width-at-half-maximum levels. As can be seen from the optical microscope images (Figure 1-18), the continuous high shear applied in Couette flow made GtO particles smaller.

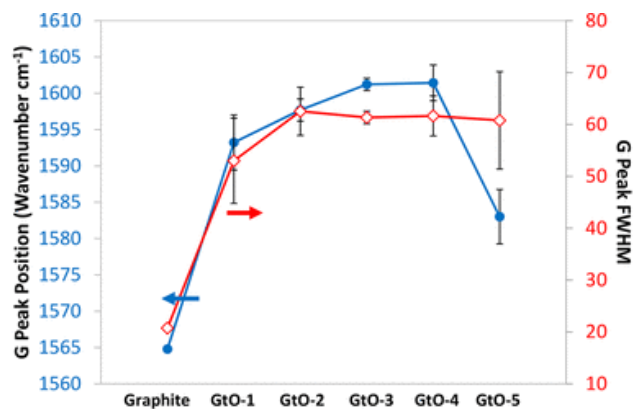


Figure 1-17 G band position and full-width-at-half-maximum of GtO samples under different flow conditions.

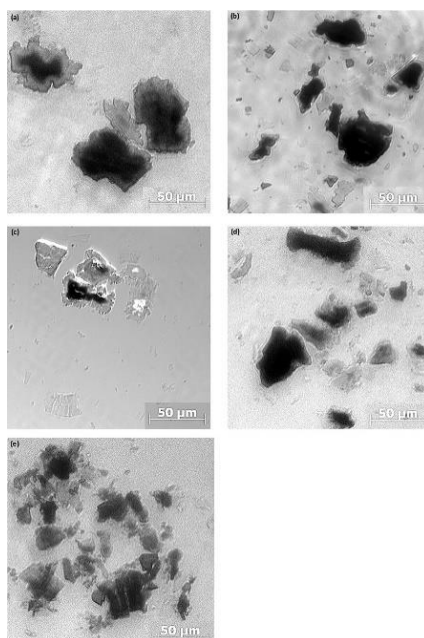


Figure 1-18 Optical microscope images of samples (a) GtO-1, (b) GtO-2, (c) GtO-3, (d) GtO-4, and (e) GtO-5.

Turbulent shear enhancement by ultrasound irradiations

The application of ultrasound field in chemical synthesis is termed sonochemical. There are two possible mechanisms of nanoparticle synthesis using sonochemical approach. One is the generation of gas/vapor filled micro bubbles, with the spread of ultrasound wave inside the reactant solution and employment of huge energy release

from the implosive collapse of bubbles, thus intensifies the physicochemical processes. The other is the formation of shock waves and turbulent flows which leads to a large amount of microbubble collapse and turbulence shear stress, influences the morphology and crystallinity of nanoparticles (Radziuk et al., 2010).

According to Morse and Ingard (1961), the following equations can be used to predict the boundary layer thickness δ , the tangential velocity around the bubble surface v_t and the shear stress ψ ,

$$\delta = \sqrt{\frac{2\eta}{\rho\omega}} \quad (1 - 1)$$

$$v_t \approx \frac{\omega\xi^2 R_0^4}{r^2} \Rightarrow \frac{\omega\xi^2}{R_0} \quad (1 - 2)$$

$$\psi = \eta \frac{\partial v_t}{\partial r} \approx \frac{\eta\omega\xi^2}{R_0\delta} \quad (1 - 3)$$

where η is the viscosity of water at room temperature, ρ is the density of water at room temperature, R_0 is an equilibrium bubble radius and ω is the frequency of ultrasound.

Ultrasound-assisted preparation has distinct effect on particle size. The imposed ultrasound power can induce more intensive interaction which results in the more homogeneous particle size. Fatimah et al. (2020) investigated the antibacterial activity of silver and gold nanoparticles. The nanoparticles synthesised under ultrasound irradiation had smaller size ranging at 18-50 nm, as shown in Figure 1-19. The imposed ultrasound power can induce more intensive interaction which resulted in the more homogeneous particle size. Khoshooei et al. (2021) also reported that the ultrasonic irradiation had great impact on particle size controllable. While in the study of Hu et al. (2020) the nanoparticles size increased with the increase of ultrasonic

treatment time (as shown in Figure 1-20), they believed under ultrasound field the collision of the solute molecules increased which enables the molecules around crystals to jump into the crystal lattice more easily.

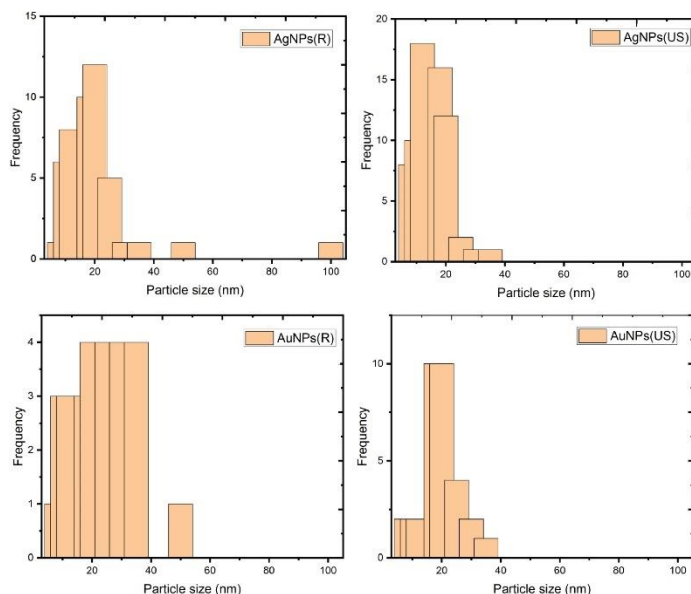


Figure 1-19 Nanoparticles size distribution in the AuNPs and AgNPs at varied synthesis method.

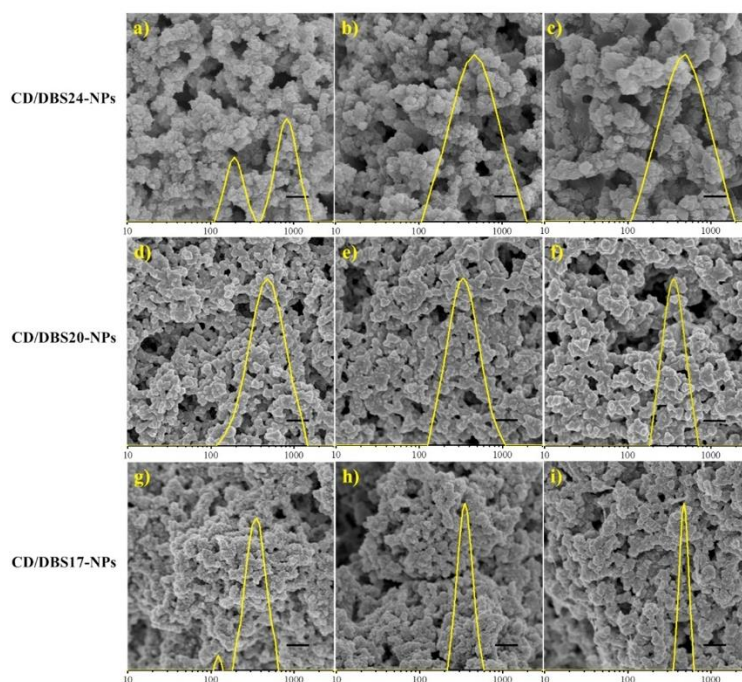


Figure 1-20 SEM images and particle size distributions (yellow line) of varying samples.

Other research showed that ultrasonic-assisted method can significantly improve the specific surface area. Bounab et al. (2021) used both ultrasonic bath and probe sonication in synthesis zero valent iron nanoparticles, the obtained results showed that the higher BET specific surface area and porosity were formed than the ones synthesised in stirring condition, which increased the number of active surface sites. Yang et al. (2020) investigated the approaches to enhance the drug loading capacity, they found greater drug loading was obtained under ultrasonic treatment due to the improvement of specific surface area.

1.2.3 Possible morphology and structure of mesoporous micro/nano SiO₂ particles

Azlina et al. (2016) have synthesised nano SiO₂ using sol-gel method. Figure 1-21 and 1-22 demonstrated the surface morphology of samples aged during 2 h, 4 h and 6 h at calcination temperatures of 600 °C and 700 °C. The particle size of silica powder ranges from 2.81-3.39 μm , and the nanoparticle size of the silica became larger with the increasing aging time and increasing temperature.

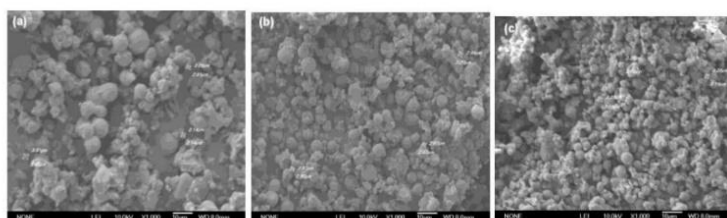


Figure 1-21 SEM image of silica nanostructures at calcination temperature of 600 °C for various aging times: (a) 2 h (b) 4 h (c) 6 h.

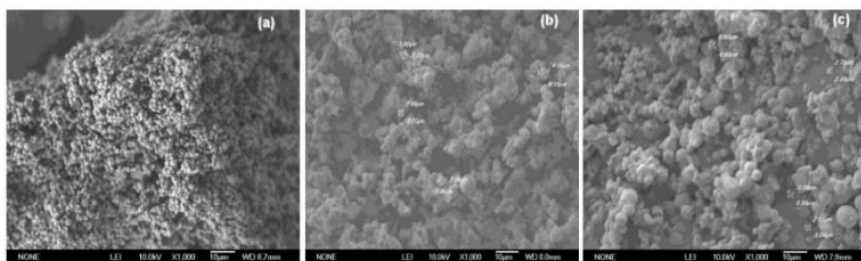


Figure 1-22 SEM image of silica nanostructures at calcination temperature of 700 °C for various aging times: (a) 2 h (b) 4 h (c) 6 h.

The structure and size of nanoparticles are known to be highly dependent on the molar ratio of reactants. Tabatabaei et al. (2006) revealed the effects of solvent in the synthesis process of nano silica oxide, and illustrated particle structure morphology and the average diameter of colloidal silica particles depend on the proportion of the reactants. As seen in Figure 1-23, different molar ratio of ethanol results in different nanostructures. With higher molar ratio of ethanol, smaller particle size and a broader size distribution of particle sizes were obtained.

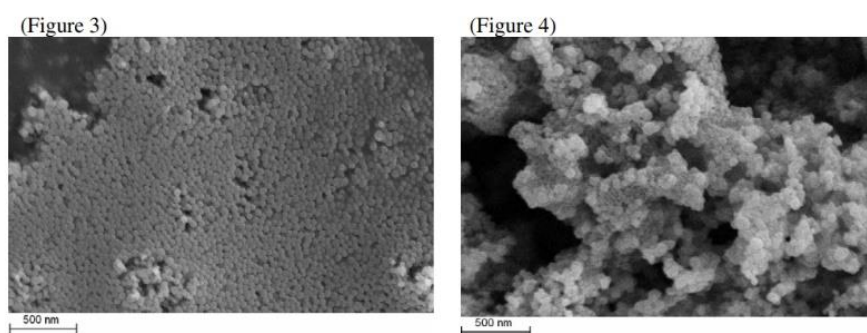


Figure 1-23 SEM images of silica particles obtained from a molar ratio of Water :

TEOS : Ammonia : Ethanol. (Fig. 3) 1 : 4 : 6 : 6; (Fig. 4) 1 : 4 : 6 : 24.

Ling et al. (2021) used microreactor for synthesis silica nanoparticles. As shown in Figure 1-24, the nanostructure of silica synthesised in the microflow system showed high mono-dispersity with almost spherical structure. And the particle size distribution was narrower where most of the nano SiO₂ fell within the range of 3 to 8 nm, as shown in Figure 1-25.

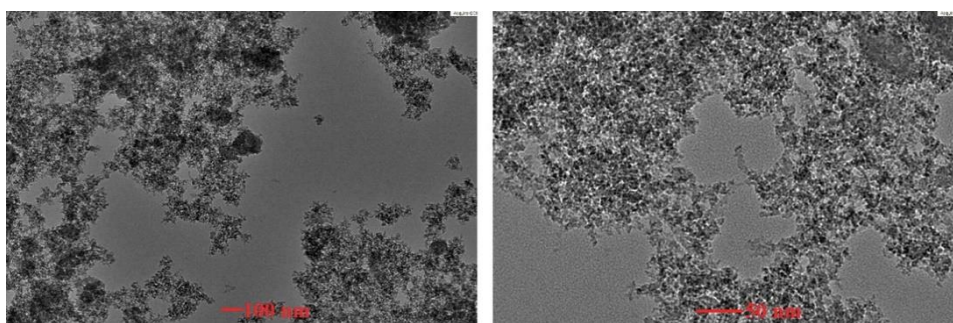


Figure 1-24 TEM images of silica nano particles synthesised within microflow system.

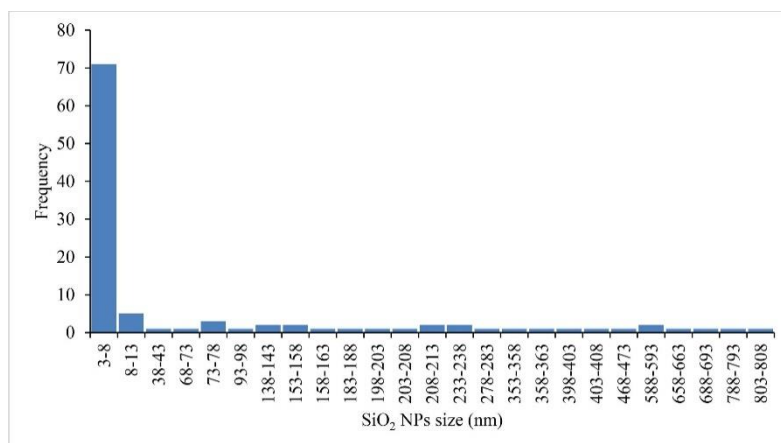


Figure 1-25 Silica nanoparticle size distribution produced in the microflow system.

1.3 Reactor systems used for turbulent shear controllable synthesis of mesoporous micro/nano particles

1.3.1 Types and characteristics of reactors for turbulent shear generation

Continuous stirring tank reactor (CSTR)

Continuous synthesis is a sustainable approach, limitations of equilibrium and product inhibition occurred in batch synthesis can be overcome due to its continuous throughput. Therefore, continuous synthesis process can achieve large-scale production of nanomaterials to meet the growing industrial demand (Tang et al., 2018). Continuous stirring tank reactor is widely used in industrial applications due to its high mixing efficacy and fast mass transfer rate.

CSTR is often used in industrial fermentations because of their good mixing capability and high mass transfer rate although power requirement for scale-up can be an issue (Orgill et al., 2013). The mixing process is usually carried out by mechanical mixing or magnetic mixing, which can evenly distribute the temperature and the reactant. In the process of CSTR synthesis, the continuous injection is required to maintain the concentration, so the control of the concentration is the key factor affecting the morphology of the nanoparticles (Tang et al., 2018).

Tang et al. (2018) compared CSTR with batch reactor on the synthesis of Ag nanosheets. As shown in Figure 1-26, with the increase of the impeller agitation speed the size and thickness of Ag nanosheets were slightly changed, which may indicate an protection from the effect of agitation speed. Figure 1-27 demonstrated the concentration of reagent with time in batch reactor and CSTR, revealed the concentration effect on Ag nanosheets.

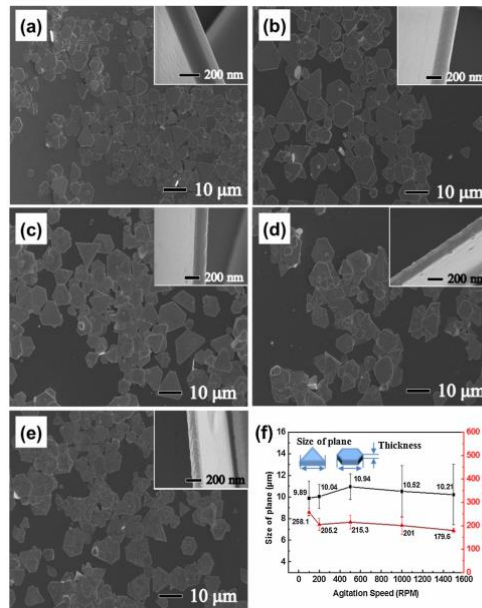


Figure 1-26 SEM images of the Ag nanosheets synthesised by CSTR at varying rotation speeds (a) 100, (b) 200, (c) 500, (d) 1000, and (e) 1500 rpm. (f) Size and thickness distribution.

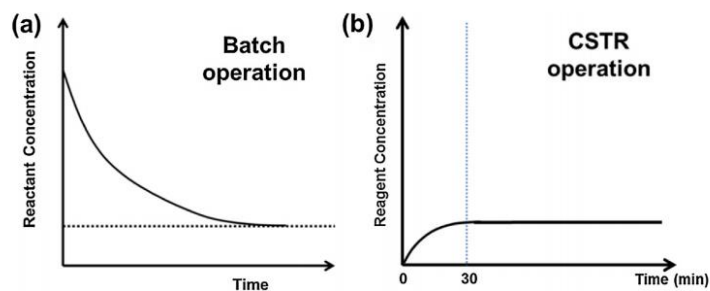


Figure 1-27 Concentration profile of reagent in the (a) batch reactor and (b) CSTR during the reactions.

Mechanical stirring or mechanical mixing is a technique commonly used to improve the mixing intensity. In order to improve the mass transfer rate and uniformity of the fluid in the reactor, the stirred tank reactor is equipped with rotating impellers. Hoseini et al. (2021) and Mustafa et al. have studied on the impeller effect on mixing in stirring tank reactor, V- and U-shape impellers were compared with the conventional 6-blade Rushton turbine. These two new designs of impellers can reduce

the power consumption of stirred tank reactor by 21% and 48% respectively in a wide Reynolds number range, as can be seen in Figure 1-28.

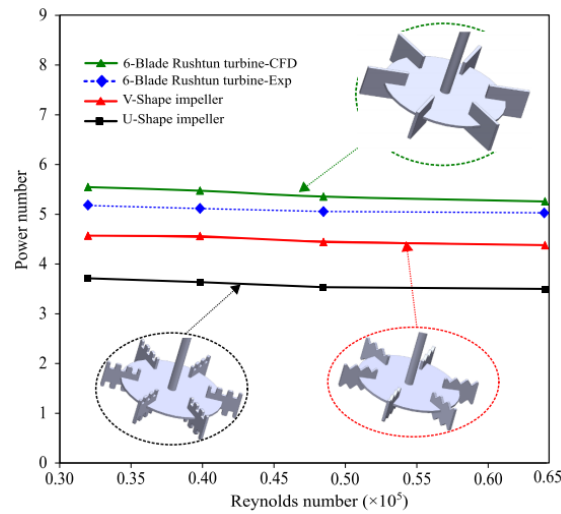


Figure 1-28 Power number of reactors with different impellers at varying Reynolds number estimated by CFD technique.

Mustafa et al. (2020) also studied four different impellers on the mixing performance. Among the edge beater, 5-turbine blade, t-shape, and paddle impeller, the edge beater had better performance on the mixing of two-phase fluid and the mixed pattern flow was formed. From the image of flow pattern (Figure 1-29), edge beater blade can produce two streams in opposite direction, besides a small rotational flow was generated as well between the impellers.

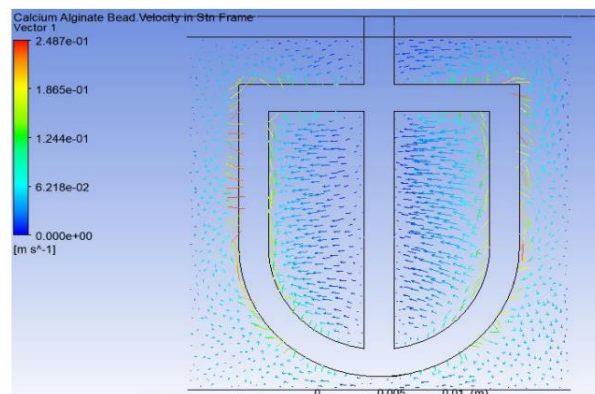


Figure 1-29 Flow pattern with edge beater at 250 rpm.

In a stirred tank the specific energy dissipation rate is explicitly determined by the shear rate γ and the shear stress τ , described as follows (Mustafa et al., 2020)

$$\frac{P}{V} = G\tau \quad (1 - 4)$$

where P is the input power and V is the fluid volume in the stirred tank.

For Newtonian fluids, the viscosity μ can be expressed as the ratio of shear stress and shear rate

$$\mu = \frac{\tau}{G} \quad (1 - 5)$$

Therefore, the Equation 1-4 can be rewritten as follows, which can be applied to laminar, turbulent and transitional flows,

$$\frac{P}{V} = G\tau = G\tau \frac{G}{G} = \mu G^2 \quad (1 - 6)$$

$$or G = \left(\frac{1 P}{\mu V} \right)^{1/2} \quad (1 - 7)$$

According to the power law, the shear stress of non-Newtonian fluids can be given as follows,

$$\tau = K G^n \quad (1 - 8)$$

where K is the consistency index and n is the flow behaviour index.

For non-Newtonian fluids the corresponding equation is given as,

$$\frac{P}{V} = \mu_a G^2 \quad (1 - 9)$$

where $\mu_a = \tau/\gamma = K G^{n-1}$ is the apparent viscosity.

Taylor - Couette reactor (TCR)

Taylor-Couette reactor consists of a cylindrical reactor with a rotating cylinder. This structure allows the creation of a unique flow pattern in the gap between two

co-axially positioning cylinders. Due to its high and effective mass and heat transfer ability, this reaction system has a wide range of application in crystallization, phase transformations, and particle purification process (Park et al., 2015, Kim, 2014, Nguyen et al., 2011, Park and Kim, 2018). Compared with a typical mixing tank reactor, the phase transformation process is several times faster in TCR system. From these works, it is clearly indicated that the Taylor vortex flow formed in the reactor plays an important role in improving reaction speed, particle size distributions, and morphology control of particles (Nguyen et al., 2012, Wu et al., 2015). As discussed, the Taylor-Couette reactor is promising in mass production of micro/nano particles (Tang et al., 2019).

The fluid is contained in the gap between the two axially positioned cylinders, and different fluid dynamic regimes are based on the rotation of the inner cylinder (Figure 1-30). A measure of the state of the flow is represented by the dimensionless Taylor and Reynolds numbers, which are defined by the following equations (Marchisio et al., 2001)

$$Ta = \frac{\Omega_1^2 r_1 d^3}{\nu} \quad (1 - 10)$$

$$Re = \frac{\Omega_1 r_1 d}{\nu} \quad (1 - 11)$$

where Ω_1 is the speed of the inner cylinder, r_1 is the radius of inner cylinder, d is the annular gap between two cylinders and ν is the kinematic viscosity.

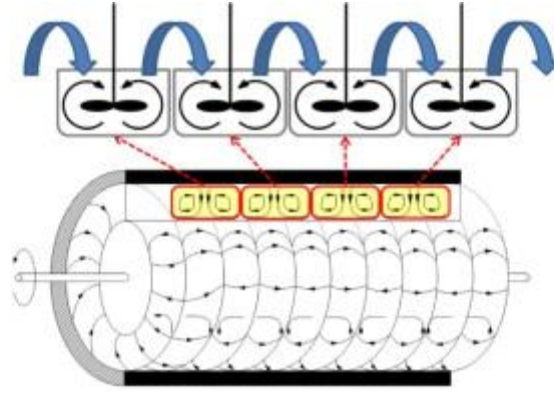


Figure 1-30 Schematic diagram of Taylor vortex induced by TCR.

For further illustrated the relationship between mass transfer rate and rotational speed of inner cylinder, Tang et al. demonstrated an empirical formula between mass transfer coefficient (k_L^0) and rotational speed, describing as follows (Tang et al., 2019):

$$k_L^0 = \alpha v^* = \frac{\alpha \sqrt{\tau_{wi}}}{\rho} = \frac{\alpha r_i \sqrt{f \rho}}{\rho} w_i \quad (1 - 12)$$

where α is a dimensionless empirical constant, ρ is the flow density, r_i and w_i are the radius and the rotational speed of the inner cylinder, respectively, and f is the friction factor.

The commonly used dimensionless numbers of Couette flow can be defined as below (Seenivasan et al., 2021):

$$Re = \frac{\rho_c a h^2}{\mu_c} \quad (1 - 13)$$

$$Ca = \frac{\mu_c a h}{\gamma} \quad (1 - 14)$$

$$We = \frac{\rho_c a^2 h^3}{\gamma} \quad (1 - 15)$$

With shear rate $a = U/h$, where U is the linear velocity of inner cylinder, h is the gap between the cylinders, μ_c is continuous phase viscosity, ρ_c is continuous phase density and γ is interfacial tension.

For their application on particles synthesis, Tang et al. (2019) studied different morphologies of copper sulphide nanoparticles in a continuous Taylor-Couette reactor under various experimental operations. As shown in Figure 1-31 to 1-33, the structures and sizes changed dramatically when adjusting rotational speed, mean residence time and reagents concentration.

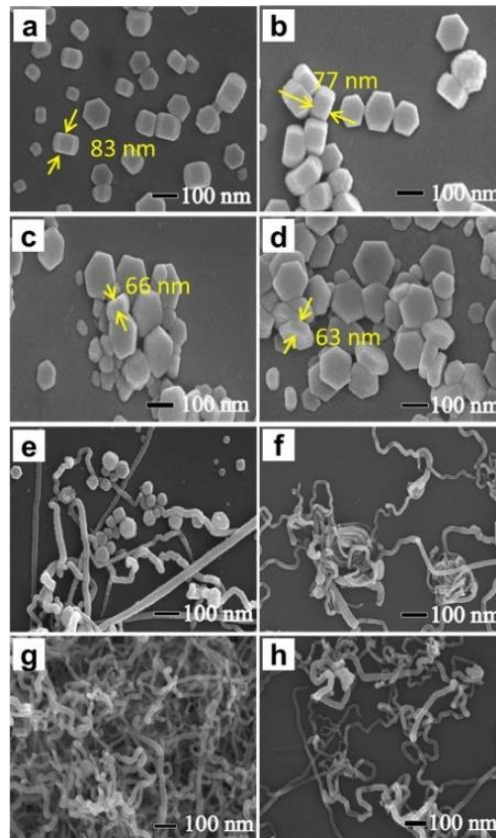


Figure 1-31 SEM images of nanoparticles synthesised under different rotational speed: (a) 90 rpm, (b) 200 rpm, (c) 500 rpm, (d) 1000 rpm, (e) 85 rpm, (f) 80 rpm, (e) 50 rpm, and (h) 5 rpm.

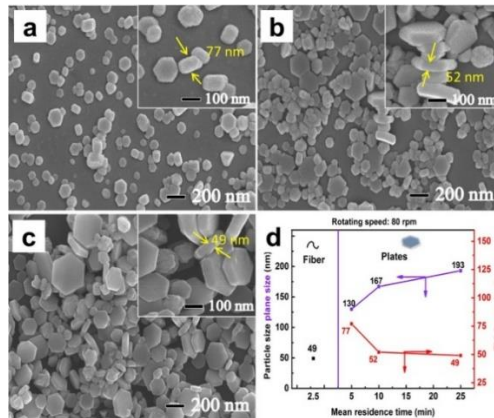


Figure 1-32 SEM images of nanoparticles synthesised in the TCR under different mean residence time.

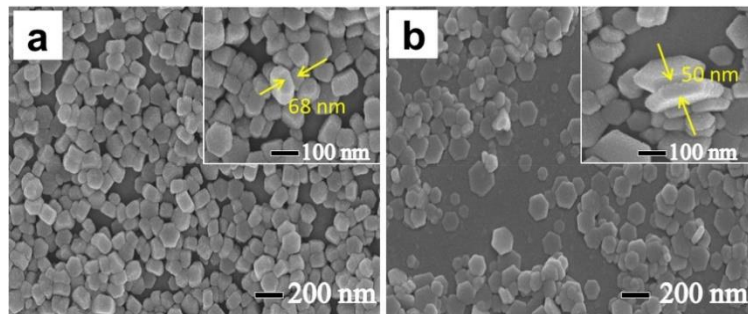


Figure 1-33 SEM images of nanoparticles synthesised in the TCR under different solution concentration (a) diluted 3 times and (b) diluted 6 times.

Kim et al. (2011) further illustrated the effect of Taylor vortex on aggregation process. Previous works showed that the aggregates can be effectively broken and re-dispersed before being transformed into concrete agglomerates under Taylor vortex. As shown in Figure 1-34, with the increasing the rotational speed the particle size was reduced, however, the particles were enlarged when increasing the mean residence time.

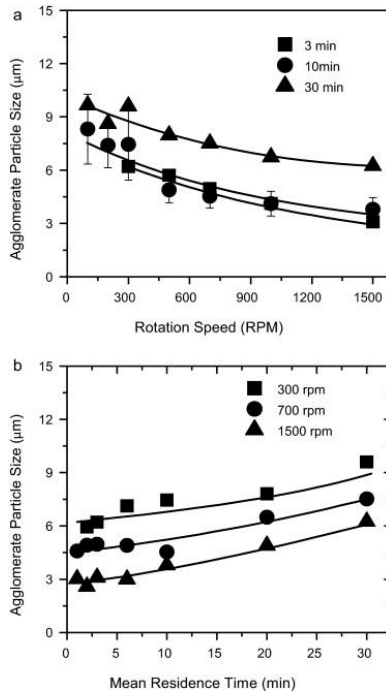


Figure 1-34 Effect of hydrodynamic conditions on particle size: (a) rotational speed and (b) mean residence time.

Metaxas et al. (2018) also investigated the influence of varying hydrodynamic conditions on assembly and morphology of polymer during the aggregation process. Figure 1-35 depicts the connection between radius of gyration and time under different situations. For laminar wavy vortex flow (LWV), turbulent wavy vortex flow (TWV) and turbulent Taylor vortex flow (TTV) type they reach a plateau value of R_g around 1mm. Intervortex mass transfer is quantified by the dispersion coefficient, give the equation below,

$$D_z^* = 2\lambda k_{cb} \quad (1 - 16)$$

where λ is the axial wavelength of vortex, and k_{cb} is the intermixing coefficient.

The image of lag time against D_z^* is shown in Figure 1-36. It was evident that the mass transfer rate is improved with speed increase, also the D_z^* had a remarkable increase from $1.12 \times 10^{-5} \text{ m}^2 \text{ s}^{-1}$ to $2.16 \times 10^{-4} \text{ m}^2 \text{ s}^{-1}$ over the range of Re used.

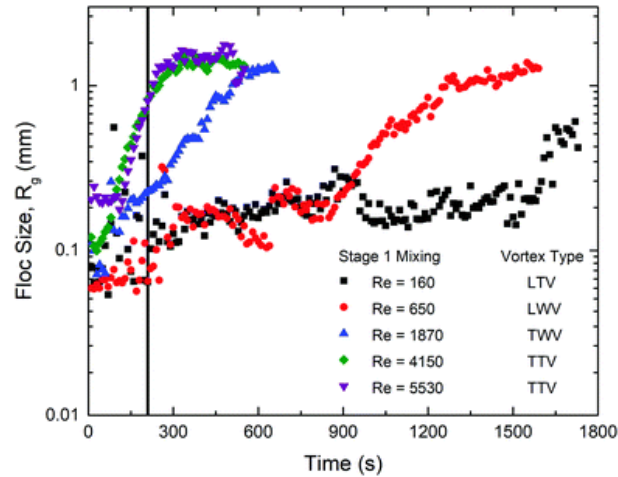


Figure 1-35 Bentonite floc size as a function of time under different conditions.

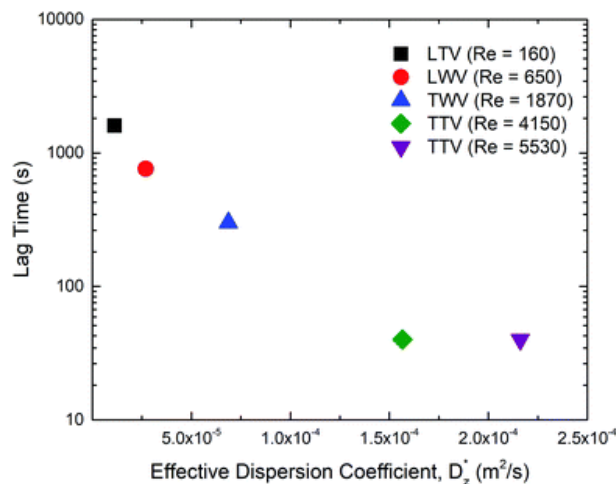


Figure 1-36 Lag time of floc growth as a function of the effective dispersion coefficient.

Impinging jet reactor (IJR)

Carver and Rollman (1956) first proposed the impinging jet reactor, which has been proved useful in a wide range application during chemical engineering process. The

impinging jet principle is the collision of two jets in opposite directions on the same axis. This collision and impingement can form a relatively narrow region in which the turbulence intensity is high, thus, providing good conditions for enhanced heat transfer and mass transfer rate.

Recently, confined impinging jet reactors (CIJRs) become attractive in precipitation of nanoparticles due to their effective mixing performance (Gavi et al., 2007a). The synthesised product has advantages of large surface area, high quality and purity, which bring its application wider than the natural origin (Wojtalik et al., 2020). In the impinging region the turbulent kinetic energy is produced and dissipated rapidly where strong mixing takes place. As show in Figure 1-37, compared with $Re_j=500$, high jet Reynolds numbers gave smaller size of impinging region and stronger mixing performance as shown by the mixture fraction variance contour plots (Gavi et al., 2007b).

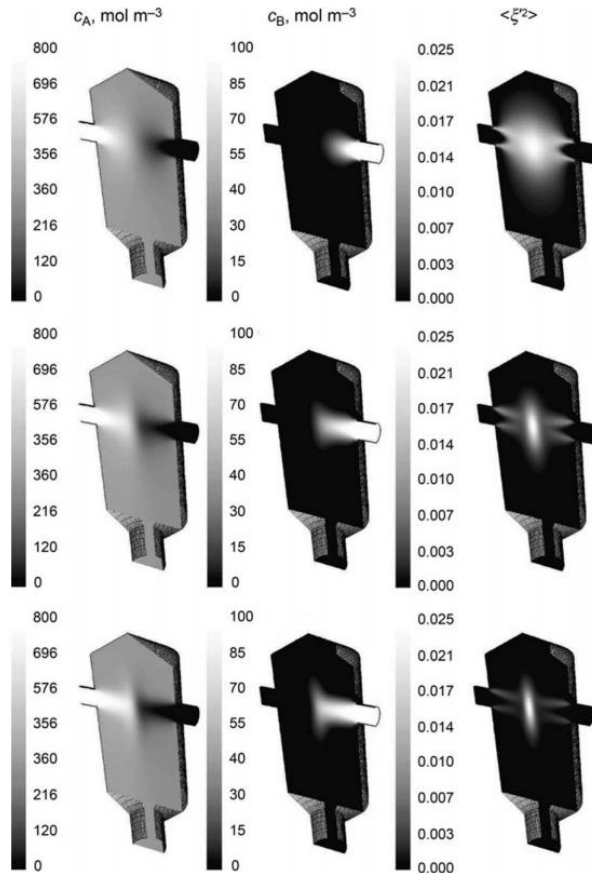


Figure 1-37 Contour plots of BaCl_2 concentration, Na_2SO_4 concentration and mixture fraction variance at three jet Reynolds number ($c_{A0} = 800 \text{ mol m}^{-3}$ and $c_{B0} = 100 \text{ mol m}^{-3}$; from top to bottom: $\text{Re}_j = 500, 1500, 2560$).

Baber et al. (2016) reported the influence of impinging jet reactor on synthesis silver nanoparticles. As shown in Figure 1-38, the average diameter of particles decreased with the improvement of flow rate. The dispersity increased with the increasing in mixing intensity. High mixing intensity leading to the increasing of supersaturation levels which would induce a higher nucleation rate and, thus, finer particles.

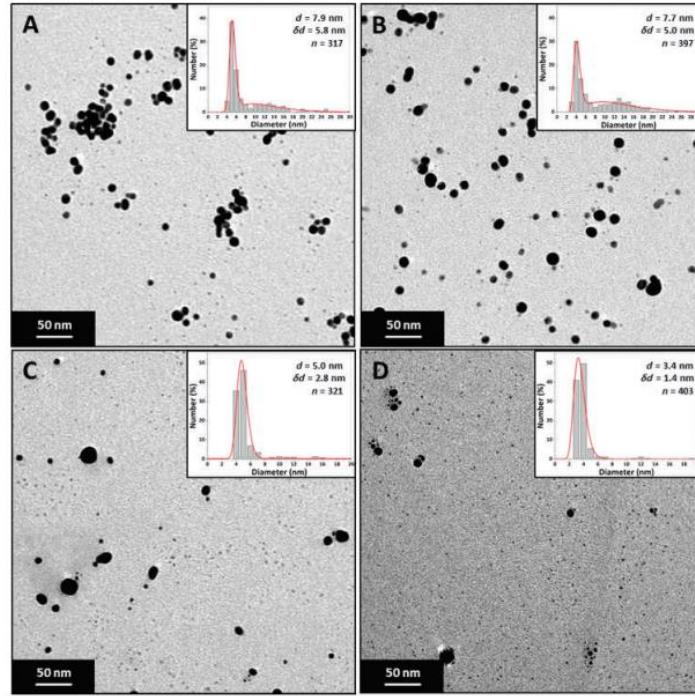


Figure 1-38 TEM images and particle size distribution of silver nanoparticle at different total flow rates: (a) 32 mL/min, (b) 48 mL/min, (c) 64 mL/min, (d) 72 mL/min.

Danckwerts' intensity of segregation can be used to calculate the mixing intensity at the impinging region, described as (Pal et al., 2021),

$$I_s = \frac{\sigma^2}{\sigma_{max}^2} \quad (1 - 17)$$

$$\sigma^2 = \frac{1}{V} \int (c - \bar{c})^2 dv \quad (1 - 18)$$

where \bar{c} is the mean value of the concentration field c , σ^2 and σ_{max}^2 are the variance and maximum possible variance, and V is the selected computational domain volume.

The mixing intensity can be given as (Pal et al., 2021),

$$I_m = I - \sqrt{I_s} = I - \frac{\sigma}{\sigma_{max}} \quad (1 - 19)$$

Swirling vortex flow reactor (SVFR)

The overall concept of swirling impingement is the introduction of tangential fluids into the main flow or the generation of swirling flow. To achieve the swirling flow impingement, the swirl generators are inserted into jet nozzle (Wongcharee et al., 2017).

Ray and Beenackers (1997) proposed a new swirl-flow monolithic-type semibatch reactor to measure the kinetic parameters for photocatalytic degradation of a textile dye. Figure 1-39 depicted the particle trajectory inside the reactor. The figure showed that the introduction of tangential fluid can generate a swirling flow.

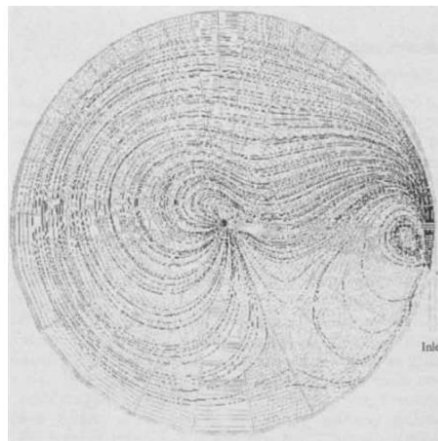


Figure 1-39 Flow pattern inside the novel reactor.

Mancuso (2018) investigated the flow characteristics in a swirling jet reactor using CFD analysis. One-phase and two-phase models were implemented in this case. Figure 1-40 is the velocity vectors inside the swirling jet reactor. It can be observed that a rotating flow was induced in pre-swirling chamber, with some small vortex created the intensification of the turbulence was promoted.

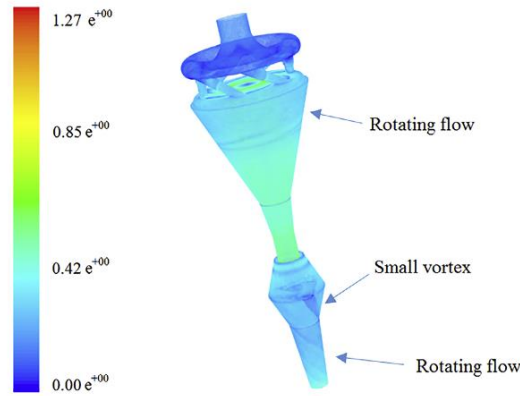


Figure 1-40 Fluid dynamics of the swirling jet reactor: velocity vectors colored by velocity magnitude [m s^{-1}], inletflow pressure 0.25 bar.

The rutile titanium dioxide (TiO_2) can be synthesised using an oxidation reactor which adopted a swirling flow condition to enhance gas mixing. Cheng et al. (2006) investigated the reactor design parameter to figure out how they affect the homogeneity of turbulence flow that further influence the production quality. Figure 1-41 showed the uniform profiles for the axial velocity with 60° of cross flow angle

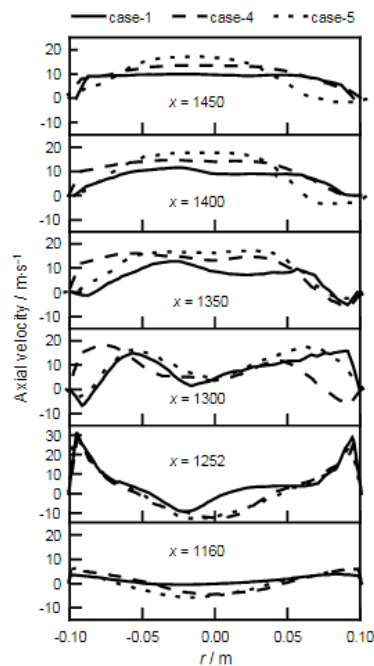


Figure 1-41 Comparison of axial velocity profiles for cases under 60° of cross flow

angle.

Wongcharee et al. (2017) compared the heat transfer of swirling impinging jet reactor with conventional impinging jet reactor, carried out at different conditions. They used TiO₂ nanofluid as the medium mainly due to its high thermal conductivity. The swirling flow was created by twisted tape inserts. As shown in Figure 1-42, at concentrations of 0.5%, 1.0%, 1.5%, 2.0% the swirling impinging jet reactor showed better performance on heat transfer than conventional one.

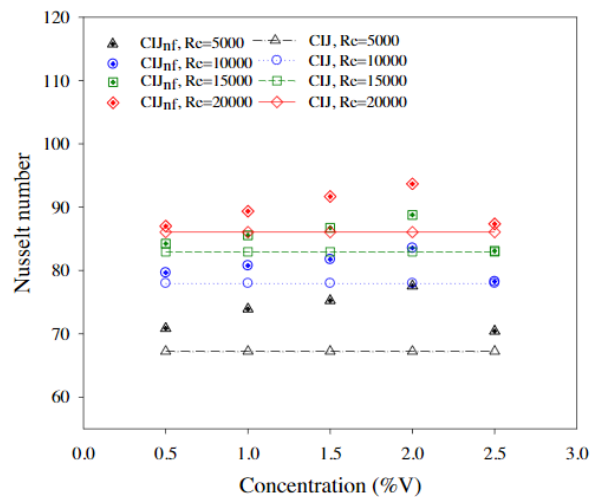


Figure 1-42 Effect of nano fluid concentration on average Nusselt number for CIJ at

$L/D=1.0$.

1.3.2 Effects of hydrodynamics in various reactors on synthesis process of mesoporous micro/nano particles

Flow heterogeneity

In gas-particles suspension, two kinds of flow structure always occur in computational parameters, homogenous flow and heterogeneous flow, as shown in Figure 1-43. Heterogeneous flow state consists of clusters, dispersed particles and interface (Xiaoxue et al., 2020).

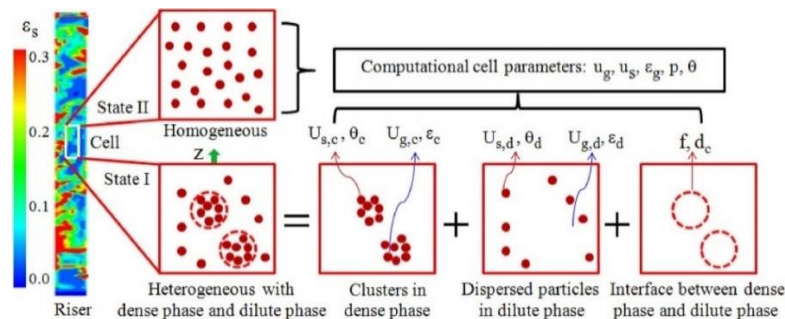


Figure 1-43 Homogenous flow state and heterogeneous flow state with the dense phase and the dilute phase in the computational cell.

Local shear turbulence, shear vortices and shear bands are the causes of the heterogeneity of local shear rate. Jiang et al. (2020) gave the profile (Figure 1-44) of the major characteristics of local shear heterogeneities. The red arrows denoted the sharp shear bands, shear turbulence is shown in Figure 1-44(c), and shear vortices is shown in Figure 1-44(d).

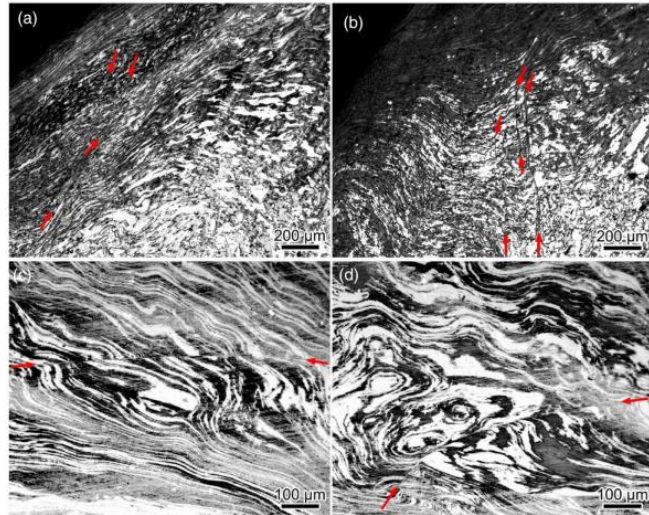


Figure 1-44 Optical micrographs of features in the heterogeneous flow: sharp shear bands (marked by red arrows), (c) shear turbulence, (d) shear vortices.

Spatial segregation plays an important role in heterogeneity. Oliveira et al. (2020) analysed spatially distribution of concentration to quantify the influence of heterogeneity on mixing, as shown in Figure 1-45. Under the heterogeneous flow field the reactants distributed throughout the whole domain, where the transverse mixing existed. Due to the heterogeneity the distribution of reaction rates was highly nonuniform, thus, affects reaction dynamics, as shown in Figure 1-46.

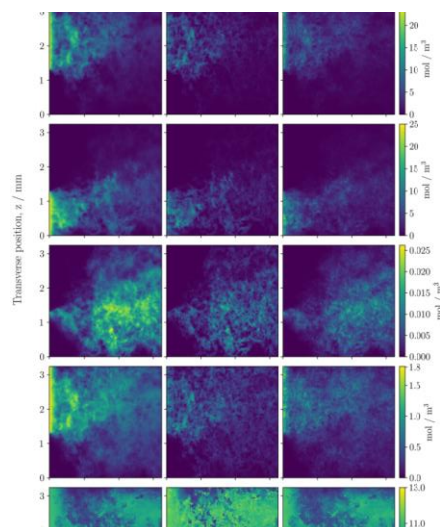


Figure 1-45 Profiles of concentration distribution in the pore space.

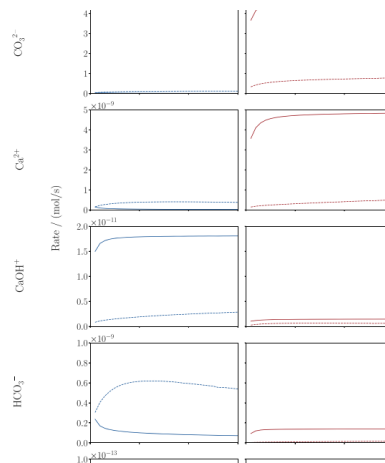


Figure 1-46 Distribution of reaction rates of formation (left) and consumption (right).

López and Smith (1996) investigated the fluid flow in fault zones and illustrated the heat transfer under heterogeneous fluid. Short-wavelength spatial variations appeared in the temperature field when heterogeneity was in the fault zone as can be seen in Figure 1-47(a). Heterogeneities had obvious difference compared with homogeneities in geothermal gradient deviations in the fault plane as shown in vertical profiles Figure 1-47(b).

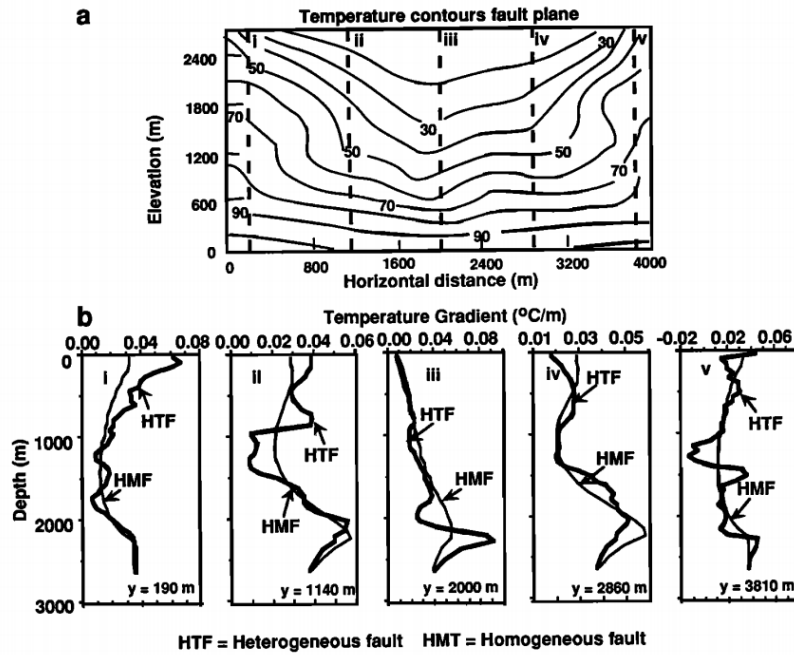


Figure 1-47 Features of the temperature field for the different flow system (a)

Temperature distribution in the fault zone. (b) Gradient of temperature with depth in the vertical direction.

Flow homogeneity

As an idealized flow, homogeneous isotropic turbulence (HIT) includes all of the basic physical processes of turbulence. Unlike heterogeneous turbulence contains complications such as mean shear, density stratification, and fluid–solid boundaries. Therefore, it is commonly used to reveal some of fundamental mechanisms of the turbulence flow, which are qualitatively independent of the origin of a specific flow system (Bellani and Variano, 2014).

The homogeneous shear flow is statistically steady with constant characteristic time and length scales. Two parameters play a key role in controlling the homogeneous shear flow are the Taylor–Reynolds number $Re_\lambda = \sqrt{5/(v\epsilon)} \langle u_\alpha u_\alpha \rangle$ and the shear strength $S^* = S \langle u_\alpha u_\alpha \rangle / \epsilon$ (Gualtieri et al., 2009).

Figure 1-48 showed the homogeneity spatial distribution of mean velocities with different locations, it also gave the magnitude of velocity fluctuations (rms velocity). The velocity profiles indicated that the mean and rms velocities are homogeneous over the centre region of the tank (Bellani and Variano, 2014).

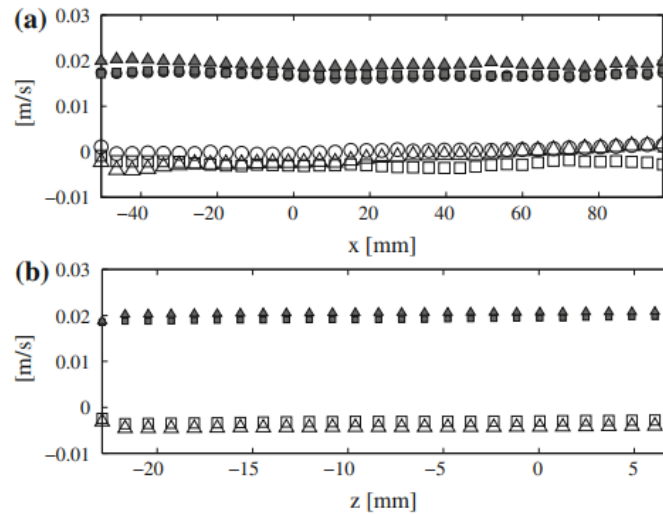


Figure 1-48 One-point velocity data obtained with S-PIV on the (a) x-y plane and (b) y-z plane, both are averaged over y. $\langle U \rangle (\circ)$, $\langle V \rangle (\square)$, $\langle W \rangle (\triangle)$.

Gu et al. (2017) investigated the effects of impellers and particle size on the degree of homogeneity of the mixing system. When increasing the impeller speed, the degree of homogeneity increased, large number of solid particles were suspended into the liquid phase as shown in Figure 1-49. Figure 1-50 demonstrated the homogeneity degree decreased with the increase of particle size. This can be attributed to the free settling velocity (V_t) for spherical particle (Hosseini et al., 2010):

$$V_t = \left[\frac{4gd_p(\rho_s - \rho_l)}{3C_D\rho_l} \right]^{\frac{1}{2}} \quad (1 - 20)$$

where the g is the gravity acceleration, d_p is the diameter of particle, ρ_s is the solid density, ρ_l is the liquid density, and C_D is the drag coefficient.

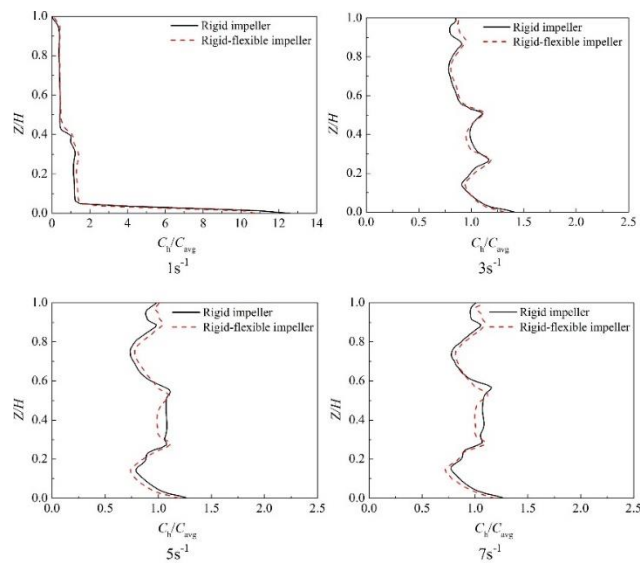


Figure 1-49 Effect of impeller speed on axial solid concentration profile .

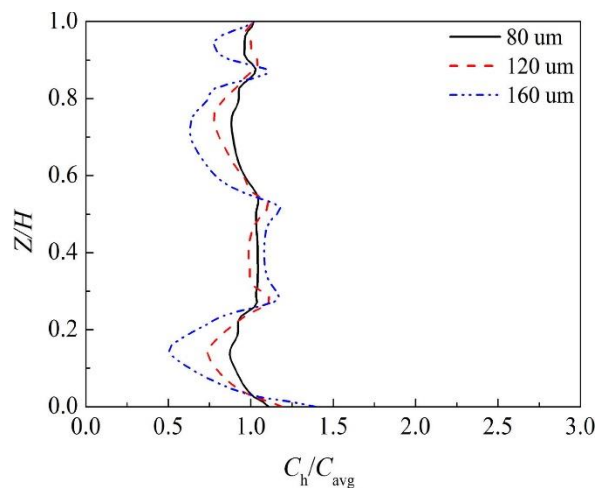


Figure 1-50 Axial solid concentration profile under different particle size.

Shear turbulence generation

Each geometrical reactor system described above has its own advantages. For continuous stirring tank reactor, the selection of impeller and its operation have a

significant effect in the generation of turbulence flow regime, as the axial velocity reaches the maxima near the impeller blade (Verma et al., 2019).

The Taylor-Couette system consists of two concentric cylinders where the turbulence shear is created. When the angular velocity of inner cylinder is high enough to a certain threshold, Couette flow becomes unstable and transforms into Taylor vortex flow, a secondary steady state. With the further increase of the cylinder angular speed, a much more complex state emerges called wavy vortex flow. If the two cylinders rotate in opposite sense, then spiral vortex flow arises. Beyond a certain Reynolds number there is the onset of turbulence. If two cylinders rotate in opposite directions, a spiral vortex is created. Turbulence appears when beyond a certain Reynolds number (Andereck et al., 1986).

For swirling impinging flow reactor, the main concept is the tangential velocity component as it introduces the swirling vortex flow. A typical swirling vortex flow usually has a core region acting as a solid body rotation and a free vortex region that away from the centre, the combination is regarded as Rankine vortex (Uddin et al., 2019).

1.4 Modelling of hydrodynamics in the process of mesoporous micro/nano particles synthesis

For mesoporous micro/nano particle synthesis process, its hydrodynamic characteristics can be modelled. Our study focused on one-way coupling simulation in which the particles have no interaction with the fluid due to the low volume fraction 1.1% and the fluid is assumed to be incompressible. However, fluid-particle coupling is very important in dense flows in industrial processes, which requires two-way

coupling simulation (Patel et al., 2017). In the two-fluid model, the volumetric interfacial area, also known as interfacial area concentration, plays a very important role in determine the intensity of interphase mass, momentum and energy transfer intensity (Yao and Morel, 2004).

1.4.1 Interfacial momentum transfer

Momentum always goes “downhill” from a high velocity region to a low velocity region. The velocity gradient can therefore be regarded as a “driving force” for momentum transport (Bird, 2002).

In momentum equations, the interface momentum force is usually added as the source term. Among other interfacial forces, the major forces include the drag force ($F_{l \rightarrow g}^D$), the lift force ($F_{l \rightarrow g}^L$), the wall lubricant force ($F_{l \rightarrow g}^{WL}$), the virtual mass force ($F_{l \rightarrow g}^{VM}$) and turbulent dispersion force ($F_{l \rightarrow g}^{TD}$). Interfacial momentum forces are usually added as source terms in the momentum equation (Khan et al., 2020).

$$M_{l \rightarrow g} = F_{l \rightarrow g}^D + F_{l \rightarrow g}^L + F_{l \rightarrow g}^{WL} + F_{l \rightarrow g}^{VM} + F_{l \rightarrow g}^{TD} \quad (1 - 21)$$

The viscous effect, decelerating effect, or accelerating effect of the dispersed phase (bubble, droplet, or solid particle) in a continuous relative fluid are known as drag forces, which is given by:

$$F_{l \rightarrow g}^D = -\frac{1}{2} \rho_l C_D \|U_{relative}\| (U_{relative}) (A_i) \quad (1 - 22)$$

$$U_{relative} = U_g - U_l$$

where C_D is the drag coefficient which is dependent on the volume fraction and the type of flow.

The lift force refers to the force applied on the dispersed phase due to velocity gradients in the liquid phase, is given by the following equation:

$$F_{l \rightarrow g}^L = -C_L \rho_l \alpha_g (U_g - U_l) \times (\nabla \times U_l) \quad (1 - 23)$$

where C_L is the lift force coefficient.

In some cases, the dispersed phase tends to concentrate in a region near the wall, but not immediately adjacent to the wall. The wall lubrication force can be used to describe this effect, which tends to push the dispersed phase away from the wall, given by the following equation (Liu et al., 2015b):

$$F_{l \rightarrow g}^{WL} = -C_{WL} \rho_l \alpha_g |U_{relative}|^2 \hat{n} \quad (1 - 24)$$

where C_{WL} is the coefficient of wall lubrication force, and \hat{n} is the outward vector normal to the wall.

Considering the acceleration of liquid by virtual mass force, the kinetic energy of dispersed phase is obtained as following equation,

$$F_{l \rightarrow g}^{VM} = C_{VM} \rho_l \alpha_g \left(\frac{d_g U_g}{dt} - \frac{d_l U_l}{dt} \right) \quad (1 - 25)$$

where C_{VM} is the virtual mass force coefficient.

Due to turbulent fluctuations, turbulent dispersion force leading to additional dispersion of phases from high-volume fraction regions to low-volume fraction regions, which is described as (Lubchenko et al., 2018),

$$F_{l \rightarrow g}^{TD} \propto grad \alpha_g \quad (1 - 26)$$

1.4.2 Interfacial mass transfer

Multi-mass transfer is the precondition of multi-phase reaction, so it has been widely studied. From the early naked measurement of the overall mass transfer coefficient to the in-depth understanding of the mass transfer mechanism. In general, mass transfer

is highly dependent on the recirculation pattern within the slug of the dispersed droplet or continuous phase (Zhao et al., 2021).

In industrial-chemical engineering applications of energy or raw material transformation, solid and fluid phase interactions are prominent. When two phases come into contact, mass transfer appears between them (Sulaiman et al., 2019). Suspension of solid phase in liquid phase is a practical method to promote mass transfer effect, as mass transfer needs interfacial area and can be enlarged by relative motion between solid and liquid (Derksen, 2014). The driving force for mass transfer is the concentrations difference between solid and fluid. The mass transfer coefficient between bulk fluid and particle surface increases as the velocity of fluid relative to particle increases (Bird, 2002).

The volumetric mass transfer coefficient $k_L \cdot a$ (l/s) consists of by a hydrodynamic term (k_L) and a morphology area term (a), as demonstrated in Figure 1-51 (Hissanaga et al., 2020).

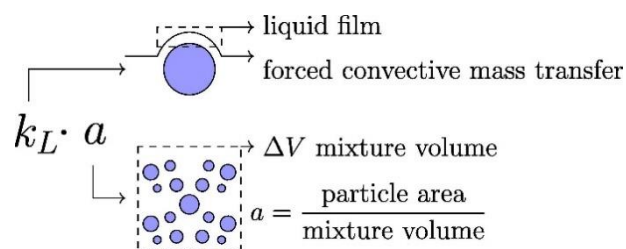


Figure 1-51 Illustration of mass transfer coefficient k_L and specific interfacial area a .

Take gas and liquid model as example, several theoretical models for calculating mass transfer coefficients k_L are proposed. Among them, the Two-film model proposed by Whitman is commonly used. A two-film model is usually used to determine the mass

transfer coefficient. With the assumption that the steady-state gas-liquid mass transfer can be modelled by the diffusion of molecules on two stagnant membranes on both sides of the gas-liquid interface, and the liquid-side mass transfer coefficient can be described as (Li et al., 2020),

$$k_l = \frac{D}{\delta_f} \quad (1 - 27)$$

where D is the species molecular diffusivity and δ_f is the thickness of liquid film. However, in various gas-liquid contacting reactors the Two-film model may be limited. The following models gives wide range of applications. In Higbie's penetration model, the continuous displacement of liquid elements at the gas-liquid interface resulted in surface renewal surface, which can be expressed as (Higbie, 1935),

$$k_l = \frac{2}{\sqrt{\pi}} \sqrt{\frac{D}{t_e}} \quad (1 - 28)$$

where t_e is the exposure time as a constant value.

Based on the surface renewal model, Danckwerts (1951) further proposed a modified penetration model. The mass transfer coefficient is obtained by the introduction of surface-age distribution function $\phi(t)$ expressed by the following equations

$$\int_0^{\infty} \phi(t) dt = 1 \quad (1 - 29)$$

$$\phi(t) = s e^{-st} \quad (1 - 30)$$

$$k_l = \sqrt{Ds} \quad (1 - 31)$$

where s is the liquid surface renewal rate.

Banerjee et al. (1968) assumed that the fresh fluid flow first carried to the surface by small eddies, at the same time deflected by the surface. And molecular diffusion can

help mass transfer through the surface. Therefore, the mass transfer coefficient was expressed as

$$k_l = K \sqrt{\frac{Dv}{l}} \quad (1 - 32)$$

where v and l are the velocity scale and length scale of eddies in the viscous dissipation range.

According to the first similarity hypothesis of Kolmogorov, viscous dissipation of energy per unit mass (ε) and the kinematic viscosity (ν) can be used to calculate v and l , given as,

$$l = \left(\frac{\nu^3}{\varepsilon}\right)^{1/4} \quad (1 - 33)$$

$$v = (\nu\varepsilon)^{1/4} \quad (1 - 34)$$

then Equation 1-32 can be rewritten in

$$k_l = KD^{1/2} \left(\frac{\varepsilon}{\nu}\right)^{1/4} \quad (1 - 35)$$

Li et al. (2020) further proposed a new eddy cell model, which takes the surface deformation power per unit mass $d(\sigma A_s)/mdt$,

$$\varepsilon_m = \varepsilon - \frac{\sigma dA_s + A_s d\sigma}{mdt} \quad (1 - 36)$$

$$k_l = D^{1/2} \left(\frac{\varepsilon}{\nu} - \frac{\sigma dA_s + A_s d\sigma}{m\nu dt}\right) \quad (1 - 37)$$

1.4.3 Modelling of chemical reaction taking place in the SiO₂ mesoporous particle synthesis

Descriptions of synthesis reaction

Through the sol-gel process, pure and homogenous products can be obtained at moderate conditions, which is an attractive method in synthesis silica, glass, and ceramic materials. For the formation of silica, the process consists of hydrolysis and condensation of metal alkoxides (Si(OR)₄) such as tetraethylorthosilicate (TEOS, Si(OC₂H₅)₄) or inorganic salts such as sodium silicate (Na₂SiO₃) under the acid (e.g., HCl) or base (e.g., NH₃) conditions. A general flow chart of sol-gel process for the production of silica with the adoption of silicon alkoxides (Si(OR)₄) is shown in Figure 1-52 (Davtyan et al., 2012).

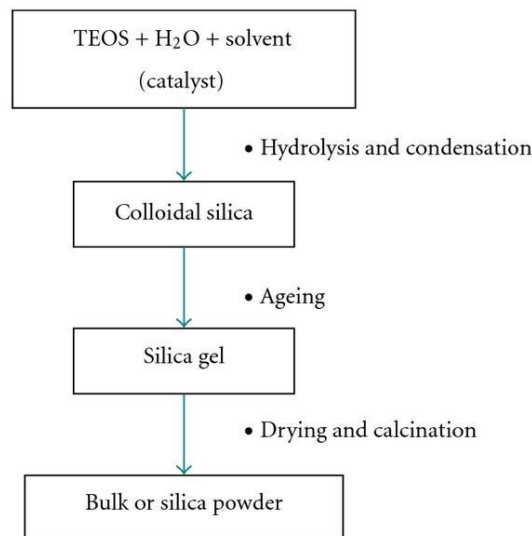
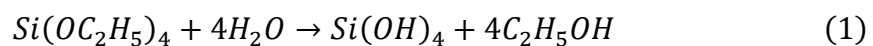
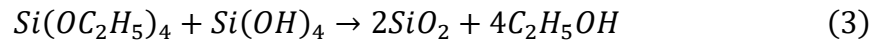


Figure 1-52 Flow chart of a typical sol-gel process.

In the sol-gel process, the general reactions of TEOS that results in the generation of silica particles can be described as (Guo et al., 2021),





For illustrating the mechanism of silica, the addition and controlled aggregation have been proposed. The monomer addition model describes the particle growth that happens when hydrolysed monomers add to the primary particle surface after an initial nucleation burst. In contrast, the nucleation process occurs continuously during the reaction in the aggregation model and secondary particles are formed due to the aggregation of the primary particles (Rahman and Padavettan, 2012).

1.4.4 Numerical simulation of mesoporous micro particle transport in turbulence shear generation reactors

In recent years, people have been working on investigated the accurate and stable numerical techniques and algorithms. Computational fluid dynamics (CFD) is an significant design tool that has been applied to various industrial fields, and it has shown its ability to accurately predict certain chemical processes (Ahmed et al., 2012). At present, there are three main methods for CFD simulation: Euler-Lagrange method and Euler-Euler method (Liu et al., 2013).

There are many variants of the Euler and Lagrange methods, however, the basic physical essence is the same, but the Euler method elaborates on it conceptually, while the Lagrange method still approaches it. Therefore, when Eulerian approach take the status of models, it becomes much more complex, and the Lagrange approach is essentially for simulations. Since the governing equations of Eulerian-Lagrange and Eulerian-Eulerian methods are obtained by averaging or filtering the basic

Navier-Stokes and Newton-Euler equations, they are necessarily approximate (Balachandar, 2020).

Eulerian- Eulerian approach

Eulerian-Eulerian approaches do not need to track individual particles which makes them computationally less expensive than Eulerian-Lagrange approaches. In contrast, they solve for a reduced, kinetic description for the particle phase regardless of the heat and mass transfer between interphases (Patel et al., 2017).

The dispersed particles are treated as a continuous phase when using Eulerian-Eulerian model. It directly predicts the particle concentration and a mechanical description of the inter-phase interactions. However, there exists some disadvantages, such as the interactions between particles and walls are difficult to be simulated precisely because particles are regarded as a continuous phase (Yan et al., 2020).

As a two-fluid approach, additional closure models are needed for the averaging of both phases. As the complexity increases, the closure models of force and torque for interphase momentum coupling are different from the ones adopted in Eulerian-Lagrange approach (Balachandar, 2020).

Eulerian- Lagrange approach

Eulerian-Lagrange methods use Newton's Laws to solve the trajectory of each particle that represented as discrete points (Patel et al., 2017). Model of soft-sphere or

hard-sphere can be used to describe the collisions between particles (Oevermann et al., 2009). Other variables such as temperature and gas concentration calculated using the energy and mass transfer equations for each particle. By using Eulerian–Lagrange approach the accuracy of simulation improved a lot due to the trajectory of each particle, but large quantity of computational resources is also needed at the same time. When it comes to large-scale fluidized bed systems which typically contain millions of particles, this approach may not be feasible (Gerber et al., 2010).

The big difference on modelling the effect of turbulent dispersion on particle transport between Eulerian–Lagrange approach and Eulerian-Eulerian approach is the addition of eddy fluctuating component onto the mean air velocity. As a fluctuating component of the air velocity, it leads to the dispersion of particles in turbulent flow. Consequently, the local air velocity can be rewritten in the following form (Yan et al., 2020),

$$\vec{U}_a = \bar{U}_a + \Phi \left(\frac{2k}{3} \right)^{0.5} \quad (1 - 38)$$

where Φ is a normally distributed random number which is related to the randomness of turbulence mean value.

1.4.5 Turbulence modelling

k – ε model

k – ε model is the most widely used model to simulate turbulent fluid mean flow characteristics used in CFD simulation. This two equations model is an alternative to algebraically determine the turbulent length scales from mild to high complexity

systems and focuses on the mechanisms that influence the turbulent kinetic energy which is an improvement of the mixing-length model (Versteeg and Malalasekera, 2007).

For an incompressible Newtonian fluid, the turbulence kinetic energy k and the turbulence dissipation ε transport equations are solved (Oualha et al., 2013):

$$\frac{\partial(\rho k)}{\partial(t)} + \text{div}(\rho k U) = \text{div}\left(\frac{\mu_t \overrightarrow{\text{grad}k}}{\sigma_k}\right) + 2\mu_t E_{ij} \cdot E_{ij} - \rho \varepsilon \quad (1 - 39)$$

$$\frac{\partial(\rho \varepsilon)}{\partial(t)} + \text{div}(\rho \varepsilon U) = \text{div}\left(\frac{\mu_t \overrightarrow{\text{grad}\varepsilon}}{\sigma_\varepsilon}\right) + C_{\varepsilon 1} \frac{\varepsilon}{k} 2\mu_t E_{ij} \cdot E_{ij} - C_{\varepsilon 2} \rho \frac{\varepsilon^2}{k} \quad (1 - 40)$$

The underlying conception is that the turbulent viscosity is isotropic, that means the ratio between mean strain rate and Reynolds stress is the same in all directions.

$$E_{ij} = \frac{1}{2} \left[\frac{\partial U_i}{\partial x_j} + \frac{\partial U_j}{\partial x_i} \right] \quad (1 - 41)$$

$$\mu_t = \rho C_\mu \frac{k^2}{\varepsilon} \quad (1 - 42)$$

The constants used in above equations are:

$$C_\mu = 0.09, C_{\varepsilon 1} = 1.44, C_{\varepsilon 2} = 1.92, \sigma_k = 1.0, \sigma_\varepsilon = 1.3$$

Vanaki et al. (2014) chose the $k - \varepsilon$ turbulence model to stimulate the flow fields in wavy channel. In order to illustrate impact of the concentration and shapes of silica nanoparticles on heat transfer and fluid flow characteristics. Similarly, Yuan et al. (2019) modelled a nanoparticle dispersion system using $k - \varepsilon$ turbulence model. The results showed that the turbulent shear force is stronger near the nozzle, which is the main mechanism for nanoparticles deagglomeration. Oualha et al. (2013) studied the mixing of fluids in a T-mixer for synthesis of the sol-gel TiO₂ nanoparticles. In

their work, $k - \varepsilon$ model was adopted to simulate the fluid velocity field at different impingement angle.

Reynolds stress model

Reynolds stress model (RSM) is the most complex and general classical turbulence model, also termed the second-order model. For many simple and complex flows, such as wall jets, asymmetric and non-circular pipe flows and curved flows, it performs well at mean flow characteristics and all Reynolds stress. Only initial and/or boundary conditions need to be given (Versteeg and Malalasekera, 2007). Instead of only the turbulent kinetic energy ε , six independent components of the Reynolds stress tensor are introduced by RSM, convective term, production term, rotational term, diffusion term, dissipation rate term and pressure-strain term.

Bahiraee et al. (2021) modelled the turbulent nanofluid using Reynolds stress model to analyse the heat transfer in heat exchanger which can provide superior accuracy than ordinary two-equation models. Due to its ability to capture the turbulence anisotropy, Mehel et al. (2010) chose the RSM combined with enhanced wall treatment to investigate wall deposition of micro/nano particles in a turbulent flow.

Rodi (1976) had developed an algebraic Reynolds stress model where the Reynolds stresses are dependent on the velocity field. The ARSM formulation includes the approximated convection and diffusion terms in some way so that the Reynolds stress tensor turns to algebraic in the modelled differential equation. The ARSM represents the anisotropy of the Reynolds stresses more accurately than the linear gradient model usually employed in the $k - \varepsilon$ model since the formulation captures the important physical processes (Taulbee, 1992).

An explicit algebraic Reynolds stress model was further developed where the Reynolds stresses are explicitly determined by the mean flow field. This results in a more numerically robust model and a negligible effect on the computational effort compared to $k - \varepsilon$ model (Wallin and Johansson, 2000). One of the disadvantages of explicit algebraic Reynolds stress models is that they do not naturally account for swirling and rotating flows.

Large eddy simulation

As the RANS equations does not seem able to give the effect of the large scales of turbulence in the same way when flows are quite different, a new numerical method needs to be developed for large flow features (Piomelli, 1999).

Large-eddy simulation is a technique that superficially on the middle ground between the direct simulation and Reynold-average simulation first proposed in 1963 by Smagorinsky (1963). LES is found to be satisfactory, because turbulent mass transfer, momentum transfer, and energy transfer, drag force, interspecies entrainment are determined mainly by the macroscopic variables $\bar{\rho}(x, t)$, $\bar{u}(x, t)$, $\bar{P}(x, t)$ which turned to be adequate accuracy in computation (Boris et al., 1992). The basic concept of LES is about the local time and spatial filter operation. To separate the large from the small scales, a filtered variable is defined as follows,

$$\bar{f}(x, t) \equiv \int f(x', t) \bar{F}(x - x') dx' \quad (1 - 43)$$

where $\bar{F}(x - x')$ is a filter function and $f(x', t)$ is the residual component. According to the definition, one can tell those filtered variables almost have no short wavelength structure due to the filtering operation.

LES has wide applications, usually used on homogeneous turbulent flows, free shear flows, plane channel flows. With the development of new models, it now can also

apply to engineering-like applications, such as combustion, acoustics and simulations of the atmospheric boundary layer (Piomelli, 1999). According to Zhang and Kleinstreuer (2011), LES modelling had great performance on computational fluid-particle dynamics. The instantaneous velocity fluctuations provided by LES might be important for turbulent micron particle transport/deposition in the respiratory tract. Sung et al. (2011) synthesised the TiO₂ nanoparticles in a turbulent flame reactor. To accurately describe the turbulent flame behaviour LES was used for simulation, which exhibited better performance than RANS models.

1.5 Recapitulation and concluding remarks

Chapter 1 gives an elaborate review on the shear turbulence controllable synthesis of mesoporous meso/nano particles, it consists of three aspects: the synthesis approaches, various reactor systems and numerical modelling. In particular, in this study we focus on the synthesis process including types and characteristics of reactor, as well as turbulence generation.

As mentioned above, the shear controllable approach has better performance than other conventional approaches on synthesis micro/nano particles. In contrast to conventional batch systems, it is widely studied due to accurate control, high heat and mass transfer rate, intensive mixing performance, large reaction interaction surfaces, and compatibility with online analysis. Shear controllable synthesis can produce products with different properties only by changing hydrodynamic conditions without the need for further additional chemicals, which makes it safe green and environment amity.

In section 3, four types of reactor systems are discussed. The ways of inducing mixing are quite different among them. The mixing of continuous stirring tank reactor is mainly dependent on the impeller, and the residence time distribution is usually used to characterise the behaviour of CSTR. For the Taylor-Couette reactor, a closed and bounded flow system, the turbulence generation depends on the angular velocities of two rotating cylinders. The mixing occurs in the impinging jet reactor when two high-velocity streams collide. At high velocity, turbulence flow is created. Similarly, the main concept of swirling impinging flow reactor is the tangential velocity component as it introduces the swirling vortex flow.

Computational fluid dynamics is also conducted to illustrate the flow characteristics in the reactor. Normally, the two-phase model is employed for fluid-particle flow. However, in this case, we only consider the one-way coupling due to the very low volume fraction of particles (1.1%).

Through this review, it seems that a little work was done in combining the shear turbulence controllable with the synthesis of micro/nano particles and a deeper understanding is required. Based on these theoretical understandings, the focus of this dissertation will be research on micro/nano particles synthesis and fluid numerical simulation inside a counter swirling impinging flow reactor.

References

- AHMED, T. Y., AHMAD, M. M., YUSUP, S., INAYAT, A. & KHAN, Z. 2012. Mathematical and computational approaches for design of biomass gasification for hydrogen production: A review. *Renewable and Sustainable Energy Reviews*, 16, 2304-2315.
- AL-HADA, N. M., SAION, E. B., SHAARI, A. H., KAMARUDIN, M. A., FLAIFEL, M. H., AHMAD, S. H. & GENE, S. A. 2014. A facile thermal-treatment route to synthesize ZnO nanosheets and effect of calcination temperature. *PloS one*, 9, e103134.
- ALAMER, M., LIM, A. R. & JOO, Y. L. 2018. Continuous synthesis of structurally uniform graphene oxide materials in a model Taylor–Couette flow reactor. *Industrial & Engineering Chemistry Research*, 58, 1167-1176.
- ANDERECK, C. D., LIU, S. & SWINNEY, H. L. 1986. Flow regimes in a circular Couette system with independently rotating cylinders. *Journal of fluid mechanics*, 164, 155-183.
- AZLINA, H., HASNIDAWANI, J., NORITA, H. & SURIP, S. 2016. Synthesis of SiO₂ nanostructures using sol-gel method. *Acta Phys Pol A*, 129, 842-844.
- BABER, R., MAZZEI, L., THANH, N. T. & GAVRIILIDIS, A. 2016. Synthesis of silver nanoparticles using a microfluidic impinging jet reactor. *Journal of Flow Chemistry*, 6, 268-278.
- BAHIRAEI, M., MAZAHERI, N. & HANOONI, M. 2021. Performance enhancement of a triple-tube heat exchanger through heat transfer

- intensification using novel crimped-spiral ribs and nanofluid: A two-phase analysis. *Chemical Engineering and Processing-Process Intensification*, 160, 108289.
- BALACHANDAR, S. 2020. Lagrangian and Eulerian drag models that are consistent between Euler-Lagrange and Euler-Euler (two-fluid) approaches for homogeneous systems. *Physical Review Fluids*, 5, 084302.
- BANERJEE, S., SCOTT, D. & RHODES, E. 1968. Mass transfer to falling wavy liquid films in turbulent flow. *Industrial & Engineering Chemistry Fundamentals*, 7, 22-27.
- BELLANI, G. & VARIANO, E. A. 2014. Homogeneity and isotropy in a laboratory turbulent flow. *Experiments in fluids*, 55, 1-12.
- BIRD, R. B. 2002. Transport phenomena. *Appl. Mech. Rev.*, 55, R1-R4.
- BOAL, A. K., ILHAN, F., DEROUCHÉY, J. E., THURN-ALBRECHT, T., RUSSELL, T. P. & ROTELLO, V. M. 2000. Self-assembly of nanoparticles into structured spherical and network aggregates. *Nature*, 404, 746-748.
- BORIS, J., GRINSTEIN, F., ORAN, E. & KOLBE, R. 1992. New insights into large eddy simulation. *Fluid dynamics research*, 10, 199.
- BOUNAB, N., DUCLAUX, L., REINERT, L., OUMEDJBEUR, A., BOUKHALFA, C., PENHOUD, P. & MULLER, F. 2021. Improvement of zero valent iron nanoparticles by ultrasound-assisted synthesis, study of Cr (VI) removal and application for the treatment of metal surface processing wastewater. *Journal of Environmental Chemical Engineering*, 9, 104773.

- CARVER, J. A. & ROLLMAN, W. F. 1956. Method and apparatus for mixing and contacting fluids. Google Patents.
- CHENG, Y., YE, A., LIU, F. & WEI, F. 2006. Numerical simulation of swirling flows in oxidation reactors for TiO₂ manufacture. *China Particuology*, 4, 108-113.
- CUI, H., WEBBER, M. J. & STUPP, S. I. 2010. Self - assembly of peptide amphiphiles: From molecules to nanostructures to biomaterials. *Peptide Science: Original Research on Biomolecules*, 94, 1-18.
- DANCKWERTS, P. 1951. Significance of liquid-film coefficients in gas absorption. *Industrial & Engineering Chemistry*, 43, 1460-1467.
- DAVTYAN, S. P., BERLIN, A., AGABEKOV, V. & LEKISHVILI, N. 2012. Synthesis, properties, and applications of polymeric nanocomposites. Hindawi.
- DEHGHANGHADIKOLAEI, A., ANSARY, J. & GHOREISHI, R. 2018. Sol-gel process applications: A mini-review. *Proc. Nat. Res. Soc*, 2, 02008.
- DERKSEN, J. 2014. Simulations of solid-liquid mass transfer in fixed and fluidized beds. *Chemical Engineering Journal*, 255, 233-244.
- FATIMAH, I., HIDAYAT, H., NUGROHO, B. H. & HUSEIN, S. 2020. Ultrasound-assisted biosynthesis of silver and gold nanoparticles using *Clitoria ternatea* flower. *South African Journal of Chemical Engineering*, 34, 97-106.
- FENG, S. & XU, R. 2001. New materials in hydrothermal synthesis. *Accounts of chemical research*, 34, 239-247.

- GAO, Y., HE, Y., ZHANG, H., ZHANG, Y., GAO, T., WANG, J.-H. & WANG, S. 2021. Zwitterion-functionalized mesoporous silica nanoparticles for enhancing oral delivery of protein drugs by overcoming multiple gastrointestinal barriers. *Journal of Colloid and Interface Science*, 582, 364-375.
- GAVI, E., MARCHISIO, D. L. & BARRESI, A. A. 2007a. CFD modelling and scale-up of confined impinging jet reactors. *Chemical engineering science*, 62, 2228-2241.
- GAVI, E., RIVAUTELLA, L., MARCHISIO, D., VANNI, M., BARRESI, A. & BALDI, G. 2007b. CFD modelling of nano-particle precipitation in confined impinging jet reactors. *Chemical Engineering Research and Design*, 85, 735-744.
- GERBER, S., BEHRENDT, F. & OEVERMANN, M. 2010. An Eulerian modeling approach of wood gasification in a bubbling fluidized bed reactor using char as bed material. *Fuel*, 89, 2903-2917.
- GRZELCZAK, M., VERMANT, J., FURST, E. M. & LIZ-MARZÁN, L. M. 2010. Directed self-assembly of nanoparticles. *ACS nano*, 4, 3591-3605.
- GU, D., LIU, Z., QIU, F., LI, J., TAO, C. & WANG, Y. 2017. Design of impeller blades for efficient homogeneity of solid-liquid suspension in a stirred tank reactor. *Advanced Powder Technology*, 28, 2514-2523.
- GUALTIERI, P., PICANO, F. & CASCIOLA, C. 2009. Anisotropic clustering of inertial particles in homogeneous shear flow. *Journal of Fluid Mechanics*, 629, 25-39.

- GUO, Y., YANG, X., LI, G., YANG, J., LIU, L., CHEN, L. & LI, B. 2021. Shear turbulence controllable synthesis of aggregated nano-particles using a swirling vortex flow reactor assisted by ultrasound irradiation. *Chemical Engineering Journal*, 405, 126914.
- HAI, L., JIA, X., HE, D., ZHANG, A., WANG, T., CHENG, H., HE, X. & WANG, K. 2018. DNA-functionalized hollow mesoporous silica nanoparticles with dual cargo loading for near-infrared-responsive synergistic chemo-photothermal treatment of cancer cells. *ACS Applied Nano Materials*, 1, 3486-3497.
- HIGBIE, R. 1935. Penetration theory leads to use of the contact time in the calculation of the mass transfer coefficients in the two film theory. *Trans. Am. Inst. Chem. Engrs* 31, 365.
- HISSANAGA, A., PADOIN, N. & PALADINO, E. 2020. Mass transfer modeling and simulation of a transient homogeneous bubbly flow in a bubble column. *Chemical Engineering Science*, 218, 115531.
- HOSEINI, S., NAJAFI, G., GHOBADIAN, B. & AKBARZADEH, A. 2021. Impeller shape-optimization of stirred-tank reactor: CFD and fluid structure interaction analyses. *Chemical Engineering Journal*, 413, 127497.
- HOSSEINI, S., PATEL, D., EIN-MOZAFFARI, F. & MEHRVAR, M. 2010. Study of solid– liquid mixing in agitated tanks through computational fluid dynamics modeling. *Industrial & Engineering Chemistry Research*, 49, 4426-4435.
- HU, Y., QIN, Y., QIU, C., XU, X., JIN, Z. & WANG, J. 2020. Ultrasound-assisted self-assembly of β -cyclodextrin/debranched starch nanoparticles as promising

- carriers of tangeretin. *Food Hydrocolloids*, 108, 106021.
- JEON, B., SHIN, J. & SHIN, D. Design Factors of a Plasma Reactor with a Swirling Flow Field for Production of Rutile TiO₂ Nanoparticles. *Proceedings of International Conference of Aerospace and Mechanical Engineering 2019*, 2020. Springer, 219-231.
- JIANG, W., ZHOU, H., CAO, Y., NIE, J., LI, Y., ZHAO, Y., KAWASAKI, M., LANGDON, T. G. & ZHU, Y. 2020. On the Heterogeneity of Local Shear Strain Induced by High - Pressure Torsion. *Advanced Engineering Materials*, 22, 1900477.
- KHAN, I., WANG, M., ZHANG, Y., TIAN, W., SU, G. & QIU, S. 2020. Two-phase bubbly flow simulation using CFD method: A review of models for interfacial forces. *Progress in Nuclear Energy*, 125, 103360.
- KHOSHOOEI, M. A., SCOTT, C. E., CARBOGNANI, L. & PEREIRA-ALMAO, P. 2021. Ultrasound-assisted bimetallic NiMo nanocatalyst preparation using microemulsions for in-situ upgrading application: Impact on particle size. *Catalysis Today*, 365, 132-141.
- KIM, J.-M., CHANG, S.-M., CHANG, J. H. & KIM, W.-S. 2011. Agglomeration of nickel/cobalt/manganese hydroxide crystals in Couette–Taylor crystallizer. *Colloids and Surfaces A: Physicochemical and Engineering Aspects*, 384, 31-39.
- KIM, W.-S. 2014. Application of Taylor vortex to crystallization. *Journal of Chemical Engineering of Japan*, 47, 115-123.

KOOPMANS, R.-J., SHRIMPSON, J. S., ROBERTS, G. T. & MUSKER, A. J. 2013.

A one-dimensional multicomponent two-fluid model of a reacting packed bed including mass, momentum and energy interphase transfer. *International journal of multiphase flow*, 57, 10-28.

LEE, J.-S. & CHOI, S.-C. 2004. Crystallization behavior of nano-ceria powders by hydrothermal synthesis using a mixture of H₂O₂ and NH₄OH. *Materials Letters*, 58, 390-393.

LI, B., WANG, X., YAN, M. & LI, L. 2003. Preparation and characterization of nano-TiO₂ powder. *Materials Chemistry and Physics*, 78, 184-188.

LI, W.-L., WANG, J.-H., LU, Y.-C., SHAO, L., CHU, G.-W. & XIANG, Y. 2020. CFD analysis of CO₂ absorption in a microporous tube-in-tube microchannel reactor with a novel gas-liquid mass transfer model. *International Journal of Heat and Mass Transfer*, 150, 119389.

LING, F. W., ABDULBARI, H. A. & CHIN, S.-Y. 2021. Synthesis and characteristics of silica nano-particles using modified sol-gel method in microreactor. *Materials Today: Proceedings*, 42, 1-7.

LIU, H., ELKAMEL, A., LOHI, A. & BIGLARI, M. 2013. Computational fluid dynamics modeling of biomass gasification in circulating fluidized-bed reactor using the Eulerian-Eulerian approach. *Industrial & Engineering Chemistry Research*, 52, 18162-18174.

LIU, N., CHEN, X., ZHANG, J. & SCHWANK, J. W. 2014. A review on TiO₂-based nanotubes synthesized via hydrothermal method: Formation mechanism,

- structure modification, and photocatalytic applications. *Catalysis Today*, 225, 34-51.
- LIU, Y., GU, J., ZHANG, J., WANG, J., NIE, N., FU, Y., LI, W. & YU, F. 2015a. Controllable synthesis of nano-sized LiFePO₄/C via a high shear mixer facilitated hydrothermal method for high rate Li-ion batteries. *Electrochimica Acta*, 173, 448-457.
- LIU, Z., QI, F., LI, B. & JIANG, M. 2015b. Multiple size group modeling of polydispersed bubbly flow in the mold: an analysis of turbulence and interfacial force models. *Metallurgical and Materials Transactions B*, 46, 933-952.
- LÓPEZ, D. L. & SMITH, L. 1996. Fluid flow in fault zones: Influence of hydraulic anisotropy and heterogeneity on the fluid flow and heat transfer regime. *Water resources research*, 32, 3227-3235.
- LUBCHENKO, N., MAGOLAN, B., SUGRUE, R. & BAGLIETTO, E. 2018. A more fundamental wall lubrication force from turbulent dispersion regularization for multiphase CFD applications. *International Journal of Multiphase Flow*, 98, 36-44.
- LYNCH, P., FIORE, G., KRIER, H. & GLUMAC, N. 2010. Gas-phase reaction in nanoaluminum combustion. *Combustion science and technology*, 182, 842-857.
- MA, J., LEE, S. M.-Y., YI, C. & LI, C.-W. 2017. Controllable synthesis of functional nanoparticles by microfluidic platforms for biomedical applications—a review.

- Lab on a Chip, 17, 209-226.
- MACWAN, D., DAVE, P. N. & CHATURVEDI, S. 2011. A review on nano-TiO₂ sol-gel type syntheses and its applications. *Journal of materials science*, 46, 3669-3686.
- MANCUSO, G. 2018. Experimental and numerical investigation on performance of a swirling jet reactor. *Ultrasonics sonochemistry*, 49, 241-248.
- MARCHISIO, D., BARRESI, A. & FOX, R. 2001. Simulation of turbulent precipitation in a semi - batch Taylor - Couette reactor using CFD. *AIChE Journal*, 47, 664-676.
- MARTINS, A. C., CAZETTA, A. L., PEZOTI, O., SOUZA, J. R., ZHANG, T., PILAU, E. J., ASEFA, T. & ALMEIDA, V. C. 2017. Sol-gel synthesis of new TiO₂/activated carbon photocatalyst and its application for degradation of tetracycline. *Ceramics International*, 43, 4411-4418.
- MEHEL, A., TANIÈRE, A., OESTERLÉ, B. & FONTAINE, J.-R. 2010. The influence of an anisotropic Langevin dispersion model on the prediction of micro-and nanoparticle deposition in wall-bounded turbulent flows. *Journal of Aerosol Science*, 41, 729-744.
- METAXAS, A., WILKINSON, N., RAETHKE, E. & DUTCHER, C. S. 2018. In situ polymer flocculation and growth in Taylor-Couette flows. *Soft matter*, 14, 8627-8635.
- MORSE, P. M. & INGARD, K. U. 1961. *Linear acoustic theory. Akustik I/Acoustics I*. Springer.

- MUSTAFA, A. G., MAJNIS, M. F. & MUTTALIB, N. A. A. 2020. CFD Study on Impeller Effect on Mixing in Miniature Stirred Tank Reactor. *CFD Letters*, 12, 15-26.
- NAGAVENI, K., SIVALINGAM, G., HEGDE, M. & MADRAS, G. 2004. Solar photocatalytic degradation of dyes: high activity of combustion synthesized nano TiO₂. *Applied Catalysis B: Environmental*, 48, 83-93.
- NARAYAN, R., NAYAK, U. Y., RAICHUR, A. M. & GARG, S. 2018. Mesoporous silica nanoparticles: A comprehensive review on synthesis and recent advances. *Pharmaceutics*, 10, 118.
- NETO, N. A., NUNES, T., LI, M., LONGO, E., BOMIO, M. & MOTTA, F. 2020. Influence of microwave-assisted hydrothermal treatment time on the crystallinity, morphology and optical properties of ZnWO₄ nanoparticles: Photocatalytic activity. *Ceramics International*, 46, 1766-1774.
- NGUYEN, A.-T., JOO, Y. L. & KIM, W.-S. 2012. Multiple feeding strategy for phase transformation of GMP in continuous Couette–Taylor crystallizer. *Crystal growth & design*, 12, 2780-2788.
- NGUYEN, A.-T., KIM, J.-M., CHANG, S.-M. & KIM, W.-S. 2011. Phase Transformation of Guanosine 5-Monophosphate in Continuous Couette–Taylor Crystallizer: Experiments and Numerical Modeling for Kinetics. *Industrial & engineering chemistry research*, 50, 3483-3493.
- NIEDERBERGER, M. 2007. Nonaqueous sol–gel routes to metal oxide nanoparticles. *Accounts of chemical research*, 40, 793-800.

- OEVERMANN, M., GERBER, S. & BEHRENDT, F. 2009. Euler–Lagrange/DEM simulation of wood gasification in a bubbling fluidized bed reactor. *Particuology*, 7, 307-316.
- OLIVEIRA, T. D., BLUNT, M. & BIJELJIC, B. 2020. Multispecies reactive transport in a microporous rock: impact of flow heterogeneity and reversibility of reaction.
- ORGILL, J. J., ATIYEH, H. K., DEVARAPALLI, M., PHILLIPS, J. R., LEWIS, R. S. & HUHNKE, R. L. 2013. A comparison of mass transfer coefficients between trickle-bed, hollow fiber membrane and stirred tank reactors. *Bioresource technology*, 133, 340-346.
- OUALHA, K., BOUAZIZ, S., JIA, Z., HADDAR, M., KANAIEV, A. & AMAR, M. B. 2013. Design of T-mixer with non-coaxial inputs for preparation of monodispersed nanoparticles. SFGP2013.
- PACHOLSKI, C., KORNOWSKI, A. & WELLER, H. 2002. Self - assembly of ZnO: from nanodots to nanorods. *Angewandte Chemie International Edition*, 41, 1188-1191.
- PAL, S., MADANE, K., MANE, M. & KULKARNI, A. A. 2021. Impingement Dynamics of Jets in a Confined Impinging Jet Reactor. *Industrial & Engineering Chemistry Research*, 60, 969-979.
- PARK, S.-A., LEE, S. & KIM, W.-S. 2015. Polymorphic crystallization of sulfamerazine in Taylor vortex flow: polymorphic nucleation and phase transformation. *Crystal Growth & Design*, 15, 3617-3627.

- PARK, S. & KIM, W.-S. 2018. Influence of fluid motions on polymorphic crystallization of L-histidine: Taylor vortex flow and turbulent Eddy flow. *Crystal Growth & Design*, 18, 710-722.
- PATEL, R. G., DESJARDINS, O., KONG, B., CAPECELATRO, J. & FOX, R. O. 2017. Verification of Eulerian–Eulerian and Eulerian–Lagrangian simulations for turbulent fluid–particle flows. *AIChE Journal*, 63, 5396-5412.
- PIOMELLI, U. 1999. Large-eddy simulation: achievements and challenges. *Progress in aerospace sciences*, 35, 335-362.
- RADZIUK, D., GRIGORIEV, D., ZHANG, W., SU, D., MÖHWALD, H. & SHCHUKIN, D. 2010. Ultrasound-assisted fusion of preformed gold nanoparticles. *The Journal of Physical Chemistry C*, 114, 1835-1843.
- RAHMAN, I. A. & PADAVETTAN, V. 2012. Synthesis of silica nanoparticles by sol-gel: size-dependent properties, surface modification, and applications in silica-polymer nanocomposites—a review. *Journal of Nanomaterials*, 2012.
- RAND, B. 1991. Calcination. *Concise Encyclopedia of Advanced Ceramic Materials*. Elsevier.
- RAY, A. K. & BEENACKERS, A. A. 1997. Novel swirl - flow reactor for kinetic studies of semiconductor photocatalysis. *AIChE Journal*, 43, 2571-2578.
- RODI, W. A new algebraic relation for calculating the Reynolds stresses. *Gesellschaft Angewandte Mathematik und Mechanik Workshop Paris France*, 1976. 219.
- SEENIVASAN, M., YANG, C.-C., WU, S.-H., CHIEN, W.-C., WU, Y.-S., JOSE, R.

- & LUE, S. J. 2021. Using a Couette–Taylor vortex flow reactor to prepare a uniform and highly stable Li [Ni_{0.80}Co_{0.15}Al_{0.05}] O₂ cathode material. *Journal of Alloys and Compounds*, 857, 157594.
- SHARMA, R., SARKAR, A., JHA, R., KUMAR SHARMA, A. & SHARMA, D. 2020. Sol - gel - mediated synthesis of TiO₂ nanocrystals: Structural, optical, and electrochemical properties. *International Journal of Applied Ceramic Technology*, 17, 1400-1409.
- SMAGORINSKY, J. 1963. General circulation experiments with the primitive equations: I. The basic experiment. *Monthly weather review*, 91, 99-164.
- SONALI, S., JENA, I. & ROUT, S. K. 2020. A comparative study of synthesis of ZnO nano particles: Hydrothermal and modified combustion routes. *Materials Today: Proceedings*, 33, 4966-4970.
- SULAIMAN, M., CLIMENT, E., HAMMOUTI, A. & WACHS, A. 2019. Mass transfer towards a reactive particle in a fluid flow: numerical simulations and modeling. *Chemical Engineering Science*, 199, 496-507.
- SUN, P., LEIDNER, A., WEIGEL, S., WEIDLER, P. G., HEISLER, S., SCHARNWEBER, T. & NIEMEYER, C. M. 2019. Biopebble Containers: DNA - Directed Surface Assembly of Mesoporous Silica Nanoparticles for Cell Studies. *Small*, 15, 1900083.
- SUNDARAM, D., YANG, V. & ZARKO, V. E. 2015. Combustion of nano aluminum particles. *Combustion, Explosion, and Shock Waves*, 51, 173-196.
- SUNG, Y., RAMAN, V. & FOX, R. O. 2011. Large-eddy-simulation-based multiscale

- modeling of TiO₂ nanoparticle synthesis in a turbulent flame reactor using detailed nucleation chemistry. *Chemical Engineering Science*, 66, 4370-4381.
- TABATABAEI, S., SHUKOHFAR, A., AGHABABAZADEH, R. & MIRHABIBI, A. Experimental study of the synthesis and characterisation of silica nanoparticles via the sol-gel method. *Journal of Physics: Conference Series*, 2006. IOP Publishing, 090.
- TAM, K., CHEUNG, C., LEUNG, Y., DJURIŠIĆ, A., LING, C., BELING, C., FUNG, S., KWOK, W. M., CHAN, W. & PHILLIPS, D. 2006. Defects in ZnO nanorods prepared by a hydrothermal method. *The Journal of Physical Chemistry B*, 110, 20865-20871.
- TANG, Z., KIM, W.-S. & YU, T. 2018. Continuous synthesis of silver plates in a continuous stirring tank reactor (CSTR). *Journal of Industrial and Engineering Chemistry*, 66, 411-418.
- TANG, Z., KIM, W.-S. & YU, T. 2019. Studies on morphology changes of copper sulfide nanoparticles in a continuous Couette-Taylor reactor. *Chemical Engineering Journal*, 359, 1436-1441.
- TAULBEE, D. B. 1992. An improved algebraic Reynolds stress model and corresponding nonlinear stress model. *Physics of Fluids A: Fluid Dynamics*, 4, 2555-2561.
- UDDIN, N., WEIGAND, B. & YOUNIS, B. A. 2019. Comparative study on heat transfer enhancement by turbulent impinging jet under conditions of swirl, active excitations and passive excitations. *International Communications in*

Heat and Mass Transfer, 100, 35-41.

VANAKI, S. M., MOHAMMED, H., ABDOLLAHI, A. & WAHID, M. 2014. Effect of nanoparticle shapes on the heat transfer enhancement in a wavy channel with different phase shifts. *Journal of Molecular Liquids*, 196, 32-42.

VAZQUEZ, N. I., GONZALEZ, Z., FERRARI, B. & CASTRO, Y. 2017. Synthesis of mesoporous silica nanoparticles by sol-gel as nanocontainer for future drug delivery applications. *Boletín de la Sociedad Española de Cerámica y Vidrio*, 56, 139-145.

VERMA, R., MEHAN, L., KUMAR, R., KUMAR, A. & SRIVASTAVA, A. 2019. Computational fluid dynamic analysis of hydrodynamic shear stress generated by different impeller combinations in stirred bioreactor. *Biochemical Engineering Journal*, 151, 107312.

VERSTEEG, H. K. & MALALASEKERA, W. 2007. *An introduction to computational fluid dynamics: the finite volume method*, Pearson education.

WALLIN, S. & JOHANSSON, A. V. 2000. An explicit algebraic Reynolds stress model for incompressible and compressible turbulent flows. *Journal of fluid mechanics*, 403, 89-132.

WOJTALIK, M., BOJARSKA, Z. & MAKOWSKI, Ł. 2020. Experimental studies on the chemical wet synthesis for obtaining high-quality MoS₂ nanoparticles using impinging jet reactor. *Journal of Solid State Chemistry*, 285, 121254.

WONGCHAREE, K., CHUWATTANAKUL, V. & EIAMSA-ARD, S. 2017. Heat transfer of swirling impinging jets with TiO₂-water nanofluids. *Chemical*

Engineering and Processing: Process Intensification, 114, 16-23.

WU, Z., SEOK, S., KIM, D. H. & KIM, W.-S. 2015. Control of crystal size distribution using non-isothermal Taylor vortex flow. *Crystal Growth & Design*, 15, 5675-5684.

XIAOXUE, J., DAN, L., SHUYAN, W., HASSAN, M., WENJIAN, C., WEIQI, C. & HUILIN, L. 2020. Comparative analysis of heterogeneous gas-solid flow using dynamic cluster structure-dependent drag model in risers. *International Journal of Multiphase Flow*, 122, 103126.

XU, C., LEI, C. & YU, C. 2019. Mesoporous silica nanoparticles for protein protection and delivery. *Frontiers in chemistry*, 7, 290.

YAN, Y., LI, X. & ITO, K. 2020. Numerical investigation of indoor particulate contaminant transport using the Eulerian-Eulerian and Eulerian-Lagrangian two-phase flow models. *Experimental and computational multiphase flow*, 2, 31-40.

YANG, G., LI, Z., WU, F., CHEN, M., WANG, R., ZHU, H., LI, Q. & YUAN, Y. 2020. Improving solubility and bioavailability of breviscapine with mesoporous silica nanoparticles prepared using ultrasound-assisted solution-enhanced dispersion by supercritical fluids method. *International journal of nanomedicine*, 15, 1661.

YAO, W. & MOREL, C. 2004. Volumetric interfacial area prediction in upward bubbly two-phase flow. *International Journal of Heat and Mass Transfer*, 47, 307-328.

YUAN, F., TU, C., YU, J. & CUI, Z. 2019. High-pressure dispersion of nanoparticle agglomerates through a continuous aerosol disperser. *Applied Nanoscience*, 9, 1857-1868.

ZHANG, Z. & KLEINSTREUER, C. 2011. Laminar - to - turbulent fluid - nanoparticle dynamics simulations: Model comparisons and nanoparticle - deposition applications. *International Journal for Numerical Methods in Biomedical Engineering*, 27, 1930-1950.

ZHAO, Q., MA, H., LIU, Y., YAO, C., YANG, L. & CHEN, G. 2021. Hydrodynamics and mass transfer of Taylor bubbles flowing in non-Newtonian fluids in a microchannel. *Chemical Engineering Science*, 231, 116299.

Chapter 2. Modelling of silica micro/nano particle synthesis process

2.1 Introduction

In the previous chapter, the overall concept of shear controllable synthesis is given. Then the hydrodynamic mechanisms under the counter swirling impinging flow reactor should be further investigated using CFD. In order to enhance the mixing intensification, the small mechanism is used to generate Rankine vortex on both side of the reactor. When two counter swirling streams collide in the impinging chamber the vigorous mixing takes place. Thus, this chapter focuses on the characteristics of impinging turbulence flow occurring in the impact reactor and its effects on the chemical reaction. As the volume fraction of particles is very low (1.1%), the impact of the solid phase can be neglected. Thus, only one-way coupling is considered in this study.

The hydrodynamic synthesis of nanoparticles is a key field in chemical engineering. Numerical simulation has always been a useful tool for the prediction of the synthesis process of particle production. Akroyd et al. (2011) investigated the detailed modelling of nanoparticle synthesis in turbulent flow field. For CFD simulations, they adopted a projected fields method and a population balance using full coupling between the flow, chemistry and particles. To further revealed the nanoparticles synthesis process, a detailed population balance model was employed for the gas-phase composition. Johannessen et al. (2000) studied the fluid-particle dynamics

during the synthesis process of alumina. A differential Reynolds stress turbulence model was used in the work to calculate the local shear force, which provided useful insight into the system. Buesser and Pratsinis (2011) investigated the gas-phase coating of core-shell particles, where the turbulence was described by the Reynolds stress model.

To expand the application of nanoparticles, size control is another emphasis in the research of this work. According to Hoshyar et al. (2016), the control of nanoparticle size has a great effect on pharmacokinetics and cellular interaction, i.e., particle diameter around 50 nm is the most suitable for cellular uptake in thermodynamic models, but for tumour penetration 20 nm or less is much better. Walkey et al. (2012) also validated that the nanoparticle size played a determining role in efficiency of cellular uptake. Cao et al. (2006) studied the performance and structure of the PVDF membranes at different nanoparticle size. The PVDF membranes showed great performance at smaller size. Therefore, our work mainly focuses on the hydrodynamic approach in the synthesis of silica oxide nanoparticle and how it affects the size and morphology.

2.2 Mathematical modelling

2.2.1 Governing equations for descriptions of particle synthesis process

In order to model the hydrodynamics during the synthesis process, the following assumptions are introduced: due to the low volume fraction of particles, the one-way

coupling is assumed; particles are assumed to be spherical and rigid; hydrodynamics is dominant by shear turbulence.

Hence the numerical simulation is conducted in the one-way coupling regime, fluid flow is assumed to be incompressible and continuous. Compared with the two-phase flow, single-phase flow problem is much easier, less sensitive to grids quality and less costly to solve. Therefore, it is logical to solving the single-phase flow fluid dynamics equations as the first and fundamental step before further solving the actual two-phase model.

In micro/nano silica particles synthesis, the hydrodynamics is also controlled by Navier-stokes equations. Thus, the continuity and momentum equation can be described by Equation 2-1 and Equation 2-2

$$\frac{\partial \rho}{\partial t} + \frac{\partial(\rho \bar{u}_i)}{\partial x_i} = 0 \quad (2 - 1)$$

Equation 2-1 states that the mass rates change is conservative (Domingues et al., 2010). In this work, the fluid is assumed to be incompressible as the particles are regarded as solid phase, Equation 2-1 can simplify into $\nabla \cdot \mathbf{u} = 0$.

$$\frac{\partial}{\partial t}(\rho u_i) + \frac{\partial}{\partial x_j}(\rho u_i u_j) = -\frac{\partial p}{\partial x_i} + \frac{\partial}{\partial x_j} \left[\mu \left(\frac{\partial u_i}{\partial x_j} + \frac{\partial u_j}{\partial x_i} - \frac{2}{3} \delta_{ij} \frac{\partial u_i}{\partial x_i} \right) \right] + \frac{\partial}{\partial x_j} (-\rho \overline{u'_i u'_j}) \quad (2 - 2)$$

2.2.2 Turbulence closure model of RSM

In this study, Reynolds stress model is adopted. Unlike one-equation and two-equation models, RSM solves seven extra transport equations. Thus, it has wide applicability among all kinds of classical models, accurate in predicting mean flow

properties and all Reynolds stresses for complicated turbulent flows (swirl, rotation, curved flows and non-circular duct flows) and easy to set up in CFD solvers.

The exact transport equation for the Reynolds stress $\overline{u'_i u'_j}$ is expressed as follows (Versteeg and Malalasekera, 2007),

$$\frac{\partial \overline{u'_i u'_j}}{\partial t} + C_{ij} = P_{ij} + D_{ij} - \varepsilon_{ij} + \Pi_{ij} + \Omega_{ij} \quad (2-3)$$

the convection term is

$$C_{ij} = \frac{\partial (\rho U_k \overline{u'_i u'_j})}{\partial x_k} = \text{div}(\rho \overline{u'_i u'_j} \mathbf{U}) \quad (2-4)$$

the production term is given by

$$P_{ij} = - \left(\frac{\partial U_j}{\partial x_m} + \frac{\partial U_i}{\partial x_m} \right) \quad (2-5)$$

the rotational term is expressed as

$$\Omega_{ij} = -2\omega_k (\overline{u'_j u'_m} e_{ikm} + \overline{u'_i u'_m} e_{jkm}) \quad (2-6)$$

where ω_k is the rotation vector and e_{jkm} is the alternating symbol. e_{jkm} equals to +1, -1, 0 when i, j, k are different and in cyclic order; different and in anti-cyclic order or any two indices are the same, respectively.

Equation 2-7 is the diffusion term that modelled under the hypothesis that the transport rate by diffusion is proportional to Reynolds stress gradients

$$D_{ij} = \frac{\partial}{\partial x_m} \left(\frac{\nu_t}{\sigma_k} \frac{\partial \overline{u'_i u'_j}}{\partial x_m} \right) = \text{div} \left(\frac{\nu_t}{\sigma_k} \text{grad}(\overline{u'_i u'_j}) \right) \quad (2-7)$$

where $\nu_t = C_\mu \frac{k^2}{\varepsilon}$, $C_\mu=0.09$ and $\sigma_k=1.0$.

the dissipation rate term of $\overline{u'_i u'_j}$ is described as

$$\varepsilon_{ij} = \frac{2}{3} \varepsilon \delta_{ij} \quad (2 - 8)$$

where ε is the energy dissipation rate, δ_{ij} is Kronechker delta equals to 1 ($i = j$) or 0 ($i \neq j$).

the pressure-strain term is proportional to anisotropy degree and production processes, defined as follow,

$$\Pi_{ij} = -C_1 \frac{\varepsilon}{k} \left(\overline{u'_i u'_j} - \frac{2}{3} k \delta_{ij} \right) - C_2 \left(P_{ij} - \frac{2}{3} P \delta_{ij} \right) \quad (2 - 9)$$

with $C_1=1.8$ and $C_2=0.6$

2.2.3 Numerical modelling

Description of the problem

In this study, we adopt a self-designed reactor, the counter swirling impinging flow reactor, which can be roughly separated into three parts, two small-sized swirling impinging jet reactors and an impact chamber with an outlet and an ultrasonic pressure inlet. The collide and impinging of two counter swirling streams is achieved by using two small-sized swirling impinging jet reactors that connected at the impact chamber. As shown in Figure 2-1, the size of the domain is 192 mm in length, 80 mm in width and 60 in height, besides, the diameter of the inlet is 6 mm. To ensure the ultrasonic effectiveness, the ultrasonic probe is inserted about 1 mm in depth. By superimposing a tangential flow onto an axial flow, the turbulent swirl flows are generated and a spiral vortical structure is induced in the core, known as engulfment flow. It rotates along the channels into the impact chamber for further interaction. The interface area of two streams increases attributing to this engulfment flow, allowing

particles to strongly interact with turbulent eddies, thus promoting mass transfer rate.

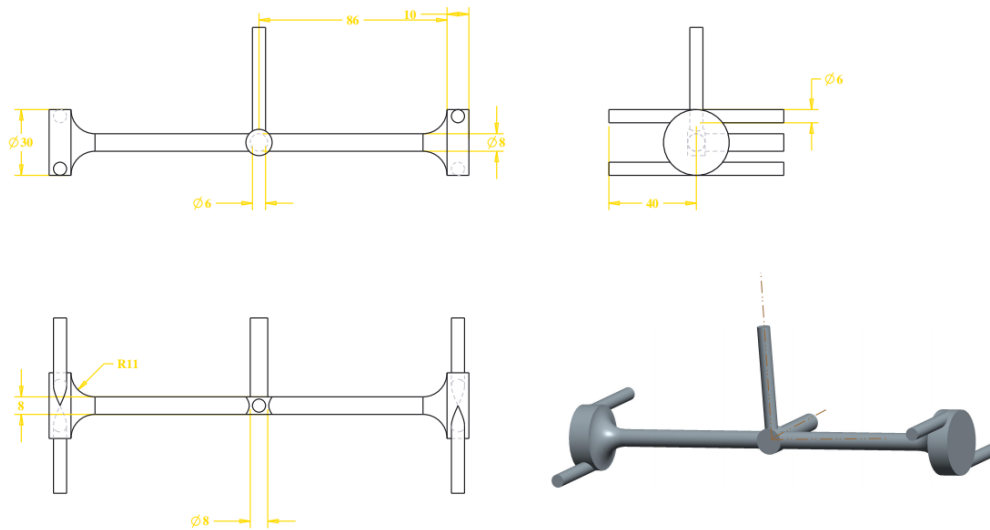


Figure 2-1 3D drawing and dimension size (mm) of counter swirling.

ANSYS Fluent 15.0 software is used to solve the numerical simulation. Since the single-phase model is used in predicting fluid flow properties, water is assumed as the flow material. The density of water is 998.2 kg/m^3 and the viscosity is about 0.001003 kg/ms . Incompressible flow, transient time and gravity in the y-direction are considered in this analysis. The convergence criterion is set as 10^{-3} for all parameters when residuals attain values under 10^{-3} indicates a converged solution. To obtain the steady state of turbulent flow, simulation is conducted for 10^5 time steps with a time step size of 10^{-5} s , which is long enough, and maximum of 100 iterations are performed per time step to reach calculation convergence. Our case is based on PRESTO! schemes for pressure equation, first order upwind spatial discretization of other convection-diffusion equations and the pressure-velocity coupling is resolved using SIMPLE algorithm.

Mesh generation

In consideration of this complex geometry, unstructured grids are applied to the middle domain, including an impact chamber with an outlet, an ultrasonic pressure inlet and two channels. Structured grids are used on the rest of the domain. ANSYS ICEM 15.0 software allows generating hexahedral unstructured grids, which has obvious advantages over 3D tetrahedral mesh in terms of calculation accuracy, deformation characteristics, mesh number, anti-distortion degree and repartition times. Due to the complexity of mesh-plotting near the impact chamber area, the impact chamber can be divided separately into 8 sub-blocks, and then these blocks are extruded to other parts (outlet, ultrasonic pressure inlet, channels) for further meshing. For circular surfaces, the O-type block method is used to improve the efficiency and the quality of grids, Figure 2-2 shows the detail of the hexahedral meshes at the middle region as well as tetrahedral meshes near the inlets, the total number of elements throughout the domain are 717945. To ensure the accuracy of computing, two interfaces are established as the connections between unstructured and structured meshes, where the grids are refined.

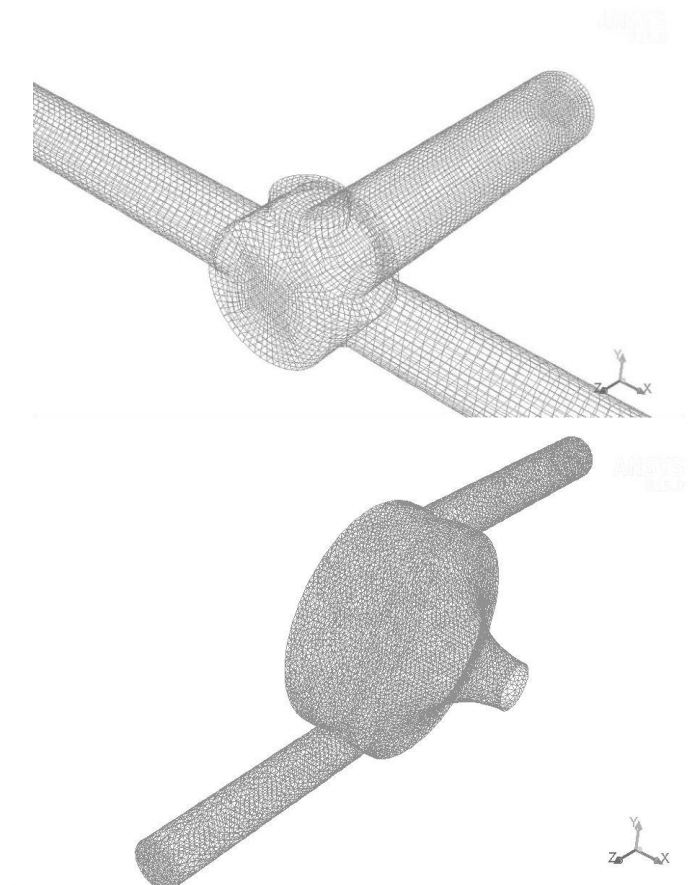


Figure 2-2 Detail meshes of unstructured and structured at different regions.

In order to consider the mesh impendence result, we employ mesh cells from 0.34 million to 1.4 million. Since the present work, the turbulent dissipation rate will play a significant role in the determination of local shear stress. Thus, we use the turbulent dissipation rate as an indicator for mesh independent check.

Figure 2-3 is a plot of turbulent dissipation rate at a point with different number of cells. It can be found that with 0.34 million cells, ϵ at the monitor point is $13.55 \text{ m}^2/\text{s}^3$. By increasing the mesh resolution to 0.7 million, the monitor point value jumps to $18.61 \text{ m}^2/\text{s}^3$. The further 1.4 million cell simulation results in an almost same value compare with the previous simulation. It can be seen clearly that trial simulation

results with 1.4 million cells have reached a solution value ($18.68 \text{ m}^2/\text{s}^3$) that is independent of the mesh size. As further refined mesh seems has not much change, we thus employ the mesh size of 0.7 million throughout the whole work.

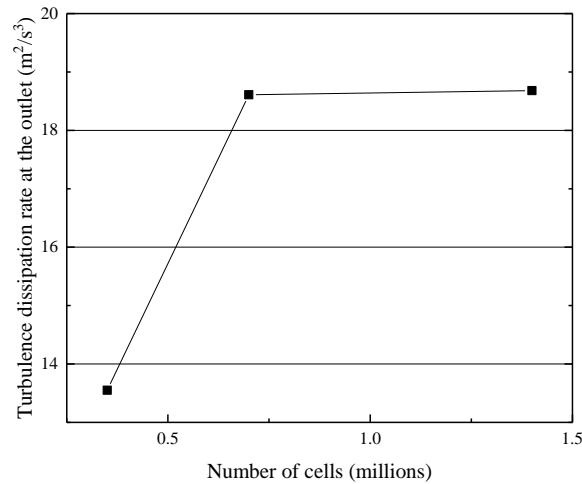


Figure 2-3 Turbulence dissipation rate at a monitor point with different number of cells.

Boundary conditions

The boundary conditions in ANSYS Fluent are:

Inlet: The average velocity at inlet is estimated by $U = \frac{Q}{A}$, where Q is the volume flowrate velocity and $A = \frac{\pi d^2}{4}$ ($d=6 \text{ mm}$) is the cross-sectional area of the inlet.

Table 2-1 gives the details of velocity setting. For the approximations of turbulent kinetic energy and dissipation rate at inlets, CFD solvers use formulas described as follows,

$$k = \frac{2}{3}(U_{in}I)^2 \quad (2 - 10)$$

$$\varepsilon = C_{\mu}^{3/4} \frac{k^{2/3}}{0.07R} \quad (2 - 11)$$

where I is the turbulent intensity set as 5 %, R is the hydraulic radius of the inlet, $C_{\mu}=0.09$.

Pressure outlet: At the outlet, assumed the flow reaches the fully developed state and set the pressure to zero.

Wall: Enhanced wall treatment is adopted for the no-slip near wall region modelling, it specifies both the energy dissipation rate ε and the turbulent viscosity μ_t in the near-wall cells.

In order to get accurate results, three different cases are implemented which represents three practical experiments. Due to the limitation of processing accuracy, the pre-calibration finds there exists little difference between four peristaltic pumps, as shown in Table 2-1.

Table 2-1 Input flow velocity at four inlets.

	U_{in1} (m/s)	U_{in2} (m/s)	U_{in3} (m/s)	U_{in4} (m/s)
Case 1	0.219	0.2	0.193	0.2
Case 2	0.264	0.247	0.237	0.247
Case 3	0.316	0.285	0.286	0.294

2.3 Results and discussion on silica micro/nano particle synthesis

2.3.1 Shear turbulence in counter swirling impinging flow reactor

The turbulence flow generates three mixing intensification regions. Two of them occur in the swirling impinging chambers, and the rest happens in the impact chamber due to the converge of two counter-swirling streams with an initial velocity U . It is clearly demonstrated in Figure 2-4 that two counter swirling streams collide and impinge at the impact chamber where the mixing intensity is enhanced.

Previous study (Guo et al., 2021) has already shown the physical characteristics of the fluid in the swirling chamber. Thus, the numerical simulation near the impact chamber should be studied in detail. As shown in Figure 2-5, at the centre of the impact chamber, the turbulent dissipation rate ε and turbulent intensity I_t reach their highest values, that is, the dispersing mixing performance is enhanced greatly. The underlying reason is the turbulent kinetic energy k first gathers in the large-scale eddies, then the energy cascade takes place, leading to the energy transfers from large scales of motion to small scales (Kolmogorov microscales). During this period, the energy dissipation occurs and high efficiency of mixing takes place under micro scale. The relationship between ε and I_t can be given by Equation 2-10 and Equation 2-11 as follows,

$$\varepsilon = \frac{C_\mu^{3/4} (u I_t)^3 \left(\frac{3}{2}\right)^{3/2}}{l} \quad (2 - 12)$$

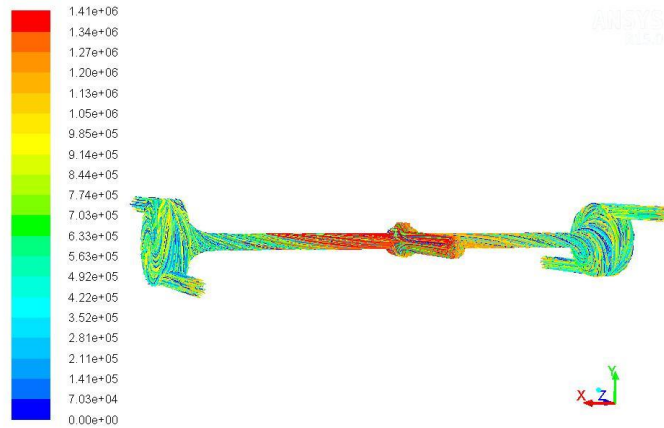


Figure 2-4 Pathlines image of the fluid flow.

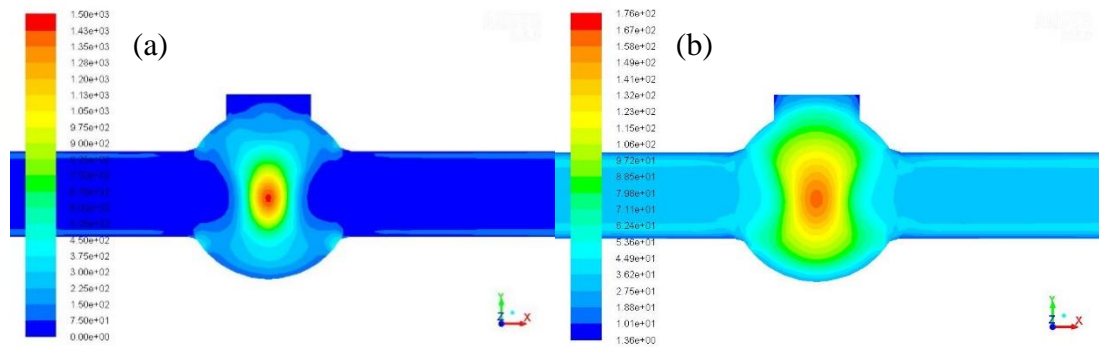


Figure 2-5 Contours of (a) turbulent dissipation rate and (b) turbulent intensity near the impact chamber.

In order to clearly see the overall shear turbulence inside the reactor, Figure 2-6 is given to show the major features of the shear stress field near the outlet. The shear stress, defined as $\tau = \rho\mu \cdot \sqrt{\varepsilon/\mu}$ (where μ is the molecular dynamic viscosity and ρ is the density of the medium), decreases along the outlet due to the reduction in turbulence dissipation rate ε . Both images in Figure 2-8 (a) and (c) show that the peak values of shear stress and energy dissipation rate occurs primarily near the centre

($z=-0.004$ m) of the impact chamber. The time-averaged centreline ε_{OUT} shown in Figure 2-8 (a) and (b) indicate that the turbulence flow breakdown both in axial and radial distance as the flow moves downstream. The relevant turbulence shear stress also decreases due to the relationship with turbulence dissipation rate as discussed before. The image of shear stress vectors at the end of the outlet is shown in Figure 2-7, which shows four axisymmetric vortexes mixing zone occurs after travelling through the impact zone, suggesting an intensive and sufficient mixing in this region.

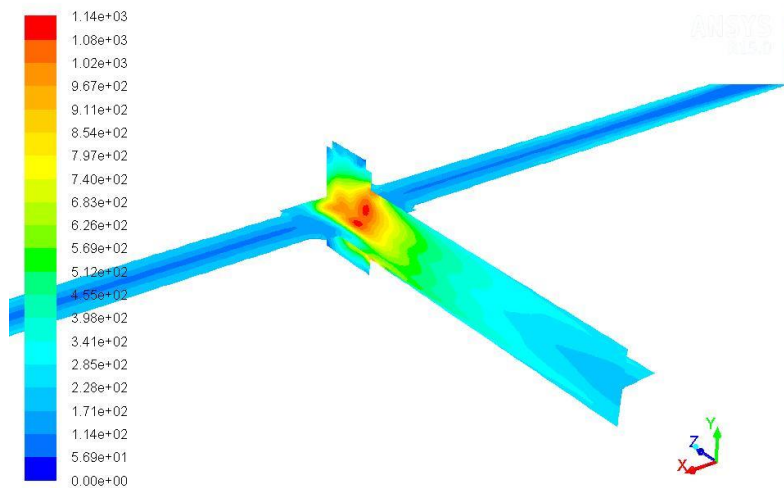


Figure 2-6 Turbulence shear contours at different cross section ($x=0$; $y=0$) of outlet.

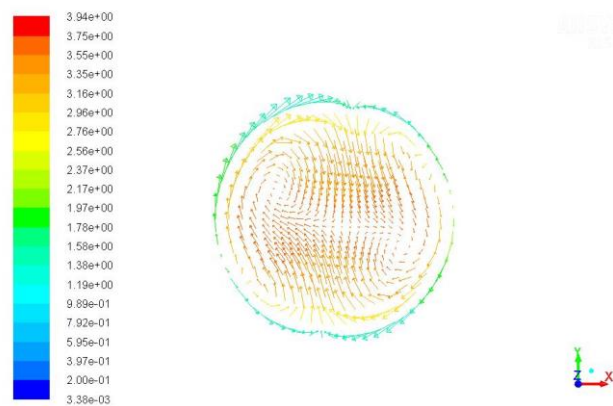


Figure 2-7 Eddy vortexes at the cutting plane of outlet ($z=-30$).

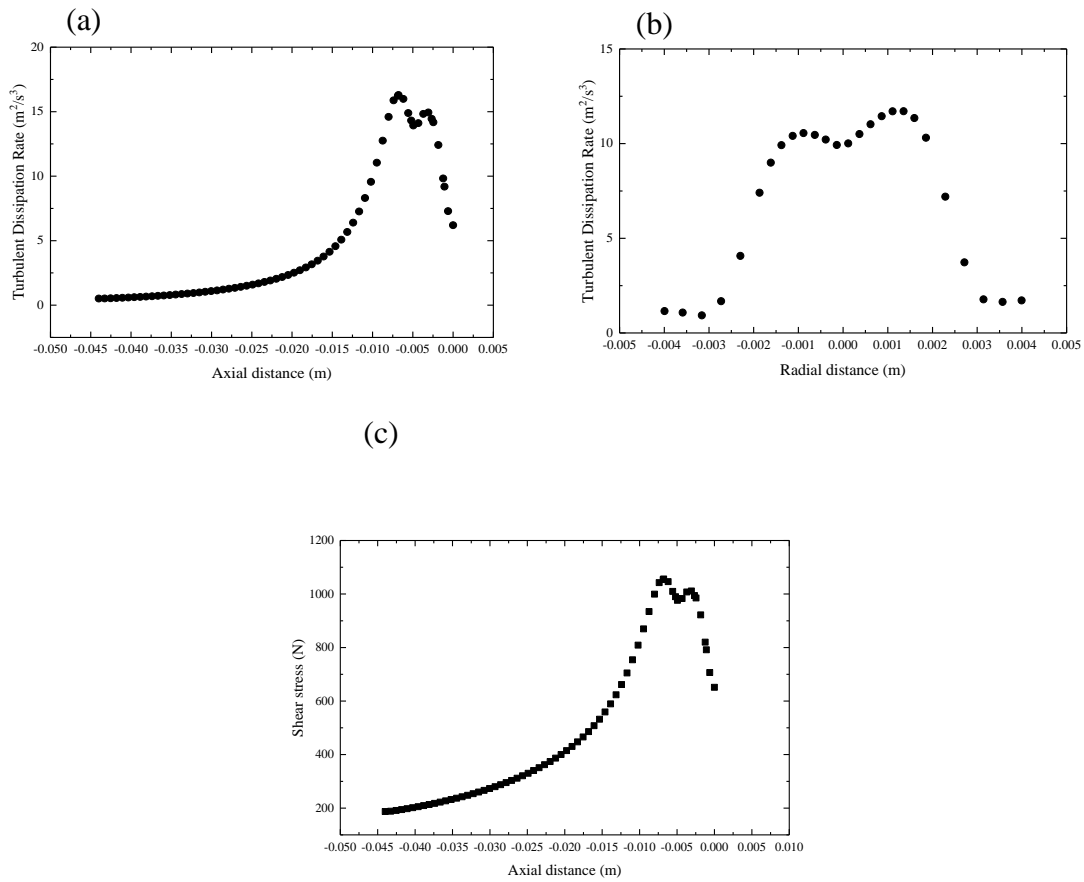


Figure 2-8 Turbulence dissipation rate ε_{OUT} profiles at (a) axial distance and (b) radial distance of outlet; shear stress τ_{OUT} profile at (c) axial distance of outlet.

2.3.2 Turbulence shear effect on particle aggregation

The formulation of particle aggregation

Previous work has indicated that the formed aggregates are significantly influenced by turbulence shear stress. The following aggregation phenomena have also been found microorganisms, bioflocs. The fundamentals of this mechanism can be concluded in two main aspects: (1) shear rate influences the flow field properties,

such as shear viscosity (Lutsko and Dufty, 1985), turbulence structure, heat and mass transfer (Rashidi and Banerjee, 1990); (2) the breakup of suspended solids in the flow field is highly dependent on shear rate (Marchisio et al., 2006, Ehrl et al., 2009).

The aggregation process can be governed by several mechanisms, including Brownian motion, shear aggregation and differential settling (Hunt, 1986), where the shear aggregation (described in Equation 2-13) is the dominated mechanism while the effect of Brownian motion and differential settling can be neglected (Soos et al., 2008).

$$n(v) = A_{sh} \left(\frac{E}{G} \right)^{1/2} v^{-2} \quad (2 - 13)$$

where $n(v)$ represents the size distribution function, G is shear rate, E is the distribution of aggregate particle size and v is a particle volume flux, A_{sh} are dimensionless constants for the respective aggregate mechanisms.

Equation 2-13 indicates that the particle size distribution is inversely proportional to the shear rate. The experiment analysis results show this suggestion as well. As shown in Figure 2-9, the particle size distribution of three cases is given, indicating the increase of shear rate results in narrower size distribution.

Particle size prediction

Generally, the local shear stress is a result of fluid flow which plays a leading role in determining the particle size. Thus, the aggregate size can be estimated in terms of average shear rate according to Jarvis et al. (2005),

$$d_{max} = CG^{-\gamma} \quad (2 - 14)$$

$$G = \sqrt{\frac{\varepsilon}{\nu}} \quad (2 - 15)$$

where d_{\max} is the possible maximum aggregates size under the certain average shear rate G , C is the aggregate strength coefficient and γ is the stable aggregate size.

Take case 3 as example, the distribution of aggregates (as shown in Figure 2-9) under Case 3 condition is obtained by particle size analysis. From the collected data, the possible maximum size d_{\max} is around $230.9 \mu m$ and the stable size γ is around $42.653 \mu m$. The average shear rate is obtained from ANSYS Fluent. In this case the volume average shear rate $\langle G \rangle$ is $0.438 s^{-1}$. Thus, the aggregate strength coefficient in our work can be roughly calculated by the following equation

$$C = G^{-\gamma} / d_{\max} = 0.438^{-42.653} / 230.9 = 8.5 \times 10^{12}$$

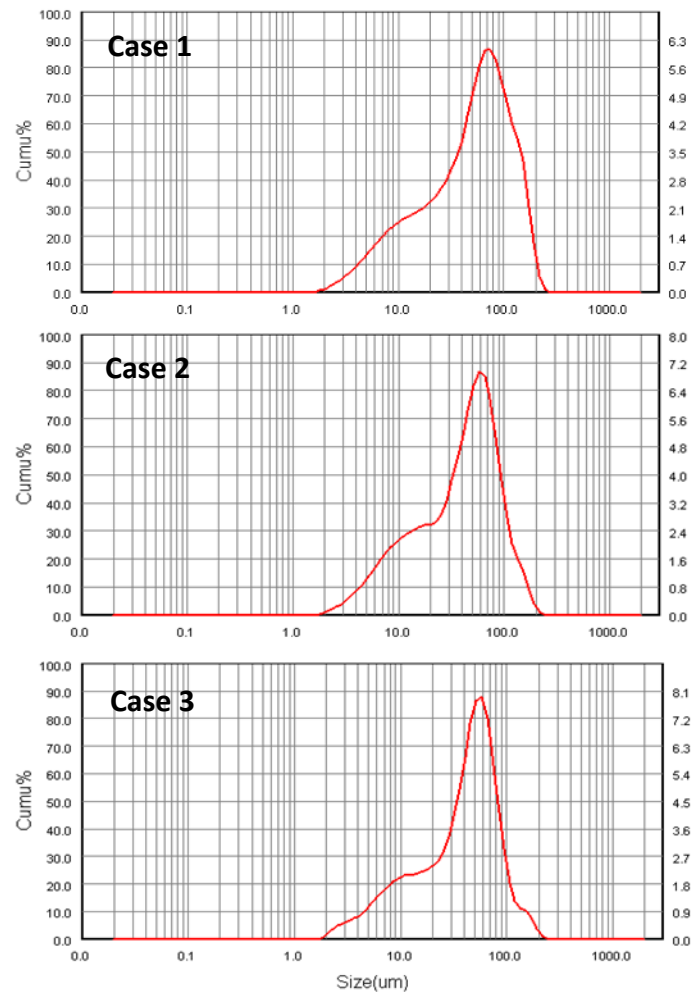


Figure 2-9 Aggregate size distribution at Re=2997 (case 1); 3676 (case 2); 4363 (case 3).

In our work, different hydrodynamic conditions are applied by adjusting the volumetric flowrate and the introduction of ultrasound irradiation. The aim of these strategies is to control the turbulent shear intensity. The breakup process occurs when the shear stress is strong enough to compete with intermolecular forces between particles. Zaccone et al. (2009) has revealed a correlation between the shear stress τ and the value of aggregate gyration radius R_g at equilibrium, as shown by Equation

2-17,

$$R_g \propto \tau^p \quad (2 - 17)$$

With the turbulence developed, shear stress is finally determined by the energy dissipation rate ε , for aggregate size smaller than the Kolmogorov microscale $\eta = (v^3/\varepsilon)^{1/4}$ (where v is the turbulence kinematic viscosity and ε is the dissipation rate), that is, the aggregate within the viscous subrange of turbulence, shear stress can be defined as (Malay et al., 2013),

$$\tau_{VS} = \frac{5}{2} \mu \sqrt{\frac{\varepsilon}{6v}} \approx \mu \sqrt{\frac{\varepsilon}{v}} \quad (2 - 18)$$

However, when aggregate size is larger than η , that is, the aggregate is in the inertial subrange, the hydrodynamic stress is in the form of,

$$\tau_{IS} = \rho(\varepsilon d_{agg})^{2/3} \quad (2 - 19)$$

where ρ is the density of fluid flow and d_{agg} is the diameter of the aggregate.

As given above, the particles size is always related to the turbulent energy dissipation rate. In Chapter 3, the results of silica oxide particles synthesis are given where we can conclude an empirical formula reflects the exact mathematic relation between the micro/nano particles size and shear rate. In order to determine the influence of shear turbulence on the synthesised particles, a correlation constant between volume average turbulent shear rate and particle equivalent has been proposed, defined by,

$$R_{\langle G \rangle, d_{equ}} = \frac{\frac{1}{N} \sum_{i=1}^n \langle G \rangle d_{equ}}{\left[\frac{1}{N} \sum_{i=1}^n \langle G \rangle \right] \left[\frac{1}{N} \sum_{i=1}^n d_{equ} \right]} \quad (2 - 20)$$

where $\langle G \rangle$ is the volume average turbulent shear rate, d_{equ} is the equivalent

diameter of particles and subscript i denotes different conditions.

It can be seen clearly from Figure 2-10 that the diameter of silica oxide and $\langle G \rangle$ has very strong correlation, and large $R_{(G)}, r_{equ}$ results in small particles. With the increase of shear rate, the diameter decreases, as well as a decrease in aggregation rate due to the rupture of aggregate surfaces by shear rate. Theoretically, shear caused by hydrodynamics can overcome the van der Waals force leading to the breakup of the aggregation.

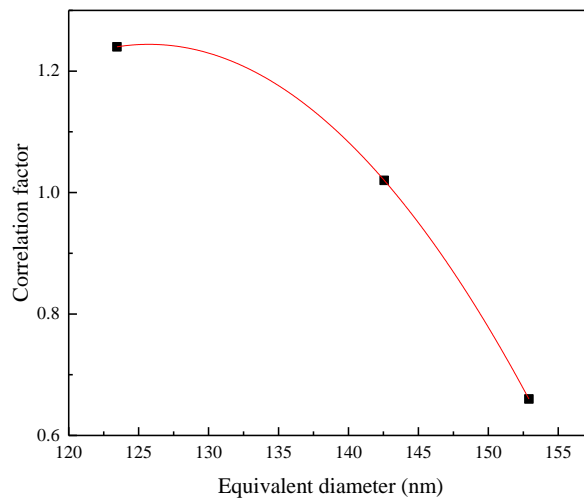


Figure 2-10 The correlation factor as a function of equivalent diameter of particles in the counter swirling impinging flow reactor.

2.4 Effects of the interaction between the turbulence shear rate and reaction on synthesis process

To identify the impact further improve the influence of mixing on the particle synthesis process of SiO_2 , the Damköhler number is adopted, which is a ratio of micro

mixing time scale τ_t and chemical reaction time scale τ_c . Different expressions for τ_t have been proposed, for this work it comes close to Kolmogorov time scale $\tau_t = 12 \sqrt{\frac{\nu}{\langle \varepsilon \rangle}}$ (Baladyga and Pohorecki, 1995). For first-order reaction, the Damköhler number can be written in the form of Equation 2-21,

$$Da = \frac{\tau_t}{\tau_c} = \frac{12 \sqrt{\frac{\nu}{\langle \varepsilon \rangle}}}{c} r = 12 \sqrt{\frac{\nu}{\langle \varepsilon \rangle}} k \quad (2 - 21)$$

where ν is kinematic viscosity, $\langle \varepsilon \rangle$ is volume average energy dissipation rate and k is the reaction rate constant.

The formation of SiO_2 particles contains two steps: hydrolysis and condensation. As the hydrolysis is predominant step in this reaction, k was found equal to the value of hydrolysis reaction rate constant $7.41 \times 10^{-3} \text{ s}^{-1}$ (Xu et al., 2005), thus, giving out the value of Da in the order of 10^{-4} . The obtained $Da \ll 1$ which indicates the system is reaction controlled by its true unhindered kinetic. In the range of Reynolds number from 2997 to 4363, the Da number decrease from 1.88×10^{-4} to 1.33×10^{-4} , as shown in Figure 2-11. It clearly indicates that the turbulent mixing intensification enhances the diffusive mass transport rate, where the reactants and products are rapidly mixed.

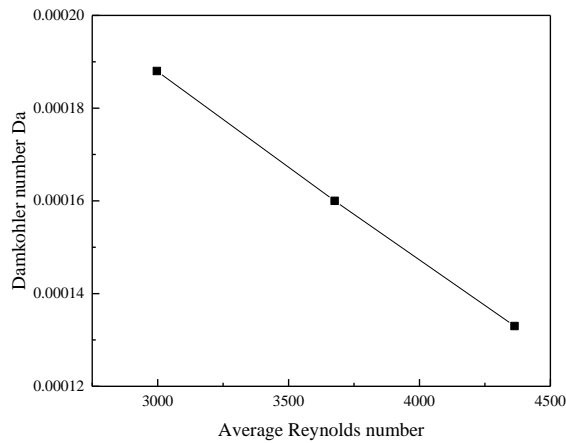


Figure 2-21 Damköhler number versus average Reynolds number.

2.5 Conclusion

In summary, we have studied the shear turbulence inside our counter swirling impinging flow reactor using CFD modelling where the Reynolds stress model is chosen. Due to the 1.1% volume fraction of particles, the one-way coupling method is adopted for this dilute system. A general concept of the flow field distribution in the reactor can be obtained from the above profiles. Two counter swirling flow streams converge in the impact chamber, resulting in an intensive mixing region and at least four vortexes are formed in the chamber. In the intensified mixing region, the eddy engulfment is much stronger that can trap the particles into higher shear force. Thus, the micro/nano particle size and shape are correlated to the turbulent flow. By further theoretically investigating the relationships between the particle size and shear effects, we understand the key factor to control the synthesis process is shear turbulence which can be controlled by adjusting the flow conditions. Furthermore, through the experimental and simulation data, an aggregate strength coefficient $C = 8.5 \times 10^{12}$

is calculated in this study which can be used to predict the aggregate size in this synthesis system. The present results indicate the shear turbulence is enhanced by the converge of counter swirling flows, which plays a significant role in the determination of the micro/nano particle size.

The study on modelling of micro/nano particle synthesis process has important reference for continual experiments in synthesis of silica oxide particles. We believe with the further validation of experiments in the next chapter, the synthesis mechanism can be thoroughly revealed.

References

- AKROYD, J., SMITH, A. J., SHIRLEY, R., MCGLASHAN, L. R. & KRAFT, M. 2011. A coupled CFD-population balance approach for nanoparticle synthesis in turbulent reacting flows. *Chemical Engineering Science*, 66, 3792-3805.
- BAŁDYGA, J. & POHORECKI, R. 1995. Turbulent micromixing in chemical reactors—a review. *The Chemical Engineering Journal and the Biochemical Engineering Journal*, 58, 183-195.
- BUESSER, B. & PRATSINIS, S. E. 2011. Design of gas-phase synthesis of core-shell particles by computational fluid–aerosol dynamics. *AIChE journal*, 57, 3132-3142.
- CAO, X., MA, J., SHI, X. & REN, Z. 2006. Effect of TiO₂ nanoparticle size on the performance of PVDF membrane. *Applied Surface Science*, 253, 2003-2010.
- DOMINGUES, N., CAMESASCA, M., KAUFMAN, M., MANAS-ZLOCZOWER, I., GASPAR-CUNHA, A. & COVAS, J. 2010. Modeling of agglomerate dispersion in single screw extruders. *International Polymer Processing*, 25, 251-257.
- EHRL, L., SOOS, M., MORBIDELLI, M. & BÄBLER, M. U. 2009. Dependence of initial cluster aggregation kinetics on shear rate for particles of different sizes under turbulence. *AIChE journal*, 55, 3076-3087.
- GUO, Y., YANG, X., LI, G., YANG, J., LIU, L., CHEN, L. & LI, B. 2021. Shear turbulence controllable synthesis of aggregated nano-particles using a swirling vortex flow reactor assisted by ultrasound irradiation. *Chemical Engineering*

Journal, 405, 126914.

HOSHYAR, N., GRAY, S., HAN, H. & BAO, G. 2016. The effect of nanoparticle size on in vivo pharmacokinetics and cellular interaction. *Nanomedicine*, 11, 673-692.

HUNT, J. R. 1986. Particle aggregate breakup by fluid shear. *Estuarine cohesive sediment dynamics*. Springer.

JARVIS, P., JEFFERSON, B., GREGORY, J. & PARSONS, S. A. 2005. A review of floc strength and breakage. *Water research*, 39, 3121-3137.

JOHANNESSEN, T., PRATSINIS, S. E. & LIVBJERG, H. 2000. Computational fluid-particle dynamics for the flame synthesis of alumina particles. *Chemical Engineering Science*, 55, 177-191.

LUTSKO, J. & DUFTY, J. W. 1985. Hydrodynamic fluctuations at large shear rate. *Physical Review A*, 32, 3040.

MARCHISIO, D. L., SOOS, M., SEFCIK, J. & MORBIDELLI, M. 2006. Role of turbulent shear rate distribution in aggregation and breakage processes. *AIChE journal*, 52, 158-173.

RASHIDI, M. T. & BANERJEE, S. 1990. The effect of boundary conditions and shear rate on streak formation and breakdown in turbulent channel flows. *Physics of Fluids A: Fluid Dynamics*, 2, 1827-1838.

SOOS, M., MOUSSA, A. S., EHRL, L., SEFCIK, J., WU, H. & MORBIDELLI, M. 2008. Effect of shear rate on aggregate size and morphology investigated under turbulent conditions in stirred tank. *Journal of colloid and interface*

science, 319, 577-589.

VERSTEEG, H. K. & MALALASEKERA, W. 2007. *An introduction to computational fluid dynamics: the finite volume method*, Pearson education.

WALKEY, C. D., OLSEN, J. B., GUO, H., EMILI, A. & CHAN, W. C. 2012. Nanoparticle size and surface chemistry determine serum protein adsorption and macrophage uptake. *Journal of the American Chemical Society*, 134, 2139-2147.

XU, Y., LIU, R., WU, D., SUN, Y., GAO, H., YUAN, H. & DENG, F. 2005. Ammonia-catalyzed hydrolysis kinetics of mixture of tetraethoxysilane with methyltriethoxysilane by ^{29}Si NMR. *Journal of non-crystalline solids*, 351, 2403-2413.

ZACCONE, A., SOOS, M., LATTUADA, M., WU, H., BÄBLER, M. U. & MORBIDELLI, M. 2009. Breakup of dense colloidal aggregates under hydrodynamic stresses. *Physical Review E*, 79, 061401.

Chapter 3. Experimental investigation on turbulence shear controllable synthesis of micro/nano porous silica oxide particle

3.1 Introduction

In the previous chapter, the characteristics of turbulence induced shear are revealed by means of CFD simulations. To further validate the effect of shear force controllable approach, experiments are carried out. Stöber et al. (1968) developed an approach of controlling the growth of monodisperse spherical silica particles with different kinds of reagents. With controlling the amount of ammonia used, the size of silica particles varied. In 1846, French chemist Ebelmen (1845) first found that TEOS synthesised gels slowly when they were hydrolysed in air, thus leading to a new era of sol-gel method. For further applications, researchers built up porous inside the silica nanoparticles (Velev et al., 1997, Velev et al., 1998, Kuang et al., 2004). It was reported that cationic surfactant head groups can be used to change the structure of particles. Cetyltrimethylammonium Bromide (CTAB) is a commonly used surfactant and is the surfactant used in this study, but when synthesised with CTAB the nanoparticles tend to agglomerate.

Recently, many researchers investigated the fluid flow influences on particle synthesis rather than the ratio of reactants. Das and Garrick (2010) studied the nanoparticle growth rate in turbulent reacting flow, it is found that the higher growth rate existed in

the eddies. This method also works in a turbulent flame reactor (Kammler et al., 2001), leads to high production rates and small particle size.

3.2 Experimental setup

The counter impinging swirling flow reactor is composed of two small swirling vortex flow reactors connected by a cylindrical impact chamber and an outlet on the back of the impact chamber, as shown in Figure 3-1 the whole reactor was embedded in a stainless-steel block. A swirling vortex flow reactor consists of two tangential inlets ($D = 6$ mm) as feeding nozzles, a circular cylindrical impinging chamber ($D = 30$ mm, $H = 10$ mm) and an outflow channel ($D = 6$ mm, $L = 80$ mm). On the top of the impact chamber there exists a vertical small tube ($H = 24$ mm) which allows the ultrasound probe to insert in for imposing the power. Temperature of the reactant solution was kept constant at 65°C by a magnetic stirrer. During the reaction, the solution is injected into four inlets simultaneously by four peristaltic pumps, then rotates along the channels and finally flow back to the beaker from the outlet. The peristaltic pumps are connected to the beaker by hoses which dependent on squeezing and releasing the elastic delivery hose of the pump to circulate of the reactant solution. During the process, aggregate particles caused by strong cohesive forces such as Van der Waals forces and repulsive electrostatic forces can be broken and re-dispersed due to the turbulent shear rate, $G = \sqrt{\frac{\varepsilon}{\nu}}$, where ε is the energy dissipation rate per unit mass and ν is the kinematic viscosity. Controllable synthesis method in our study is realised by changing the rotation speed and the ultrasound amplitude which results in

the introduction of different intensity of shear force acting on aggregates. To better understand the effect of shear force on particle synthesis, mesoporous silica oxide is prepared under various parameters, different average Reynolds number range from 989 to 4360 and ultrasound power range from 360 w to 1080 w are investigated.

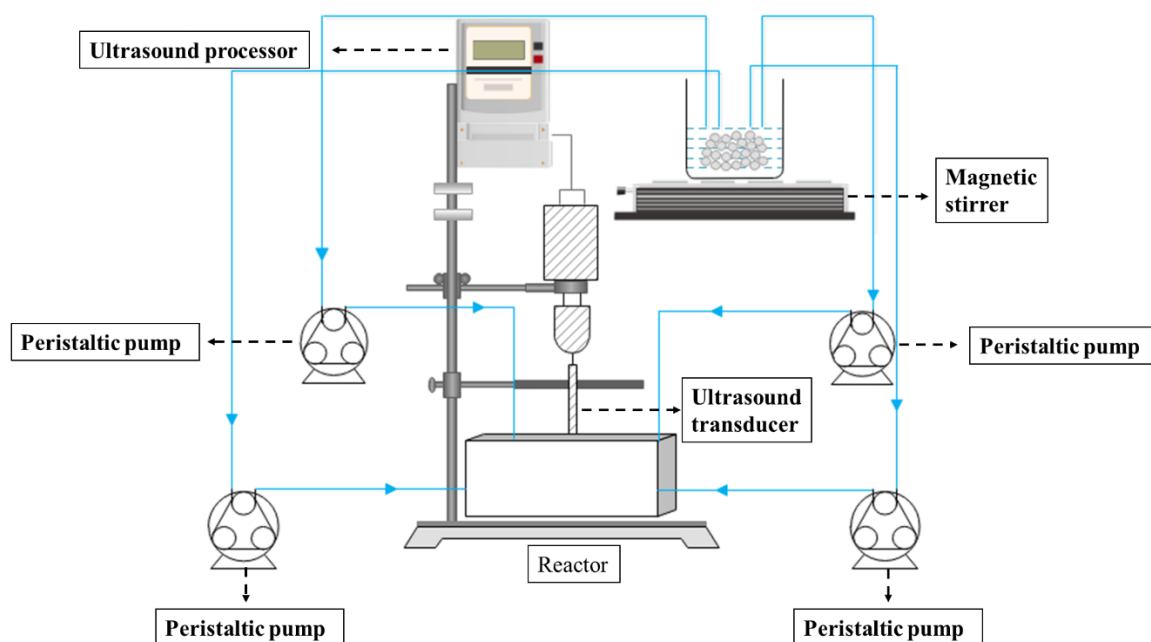


Figure 3-1 Schematic drawing of experimental setup.

3.3 Materials and experimental description

Materials

1. Hexadecyltrimethylammonium bromide (CTAB)

CTAB, purchased from Sinopharm Chemical Reagent Co., Ltd., which serves not only as the stabilizing surfactant for the nanoparticles in the liquid phase, but also serves as liquid templating micelle molecule for the formation of the mesoporous silica. The overall formation mechanism of mesoporous is the silica source builds up inorganic walls between CTAB formed micelles. The micelles become a two

dimensional hexagonal mesostructured in aqueous phase, then the silica precursor begins to hydrolyse between the surfactant micelles and finally the silicon dioxide is filled in the gap. The porous template can be removed by calcination at high temperature and leave a pore structure behind. The micelles shape can be changed by controlling the molar ratio between CTAB and TEOS, that is because the interfacial energy and the hydrophobic cores, as the molecule structure of CTAB consists of a hydrophilic polar head and a hydrophobic hydrocarbon tail.

2. Tetraethyl orthosilicate (TEOS)

Tetraethyl orthosilicate (TEOS > 28.5%) as the silica precursor (purchased from Sinopharm Chemical Reagent Co., Ltd.). Under the action of the catalyst, it is prone to hydrolysis to form polysilicon acid, ethanol and intermediates.

3. Sodium hydroxide (NaOH)

NaOH solution (2 M) is a base catalyst, hydrolysis process proceeds faster in basic conditions. The catalyst can not only influence the hydrolysis and condensation of silica precursor, but also improve the kinetics of reaction. Thus, the pH value of the system plays a significant role in governing the nanoparticle size.

Preparation of solution

Generally, the sol-gel synthesis mechanism of silica can be generally divided into three procedures (Dorcheh and Abbasi, 2008). First is the gel preparation, gelation is appeared after the sol that synthesised by a silica source solution added the catalyst. Second is the aging of the gel, the gel prepared in the above step is aged and

strengthened in its mother solution, so that during the drying process the shrinkage can be kept to a minimum. The last step is the drying and calcination process, in this step the gel gets rid of the surfactant template which can prevent the collapse of the gel structure.

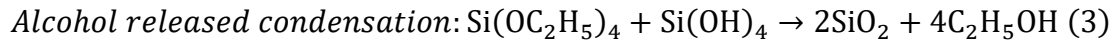
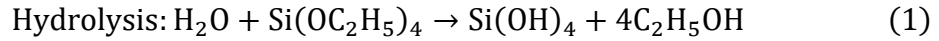
The synthesis of mesoporous silica aggregates is achieved by the NaOH-catalysed hydrolysis and condensation of TEOS by using CTAB as surfactant under water solution. In the experimental procedure, first, a mixed solution is prepared by dissolving CTAB and NaOH solution (2 M) in deionized water. After 30 min stirring at 65 °C a clear solution is obtained, TEOS is added into the mixture solution dropwise. The reaction is allowed to proceed for 1 hour, the resulting products are filtered under vacuum, washed with water, to obtain the silica gel. Then the products are dried at 100 °C in the convection oven for 5 h and then calcination at 500 °C for 6 h in the muffle oven to remove the template completely. Agitation is achieved by using counter swirling impinging flow reactor with peristaltic pump. Different samples with various operation parameters $Re_{aver} = 989; 2093; 2997; 3676; 4363$ under 360w, 600w, 1080w ultrasound power are synthesised in our study, listed in Table 3-1.

Table 3-1 Prepared samples under different experimental conditions.

Sample	Experimental conditions		
	Ultrasonic power (W)	Average corresponding Reynolds number	Volumetric flowrate (ml/s)
S1	0	989	$U_{in1}=2.02$; $U_{in2}=1.76$; $U_{in3}=2.05$; $U_{in4}=1.74$
S2	0	2093	$U_{in1}=4.38$; $U_{in2}=3.71$; $U_{in3}=4.31$; $U_{in4}=3.65$
S3	0	2997	$U_{in1}=6.18$;
S6	360		$U_{in2}=5.46$;
S7	600		$U_{in3}=5.64$;
S8	1080		$U_{in4}=5.66$
S4	0	3676	$U_{in1}=7.46$;
S9	360		$U_{in2}=6.71$;
S10	600		$U_{in3}=6.99$;
S11	1080		$U_{in4}=6.97$
S5	0	4363	$U_{in1}=8.94$;
S12	360		$U_{in2}=8.09$;
S13	600		$U_{in3}=8.06$;
S14	1080		$U_{in4}=8.31$

3.4 Synthesis and kinetics

In this study, a sol-gel process with base catalyst is adopted to produce SiO₂ nanoparticles. By means of hydrolysis and condensation reactions, the sol phase is formed and the small colloidal particles inside the sol condense into the gel phase.



The formation of micelles by CTAB is the templating agent, which can direct the silicate source to condense around the templating micelle molecule into ordered silica structures (Li et al., 2012).

3.4.1 Reaction kinetics of silica nanoparticles by sol-gel process

In the hydrolysis process, the removal of first alkoxy group is the limited step. Based on the steric effects of the substitutes, when fewer alkoxy groups around the silicon atom, the nucleophilic OH^- more vigorously attack the silicon atom. From the perspective of charge induction effect, the addition of OH^- ions can reduce the charge density of silicon atom which makes the attack of water molecules easier. Thus, the substitution reaction rate increases due to the subsequent attack of OH^- ions on other alkoxy group (Bari et al., 2020). According to the study of Malay et al. (2013), it is assumed that silica precursor hydrolysed through single hydrolysed monomer as shown in Equation 3-1,



where Q_0^0 is the TEOS, Q_1^0 represents the product formed after first attack of OH^- and R is the alkoxy group.

Aelion et al. (1950) validated that the hydrolysis reaction catalysed by dilute sodium hydroxide is of first order in relation to the concentrations of both silica precursor concentration and hydroxyl ion,

$$r_{TEOS} = -d[Q_0^0]/dt = k_H[Q_0^0][OH^-] \quad (3 - 2)$$

Because the concentration of OH^- is in great excess with respect to TEOS, it can be considered invariable. Then a pseudo first order rate constant, k_H^* , can be defined as

$$k_H^* = k_H[OH^-] \quad (3 - 3)$$

Thus, the hydrolysis rate Eq. can be simplified into

$$r_{TEOS} = -d[Q_0^0]/dt = k_H^*[Q_0^0] \quad (3 - 4)$$

the integration of Equation 3-4 is

$$\ln[Q_0^0] = \ln[Q_0^0]_0 - k_H^*t \quad (3 - 5)$$

Since each subsequent hydrolysis step occurs quickly under basic conditions, reaction will spend more time on condensation, which proceeds as soon as the alkoxy group has been hydrolysed. Si-O-Si bonds formed rapidly after the addition of TEOS droplet into water and catalyst solution (Das and Das, 2015). The condensation of $Si(OH)_4$ (Q_4^0) is approximated as an irreversible reaction, because the equilibrium concentration of $Si(OH)_4$ in reactant solution is larger than in the alcohol solution.



The rate of the above reaction can be calculated as follows (Dorcheh and Abbasi, 2008),

$$r_{Si(OH)_4} = d[Q_4^0]/dt = k_H[Q_0^0] - k_C[Q_4^0] \quad (3 - 7)$$

$$r_{SiO_2} = d[SiO_2]/dt = \frac{[Q_0^0]_0}{L_\infty^3 - L_0^3} \frac{dL_t^3}{dt} = k_C[Q_4^0] \quad (3 - 8)$$

From the above Equation 3-7 and Equation 3-8 the diameter of aggregates after the reaction can be given by,

$$L(t) = \left\{ L_0^3 + \left[1 - \frac{k_C}{k_C - k_H} e^{-k_H t} + \frac{k_C}{k_C - k_H} e^{-k_C t} \right] (L_\infty^3 - L_0^3) \right\}^{1/3} \quad (3 - 9)$$

where L_0 is the initial aggregate diameter, L_∞ is the final aggregate diameter.

The concentration of consumed TEOS can be described by Equation 3-10

$$[Q_0^0]_R = [Q_0^0]_0 (1 - e^{-k_H t}) \quad (3 - 10)$$

The concentration of produced silica can be calculated as

$$[SiO_2] = [Q_0^0]_0 \frac{L_t^3 - L_0^3}{L_\infty^3 - L_0^3} \quad (3 - 11)$$

3.4.2 Formation process of silica oxide

Rahman and Padavettan (2012) suggested that monomer addition model and controlled aggregation model can be used to illustrate the growth mechanism of silica.

The monomer addition model describes the rapid nucleation burst that forms all the particle growth sites, then the particle growth proceeds through the addition of monomers to the surface of existing particles (Matsoukas and Gulari, 1988). By comparison, under a controlled aggregation model the nucleation sites are generated continuously throughout the reaction, and the initial nanoparticles prone to aggregate together into coarse and large particles (aggregates).

The second kinetic model fits well with experimental observations including microgravity analysis, variable pH analysis and small-angle X-ray scattering analysis.

Based on the controlled aggregation model, the nucleation rates follow the equation below (Bogush and Zukoski Iv, 1991)

$$J = g_s(e^{-k_1t} - e^{-k_2t}) \quad (3 - 12)$$

where J is the nucleation rate, g_s is the normalization factor based on the quantity of silica precursor, and k_i represents rate constant according to the concentrations of H₂O and base catalyst.

Whether nanoparticles are aggregated or disaggregated should be determined by the interaction energy under specific conditions. The aggregation is thermodynamically preferable when the interaction energy minimum shows at a short interparticle distance; otherwise, the disaggregation is preferred (Butt et al., 2013). The total interaction energies between particles are generally attributed to electrostatic repulsion, van der Waals force and the effects of solvation, which provides a barrier and affect the merging of nucleation sites. Thus, the aggregation process and the final uniform spherical morphology are related to these interaction energies. V_T is the sum of three forces (Lee et al., 1998),

$$F_T = F_{vdw} + F_{elec} + F_{solv} \quad (3 - 13)$$

Ideally, the nanoparticles are supposed to be spherical and the surface layer is very thin, thus the van der Waals attraction between nanoparticle and surface layer, surface and surface layer can be neglected. The van der Waal force between particles is expressed by the following equation

$$F_{vdw} = -\frac{A_H}{6} \left[\frac{2a_1a_2}{R^2 - (a_1 + a_2)^2} + \frac{2a_1a_2}{R^2 - (a_1 - a_2)^2} + \ln \frac{R^2 - (a_1 + a_2)^2}{R^2 - (a_1 - a_2)^2} \right] \quad (3 - 14)$$

where A_H is the Hamaker constant, R is the distance between the centres of two neighbouring particles and a_i is the radius of the particle.

From the work of Bergström (1997) based on Lifshitz theory, the Hamaker constant A_H for silica is around 6.5×10^{-20} J. Thus, the van der Waals attraction F_{vdw} between the synthesised nanoparticles can be estimated. Take Sample 5 for instance, the value of R (157.28 nm) and a_i can be obtained from Figure 3-3. Due to the worm-like morphology, equivalent radius is used in this work (Limin and Jing, 2006).

$$a_1 = r_{equ-1} = \frac{1}{2} w_1 \sqrt{\frac{1}{\alpha_1}} = \frac{1}{2} \times 192.9 \times \sqrt{0.64} = 77.16 \text{ nm}$$

$$a_2 = r_{equ-2} = \frac{1}{2} w_2 \sqrt{\frac{1}{\alpha_2}} = \frac{1}{2} \times 181 \times \sqrt{0.56} = 67.72 \text{ nm}$$

where w and α is the average width and aspect ratio of nanoparticles.

Therefore, the van der Waals force can be calculated from Equation 3-14,

$$F_{vdw} = -\frac{6.5 \times 10^{-20}}{6} \times \left(\frac{2 \times 77.16 \times 67.72}{157.28^2 - (77.16 + 67.72)^2} + \frac{2 \times 77.6 \times 67.72}{157.28^2 - (77.16 - 67.72)^2} + \ln \frac{157.28^2 - (77.16 + 67.72)^2}{157.28^2 - (77.16 - 67.72)^2} \right) = 1.44 \times 10^{-20} \text{ N}$$

Aggregation phenomenon occurred during the growth process is mostly attributed to van der Waals force. In order to make better control of the production quality, we can compare the shear force applied on the nanoparticle to the F_{vdw} as the indicator for the conducting of experiment. The shear force can be calculated by the following equation,

$$\tau_{eddy} = \mu_l \langle G \rangle$$

$$\langle G \rangle = \sqrt{\frac{\langle \varepsilon \rangle}{\nu}}$$

$$\text{thus, } \tau_{eddy} = 4.061 \times 10^{-4} \times \sqrt{0.438 / 4.061 \times 10^{-7}} = 0.42 \text{ N/m}^2$$

where μ_l is the dynamic viscosity of the fluid and ν is the kinematic viscosity of the fluid at reaction temperature of 70°C, as the solution is a dilute system, the fluid is regarded as water in this study. $\langle \varepsilon \rangle$ is the volume average energy dissipation rate (obtained from ANSYS Fluent) and $\langle G \rangle$ is the volume average shear rate throughout the fluid.

$$\tau_{vdw} = F_{vdw} / A_{particle} = 1.44 \times 10^{-20} / \left(\frac{\pi(a_1 + a_2)^2}{8} \right) = 1.75 \times 10^{-6} \ll \tau_{eddy}$$

$A_{particle}$ is assumed to be the cross-sectional area of a cylindrical particle formed by two smaller particles (a_1, a_2).

The results of calculation are in great agreement with the experimental result that the synthesised powders are almost aggregates. Therefore, this data comparison can be expended to predict the dispersity of final production when using shear controllable synthesis method.

3.5 Characterization methods

Scanning Electron Microscopy (SEM) images are observed by a Hitachi SU8200 cold field emission scanning electron microscope at 2.5 kV. The pre-treatment is applying the powders on the double-sided sticky electric conductive adhesive which is put on a

microscope stub. Before the microscopy, all samples are needed to coat with a thin gold film (10 nm) under vacuum as silica oxide is nonconducting.

N₂ adsorption–desorption isotherm measurements are conducted by a Micromeritics ASAP 2020M pore analyser with a continuous adsorption environment. Samples are degassed at 200°C before analysis. The surface area, pore volumes and pore size distribution of the particles can be obtained by using the Brunauer–Em-mett–Teller (BET) and Barrett–Joyner–Halenda (BJH) analyses.

The chemical composition of the prepared samples are characterised using Fourier transform infrared spectroscopy (FTIR, Agilent Cary660+620). Before measurement samples are compacted as pellets and KBr are dried at 120°C for 24 h. KBr is thoroughly mixed and crushed with the sample by using a mortar and pestle. The mixture is placed in a pellet former then pressure is applied to form the KBr pellet.

Particle size analysis is performed on the Bettersize 2000 particle size analyser by measuring angular changes in the time scattering intensity of a laser beam through a dispersed particle sample. Then, using Mie theory of light scattering, angular scattering intensity data are measured to calculate the size of the particles that generate the scattering pattern. The particle size is calculated by volume equivalent spherical diameter.

3.6 Results and discussion

3.6.1 Characteristics of synthesised silica oxide particles

To confirm the chemical structure of the synthesised particles, FTIR spectroscopy analysis is conducted. As shown in Figure 3-2, six peaks are observed. The observed peak at 1632.447 cm^{-1} and the broad band around 3443.313 cm^{-1} is attributed to Si-H₂O flexion and Si-OH stretching vibration with hydrogen bonded. The asymmetric vibrations of Si-O-Si at peak around 1088.62 cm^{-1} , 801.278 cm^{-1} is corresponding to the symmetric stretching vibration of O-Si-O and the peak at 462.832 cm^{-1} is detected due to the bending vibrations of Si-O. The peak at 962.3049 cm^{-1} is originated from the flexural vibration absorption of Si-OH.

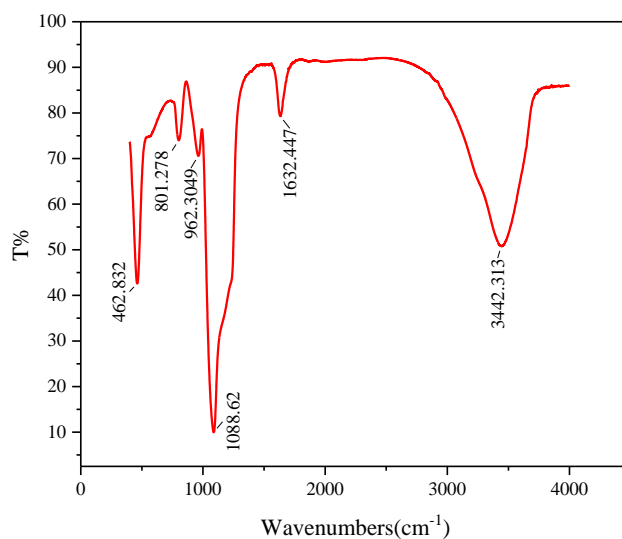


Figure 3-2 FT-IR spectra of synthesised SiO₂.

SEM images are taken as an indicators of particle morphology, as shown in Figure 3-3 to 3-6. Interestingly, it is noted that under conditions without ultrasonic power the

structure turned to be worm-like. This is attributed to the orientation of turbulence shear at the outlet, as shown in Figure 3-3 the turbulence shear decays with distance. When the ultrasonic power is induced, the particles are segmented into sphere morphology much smaller and uniform size. The aspect ratios and average sizes of nanoparticles also with the size distributions are analyzed using Fiji image J. As considering the problems that the silica nanoparticles are prone to aggregate due to the van der Waal force and the worm-like silica, the DSL is not an appropriate method to accurately estimate the nanoparticle size. As the Table 3-2 shows, aspect ratio of the worm-like particles is measured using their average width and height, which suggests the morphology becomes uniform with the increase of volumetric flowrate. As shown in Figure 3-4 to 3-6, the size distribution is demonstrated by using the Gaussian fitting which is a function of the following form Equation 3-18, the mean values of nanoparticle diameter are concluded in Table 3-3.

$$f(x) = a \cdot e^{-\frac{(x-b)^2}{2c^2}} \quad (3 - 18)$$

where a and b are arbitrary real constants and c is non-zero.

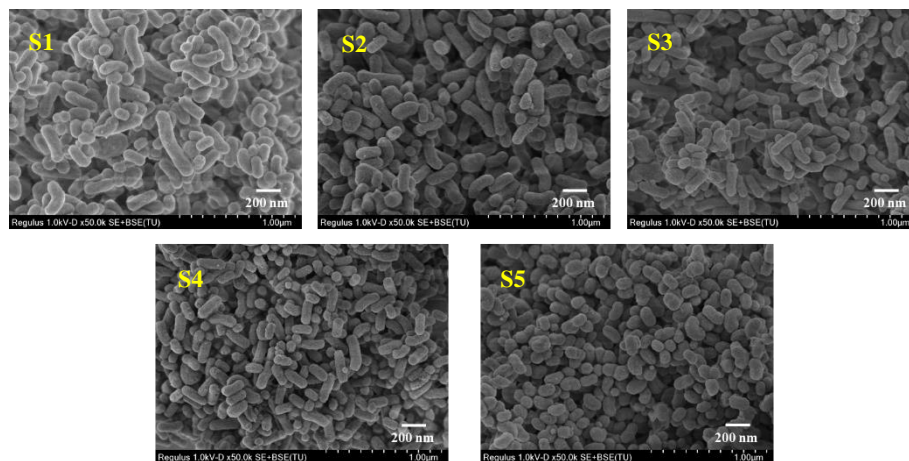


Figure 3-3 SEM images of SiO₂ nanoparticles at different average Reynolds number

without ultrasonic input power $Re = 989; 2093; 2997; 3676; 4363$.

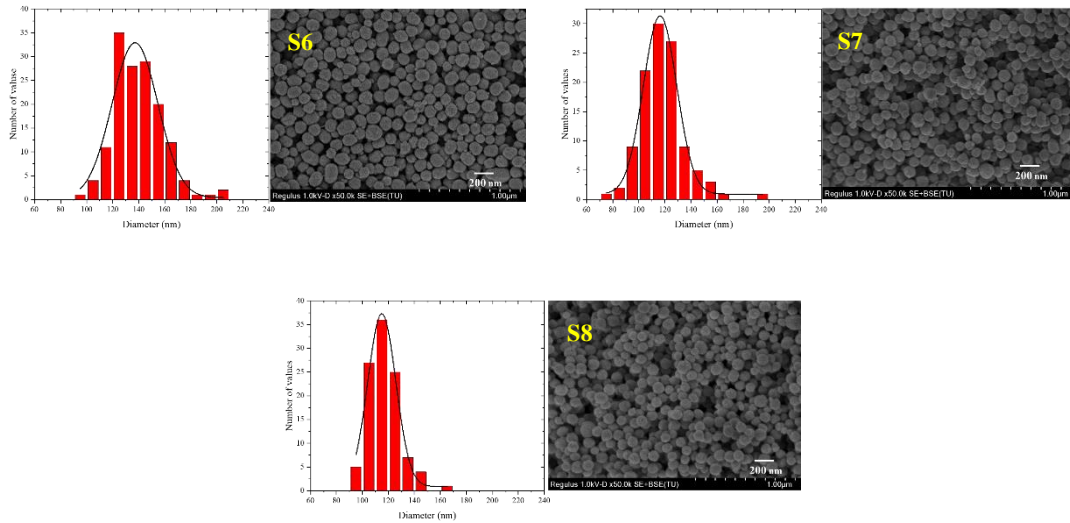


Figure 3-4 SEM images and particle size distribution at $Re = 2997$ under different ultrasound power 600 w (S6); 840 w (S7); 1080w (S8).

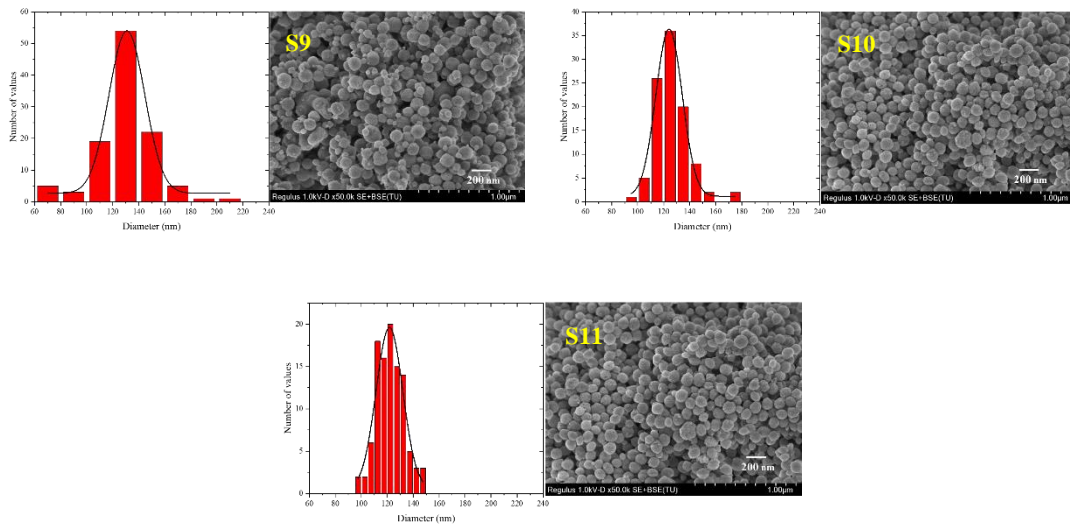


Figure 3-5 SEM images and particle size distribution at $Re = 3676$ under different ultrasound power 600 w (S9); 840 w (S10); 1080w (S11).

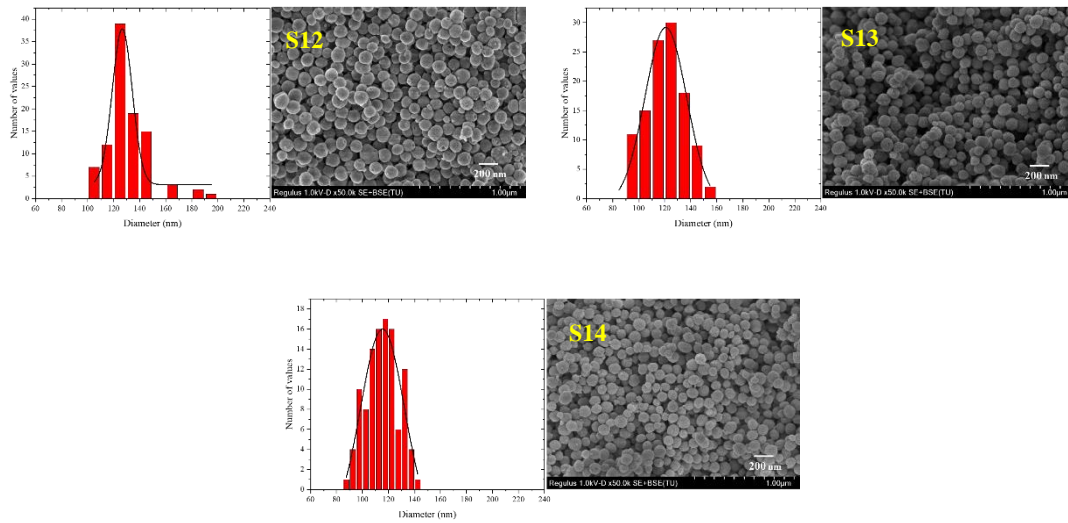


Figure 3-6 SEM images and particle size distribution at $Re = 4363$ under different ultrasound power 600 w (S12); 840 w (S13); 1080w (S14).

Table 3-2 Size analysis of particles with different Reynolds number.

Sample	Average width w (nm)	Average height h (nm)	Aspect Ratio α (width/height)
S1	274.36	106.62	2.57
S2	302.29	108.53	2.79
S3	256.75	91.19	2.82
S4	209.55	86.21	2.43
S5	165.02	123.45	1.34

Table 3-3 Average Ferret diameter of Sample 6-14 under different experimental conditions.

Sample	Average Ferret diameter (nm)		
Reynolds number Ultrasonic power	Re= 2997	Re= 3676	Re= 4363
600 w	137.14±1.79	130.83±0.68	126.57±1.39
840 w	116.26±0.57	124.11±0.56	120.82±1.19
1080 w	114.88±0.68	121.62±0.45	115.32±1.48

Figure 3-7 shows the adsorption and desorption properties of the calcined nanoparticles. The prepared particles exhibited a representative type-IV curve, which is indicative of the mesoporous material. The quantitative relationship between mesopore size and relative pressure obeys the Kelvin function (Equation 3-19) when pore condensation occurs.

$$\ln \frac{p}{p_0} = -\frac{2\sigma V_L}{RT} \cdot \frac{1}{r_m} \quad (3 - 19)$$

where p_0 is saturated vapor pressure, σ surface tension, V_L molar volume and r_m radius of surface curvature.

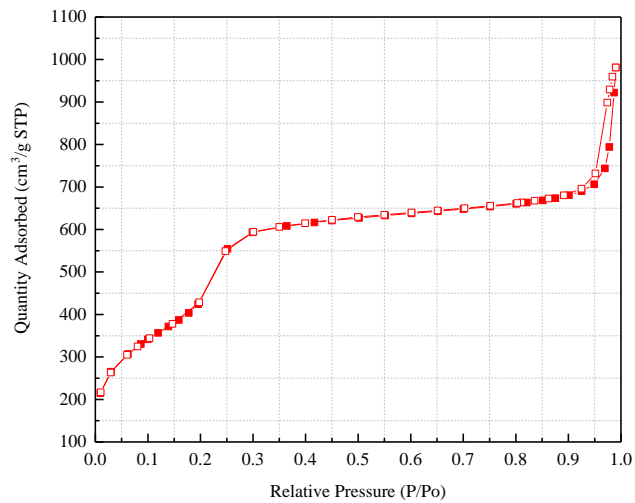


Figure 3-7 Nitrogen adsorption and desorption isotherm liner plot.

3.6.2 Effect of hydrodynamics in counter swirling impinging flow reactor on silica oxide synthesis

To figure out how the Reynolds number affects the nanoparticles characteristics, we keep all the initial conditions constant except for the volumetric flowrate applied. The revolutions per minute (rpm) of the peristaltic pump tube are varied from 300 to 500, the average corresponding Reynolds number are range from 2997 to 4363.

It is found that if the Reynolds number of the fluid flow is increased beyond a certain value, the nanoparticle structure breaks down and tends toward spherical structure. As shown in Figure 3-8, the aspect ratio first increases with the increase of the Re and drops dramatically after reaches a limited value (Re=2997). The results fit the hydrodynamic concept that the shear stress increase with the increase of the Re (as described in Equation 3-20 and Equation 3-21).

$$Re_{eddy} \sim \frac{u'l}{\nu} \sim \frac{v_t}{\nu} \quad (3-20)$$

$$v_t \sim Re_{eddy} \nu \quad (3-21)$$

where u is the flow velocity, μ is the dynamic viscosity of the flow, ρ is the flow density, d is the hydraulic diameter.

However, the first two cases are occurred under laminar flows where the shear strength is not strong enough compared to the cohesion of substance. Thus, the worm-like nanoparticles cannot be broken up but become larger in width. Under turbulent conditions the breakup process happens, and the aspect ratio of nanoparticles is close to 1 at high Reynolds number, that is, the silica particles are near-spherical.

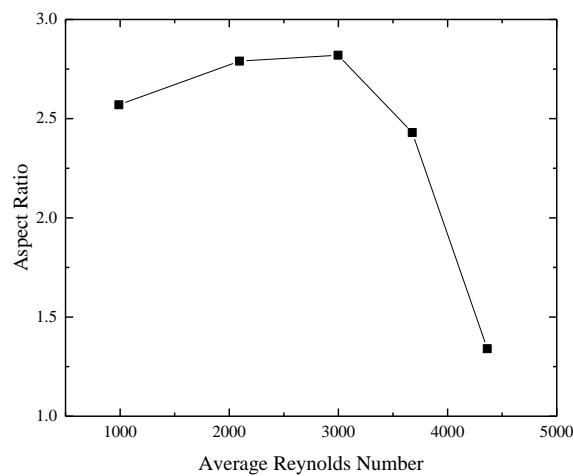


Figure 3-8 Changes in aspect ratio with respect to average Reynolds number of fluid flow.

Figure 3-9 shows the specific surface area of nanoparticles made as a function of average Reynolds number. Increasing the average Reynolds number from 2997 to

3676 and 4363 increases the specific surface area of the nanoparticles from 892 to 1013 and 1200 m²/g respectively, indicating that more pore cavities have formed under turbulent flow conditions.

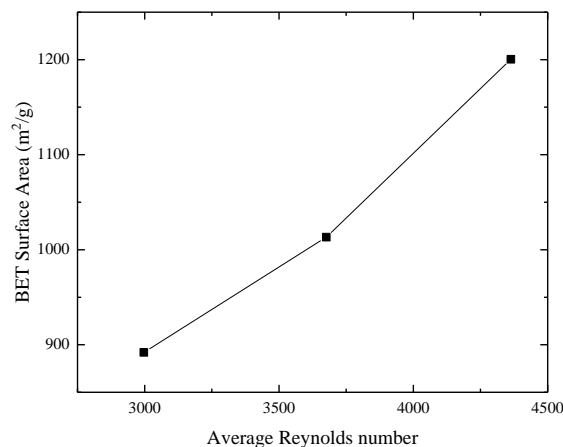


Figure 3-9 BET surface area as a function of the average Reynolds number.

3.6.3 Effect of ultrasound irradiation intensification on in hydrodynamic synthesis

We further carry out synthesis with various ultrasonic power in order to reveal the role of ultrasound in the reaction process. The introduction of ultrasonic field has a significant impact on the structure of the nanoparticles. As shown in Figure 3-4 to 3-6, the increase in ultrasonic power leads to a narrower nanoparticle size distribution. Under different Reynolds number, the particle sizes decrease markedly with the increase of the ultrasonic power (Figure 3-10), tends to produce the smaller size and more uniform morphology of the nanoparticles. This is a result of interplay between hydrodynamic stress (shear stress) and aggregate strength. The hydrodynamic stress

changes with the shear rate which allows the already formed aggregates to be broken up when trapped into eddies with higher shear rates.

It is worth noting that under the ultrasonic field the influence of Reynolds number on nanoparticles becomes unclear, especially the cases at $Re=2997$. From Figure 3-10, it can be found that under higher ultrasonic power the smallest average Ferret diameter occurred at $Re=2997$. This indicates that when turbulence fluid flow assisted with the ultrasound, the generated shear force is dominated by the ultrasonic power.

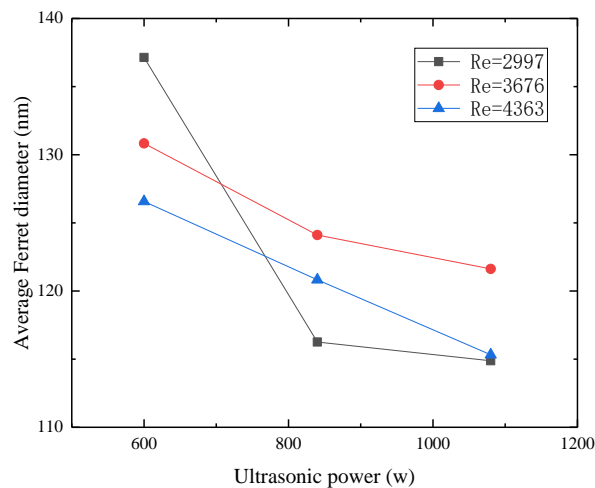


Figure 3-10 Average Ferret diameter of Sample 6-14 under different experimental conditions.

Figure 3-11 shows the specific surface area of nanoparticles made at $Re=2997$ as a function of ultrasonic power. As the ultrasonic power improved, the specific surface area increases apparently, especially at 600 w. But has a little effect when further increase the ultrasonic power. This result suggests that 600 w is the optimal power for the mesopore fabrication.

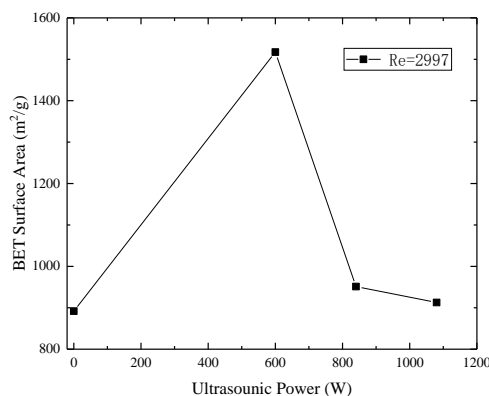


Figure 3-11 BET surface area as a function of the ultrasound power with Re=2997.

3.7 Conclusion

In summary, a systematic experimental investigation on shear controllable synthesis of micro/ nano silica oxide particle inside a counter swirling impinging flow reactor is demonstrated in this chapter. We first control the hydrodynamics inside the reactor by adjusting the volumetric flowrate. With the presence of the shear stress, the shape of silica oxide nanoparticles transformed into rod like. With the addition of CTAB surfactant, meso pores are fabricated inside the nanoparticles, consequently, enlarge the range of application. By increasing the volumetric flowrate in the reactor, the Reynolds number increases, and the flow field transforms into turbulence. This phenomenon is reflected in the morphology and size of silica oxide nanoparticles. As discussed, the aspect ratio and structure uniformity become closer to the spherical one due to the intensive mixing and strong shear stress applied on it.

In order to generation silica oxide nanoparticles with higher uniformity in controllable manners, ultrasound irradiation is adopted. The formation and collapse of bubbles produced by ultrasound power can induce high turbulent eddies around the collapsing bubbles. It is found that the nanoparticles synthesised with ultrasound irradiation show superior performance on size, particles size distributions and specific surface area than.

Our research suggests the shear controllable synthesis assisted with ultrasound strategy enables production of silica oxide nanoparticles with predictable morphologies and allow convenient optimization of their mesoporous properties. We believe our progress on controllable synthesis can be applied to other particles such as drug carrier particles and abrasive particles that require desired morphologies and structural configurations.

References

- AELION, R., LOEBEL, A. & EIRICH, F. 1950. Hydrolysis of ethyl silicate. *Journal of the American chemical society*, 72, 5705-5712.
- BARI, A. H., JUNDALE, R. B. & KULKARNI, A. A. 2020. Understanding the role of solvent properties on reaction kinetics for synthesis of silica nanoparticles. *Chemical Engineering Journal*, 398, 125427.
- BERGSTRÖM, L. 1997. Hamaker constants of inorganic materials. *Advances in colloid and interface science*, 70, 125-169.
- BOGUSH, G. & ZUKOSKI IV, C. 1991. Uniform silica particle precipitation: An aggregative growth model. *Journal of colloid and interface science*, 142, 19-34.
- BUTT, H.-J., GRAF, K. & KAPPL, M. 2013. *Physics and chemistry of interfaces*, John Wiley & Sons.
- DAS, R. & DAS, M. 2015. Catalytic activity of acid and base with different concentration on sol–gel kinetics of silica by ultrasonic method. *Ultrasonics sonochemistry*, 26, 210-217.
- DAS, S. & GARRICK, S. C. 2010. The effects of turbulence on nanoparticle growth in turbulent reacting jets. *Physics of Fluids*, 22, 103303.
- DORCHEH, A. S. & ABBASI, M. 2008. Silica aerogel; synthesis, properties and characterization. *Journal of materials processing technology*, 199, 10-26.
- EBELMEN, M. 1845. Chimie sur une production artificielle de silice diaphane. *Compt. Rendus Acad. Sci*, 21, 502-505.

- KAMMLER, H. K., MUELLER, R., SENN, O. & PRATSINIS, S. E. 2001. Synthesis of silica-carbon particles in a turbulent H₂-air flame aerosol reactor. *AIChE Journal*, 47, 1533-1543.
- KUANG, D., BREZESINSKI, T. & SMARSLY, B. 2004. Hierarchical porous silica materials with a trimodal pore system using surfactant templates. *Journal of the American Chemical Society*, 126, 10534-10535.
- LEE, K., SATHYAGAL, A. N. & MCCORMICK, A. V. 1998. A closer look at an aggregation model of the Stöber process. *Colloids and Surfaces A: Physicochemical and Engineering Aspects*, 144, 115-125.
- LI, Z., BARNES, J. C., BOSOY, A., STODDART, J. F. & ZINK, J. I. 2012. Mesoporous silica nanoparticles in biomedical applications. *Chemical Society Reviews*, 41, 2590-2605.
- LIMIN, Y. & JING, Y. 2006. Image Analysis for Wollastonite Powder With Needle Shape by Fluidized Bed Opposed Jet Mill [J]. *China Non-Metallic Mining Industry Herald*, 2.
- MALAY, O., YILGOR, I. & MENCELOGLU, Y. Z. 2013. Effects of solvent on TEOS hydrolysis kinetics and silica particle size under basic conditions. *Journal of sol-gel science and technology*, 67, 351-361.
- MATSOUKAS, T. & GULARI, E. 1988. Dynamics of growth of silica particles from ammonia-catalyzed hydrolysis of tetra-ethyl-orthosilicate. *Journal of colloid and interface science*, 124, 252-261.
- RAHMAN, I. A. & PADAVETTAN, V. 2012. Synthesis of silica nanoparticles by

sol-gel: size-dependent properties, surface modification, and applications in silica-polymer nanocomposites—a review. *Journal of Nanomaterials*, 2012.

STÖBER, W., FINK, A. & BOHN, E. 1968. Controlled growth of monodisperse silica spheres in the micron size range. *Journal of colloid and interface science*, 26, 62-69.

VELEV, O., JEDE, T., LOBO, R. & LENHOFF, A. 1997. Porous silica via colloidal crystallization. *Nature*, 389, 447-448.

VELEV, O., JEDE, T., LOBO, R. & LENHOFF, A. 1998. Microstructured porous silica obtained via colloidal crystal templates. *Chemistry of Materials*, 10, 3597-3602.

Chapter 4. Conclusions and outlook for the future work

4.1 Conclusions for the present study

Turbulence shear controllable synthesis is a crucial pathway to synthesis nanoparticles with uniform, small size and spherical morphology. This is a bottom-up method which has advantages on the scaling-up, intelligent control on the size, structures and properties of the materials at the nanoscale. In this work, we present our efforts on the size control synthesis of silica nanoparticles and the underlying mechanisms. The main conclusions as the result of present work can be summarised as follows:

(1) In particular our work illustrates the fluid dynamics of counter swirling impinging flow. As introduced in Chapter 2, we use the commercial CFD software ANSYS Fluent 15.0 to simulate the fluid field in our reactor. It is shown that turbulent dissipation rate ε and turbulent intensity I_t reach their highest values near the impact chamber. The shear force decreases as the flow travels downstream of the outlet results in inhomogeneous shear force distribution. We also give a predictive effect that the micro/nano particle size and particle size distribution are highly dependent on the shear rate that applied on it, which always result in smaller size and narrower size distribution with the increase of shear rate. Correlation $R_{\langle G \rangle, d_{equ}}$ between particle diameter d_{equ} and volume shear rate $\langle G \rangle$ is proposed, which shows that with the increase of $\langle G \rangle$, the d_{equ} decreases monotonically, indicating that the synthesised particle morphology is strongly affected by local shear turbulence.

(2) Chapter 3 focuses on the particles that synthesised under turbulent conditions. The size of synthesised nanoparticles ranges from 114 nm to 137 nm. It is shown that nanoparticles with desired size can be produced under various turbulent conditions by adjusting the operating or flow parameters. Through the mathematical comparison between shear force and van der Waals force, it can be verified that the shear force is the key in size determination. We also investigate the influence of the introduction of ultrasonic power in the synthesis process. It is shown that the shear force induced by ultrasound has a great impact on the morphology of nanoparticles, changing the worm-like structure to nearly spherical-like. It is also confirmed that the mixing intensity improves significantly at the impact chamber.

4.2 Recommendations for future work

However, there still exists challenges for shear controllable synthesis. Typically, particles have a tendency to aggregate under van der Waal's force at nanoscale which limits their applications, including pharmacy, polishing on nano-electronic devices that call for monodisperse particles. Therefore, the field of shear controllable synthesis of nanoparticles still exists great potentials to be further developed in order to yield high-quality products.

In the future work, our attention will be paid on the shear controllable synthesis of silica micro/nano particles and their applications. First, the two-way coupling method

will be adopted to further illustrates the physics in the counter swirling impinging flow reactor. Since in Chapter 2 we have solved the single-phase flow problem as the first and fundamental step. Second, from the current particle size analysis, the size of aggregates can reach 10 μm or even larger, which results in bad performance and uncertainties. Thus, the dispersion of products needs to be improved in order to prevent aggregation occurrence during the application process.